Pseudo-γ aluminum oxide: A new transparent conductive oxide with outstanding structural properties

Dissertation
der Mathematisch-Naturwissenschaftlichen Fakultät
der Eberhard Karls Universität Tübingen
zur Erlangung des Grades eines
Doktors der Naturwissenschaften
(Dr. rer. nat.)

vorgelegt von
Michael Ulrich Pfeffer
aus Coburg

Tübingen
2019

Gedruckt mit Genehmigung der Mathematisch-Naturwissenschaftlichen Fakultät der Eberhard Karls Universität Tübingen.

Tag der mündlichen Qualifikation: 18.12.2019
Dekan: Prof. Dr. Wolfgang Rosenstiel
1. Berichterstatter: Prof. Dr. Oliver Eibl
2. Berichterstatter: Prof. Dr. Jannik Meyer

Summary

Tungsten carbide (WC) is a widely used material for cutting tools due to its high mechanical hardness and friction toughness. When exposed to high temperature (e.g. due to friction), oxidation occurs and transforms the stable phase of tungsten carbide to a powdery phase.
To avoid oxidation and enhance the tool lifetime, protective layers are deposited on top of WC substrates consisting of various oxides or nitrides, either as single layers or as multilayer structures. For physical vapor deposition (PVD) processes (e.g. magnetron sputtering), a bias potential is applied to the substrate to achieve the surface energy necessary for the growth process. When growing insulating layers (such as most of the metal oxides), the bias potential is reduced during growth, leading to poorer crystallinity as the layer thickness increases.

Therefore, the development of a semi conductive oxide with advantageous mechanical properties for coating applications is of great interest.

In this thesis, aluminum oxide (Al_2O_3) was deposited on tungsten carbide substrates using dual magnetron sputtering (DSM) with argon as the sputtering gas. The deposition conditions during the growth process provide many different parameters that influence the crystal growth. A combination of argon and oxygen pressure during sputtering, together with the bias potential and substrate temperature was identified as necessary to achieve an electrically conductive aluminum oxide phase.
The goal of this thesis was to analyze the conductive aluminum oxide phase with respect to the structural and electrical features. In addition to the enhanced quality of wear resistant coatings for cutting applications, conductive aluminum oxide is an interesting new member of the transparent conductive oxide (TCO) family. Strong efforts are made to find a replacement for the most widely used material indium tin oxide (ITO), since it relies on expensive and rare materials. A conductive aluminum oxide only requires easily available materials and is therefore an excellent candidate to play an important role in future TCO developments.

Samples analyzed in this thesis were provided by Walter AG in Tübingen. The samples consist of WC substrates (for cutting applications) and wear resistive coatings of aluminum oxide were deposited using DMS. A subset of the samples was coated with an additional $Ti_{0.33}Al_{0.67}N$ layer using high power impulse magnetron sputtering (HIPIMS).

The structure of the conductive phase was identified as a disordered cubic structure, containing aluminum, oxygen and argon up to mole fractions of 2.5 at%. To make a distinction to insulating disordered cubic aluminum oxide phases known as γ aluminum oxide, the conductive phase is called pseudo-γ aluminum oxide.
Due to its unique structure (known as disordered spinel) of γ aluminum oxide, it is possible to incorporate rather large amounts of noble gas atoms into the structure. But only when argon is incorporated in the growth using DMS, the conductive phase is formed. The Ar atoms seem to stabilize the pseudo-γ phase.
To get a grasp on the role of argon in the formation of the conductive phase, the structural features as well as the electrical properties were investigated in detail in this thesis.

Investigations were performed both in plan-view and in cross-section. The samples were cho-

sen to cover a wide range of samples properties such as film thickness, deposition bias, but also different hardness values. Quantitative energy-dispersive x-ray spectroscopy (EDX) in a scanning electron microscope (SEM) was carried out to trace the Ar mole fraction and to establish a correlation thereof to the sample hardness.

By precisely determining the Ar mole fraction in plan-view as well as cross-section in SEM EDX point scans, the argon mole fraction was successfully correlated to the sample hardness, showing that the Ar atoms are essential to the forming of the stable structure. In addition, a shift in the lattice spacing towards a larger unit cell was observed when more Ar was incorporated into the pseudo-γ aluminum oxide phase.

By performing SEM EDX linescans in cross-section, the Ar distribution was found to be non-uniform. The highest Ar amount was always found at the interface to the WC substrate, but different content profiles were found for the rest of the sample, ranging from a linear decay throughout the film to a second, smaller maximum in the Ar content.

TEM investigation revealed that the differences in the Ar mole fraction are in fact linked to structures features of the pseudo-γ aluminum oxide phase. For both samples under investigation in the TEM, a multilayer structure was found at the interface to the substrate with high argon mole fractions up to 10 at%. For the rest of the sample, different structures were found for the sample with higher and lower hardness. The high hardness sample showed columnar grains with a constant Ar mole fraction at ≈ 2 at%, whereas the low hardness sample showed much smaller grains with decreasing Ar mole fraction towards the top of the film.

In terms of electrical characterization, two different contacting methods were successfully applied, using DC sputtered Au contacts and $Ti_{0.33}Al_{0.67}N$ contacts deposited using HIPIMS. Such contacts showed low ohmic electrical resistance values at room temperature and semiconducting behavior in temperature dependent measurements. The same samples were also used to determine the ratio of the thermopower of pseudo-γ aluminum oxide to its heat conductivity, revealing a positive sign of the thermopower.

Temperature dependent measurements of the electrical resistance were also performed on samples with $Ti_{0.33}Al_{0.67}N$ on top of pseudo-γ aluminum oxide. All samples showed curved lines in Arrhenius plots of the electrical conductivity as is expected for a polycrystalline semiconductor. By carefully choosing the right model to explain the curvature of the reference samples, it is possible to gain insight on the structural features that are essential for the applied model, such as grain structure and homogeneity of the films.

For further use of pseudo-γ aluminum oxide as a transparent conductive oxide, the possibility to transfer the structure to different substrates was successfully investigated. Films were deposited on WC substrate as a reference and on electrically insulating SiO_2, leading to the same pseudo-γ aluminum oxide phase in both cases. All applied methods of characterization such as x-ray diffraction (XRD), SEM and SEM EDX showed that the pseudo-γ aluminum oxide layers are identical and do not depend on the substrate material.

Future work still needs to be done on the optimization of the contacting procedure of the pseudo-γ films. Especially the deposition of structured contacts on samples with insulating SiO_2 substrates is important to determine electrical resistivity and absolute thermopower values that can lead to a deeper understanding of the pseudo-γ aluminum oxide phase. Due to its cheap materials, pseudo-γ aluminum oxide is an excellent candidate for future use as a transparent conductive oxide.

Zusammenfassung

Wolframcarbid (WC) ist aufgrund seiner hohen Härte und Reibungsfestigkeit ein weit verbreitetes Material für Schneidwerkzeuge. Bei hohen Temperaturen (z.B. durch Reibung beim Schnittprozess) tritt Oxidation auf und die stabile Phase von Wolframcarbid wird in eine pulvrige Phase umgewandelt.
Um Oxidation zu vermeiden und die Lebensdauer des Werkzeugs zu erhöhen, werden einzelne oder mehrere Schutzschichten aus verschiedenen Oxiden und Nitriden auf WC-Substrate aufgebracht. Bei Abscheidung mittels physical vapor deposition (PVD) Prozessen (bspw. Magnetron- Sputtern) wird ein Vorspannungspotential an das Substrat angelegt, um die für den Wachstumsprozess erforderliche Oberflächenenergie zu erreichen. Beim Aufwachsen von isolierenden Schichten (wie den meisten Metalloxiden) wird das effektive Vorspannungspotential während des Wachstums verringert, was zu einer schlechteren Kristallinität führt.
Die Entwicklung eines halbleitenden Oxids mit herausragenden mechanischen Eigenschaften für Beschichtungsanwendungen ist daher von großem Interesse.

In dieser Arbeit wurde Aluminiumoxid auf Wolframcarbidsubstrat abgeschieden, wobei Dual-Magnetron-Sputtern (DMS) mit Argon als Sputtergas verwendet wurde. Die Abscheidungsbedingungen während des Wachstumsprozesses werden durch viele verschiedene Parameter definiert. Es wurde eine Kombination aus Argon- und Sauerstoffdruck während des Sputterns zusammen mit dem Vorspannungspotential und der Substrattemperatur identifiziert, die zu einer elektrisch leitfähigen Aluminiumoxidphase führt.

Ziel dieser Arbeit war es, die leitfähige Aluminiumoxidphase hinsichtlich der strukturellen und elektrischen Eigenschaften zu analysieren. Neben der verbesserten Qualität verschleißfester Beschichtungen für Schneidanwendungen ist leitfähiges Aluminiumoxid ein interessantes neues Mitglied der transparenten leitfähigen Oxide (TCO). Große Forschungsanstrengungen werden unternommen, um einen Ersatz für Indiumzinnoxid (ITO) zu finden, da es aus teuren und seltenen Materialien besteht. Ein leitfähiges Aluminiumoxid benötigt hingegen nur leicht verfügbare Materialien und ist daher ein hervorragender Kandidat, um bei zukünftigen TCO-Entwicklungen eine wichtige Rolle zu spielen.

Die in dieser Arbeit analysierte Proben wurden von der Walter AG in Tübingen zur Verfügung gestellt. Die Proben bestehen aus WC-Substrat mit Verschleissschutzschichten aus Aluminiumoxid, abgeschieden mittels DMS. Eine Teil der Proben wurde mittels Hochleistungsimpuls-Magnetron-Sputtern (HIPIMS) mit einer zusätzlichen $Ti_{0.33}Al_{0.67}N$-Schicht beschichtet.

Die Struktur der leitfähigen Phase wurde als ungeordnete kubische Struktur identifiziert aus Aluminium und Sauerstoff, sowie Argon mit Molanteilen bis zu 2.5 at%. Bisher bekannte ungeordnete kubische Aluminiumoxidphasen sind als γ Aluminiumoxid bekannt und sind alle elektrisch isolierend. Um daher die elektrische leitfähige Phase abzugrenzen, wurde der Begriff pseudo-γ Aluminiumoxid eingeführt.
Aufgrund seiner einzigartigen Struktur (bekannt als ungeordneter Spinell) ist es möglich, große Mengen an Edelgasatomen in die Struktur einzubauen. Doch nur beim Wachstum mittels DMS führt der Einbau von Argon zur Bildung der leitfähigen Phase. Die Ar- Atome scheinen die pseudo-γ Phase zu stabilisieren.

Um die Rolle des Argon innerhalb der leitfähigen Phase zu verstehen, wurden die strukturellen Merkmale sowie die elektrischen Eigenschaften der pseudo-γ Phase in dieser Arbeit detailliert untersucht.

Die Charakterisierung der Proben wurde sowohl an Draufsicht- als auch an Querschnittsproben durchgeführt. Die Proben wurden so ausgewählt, dass sie einen breiten Bereich an Probeneigenschaften abdecken, bspw. Probendicke, Vorspannungspotential, aber auch unterschiedliche Härtewerte. Quantitative energiedispersive Röntgen-Spektroskopie (EDX) wurde im Rasterelektronenmikroskop (REM) durchgeführt, um die Ar-Molanteile zu bestimmen und eine Korrelation der Probenhärte mit der Ar-Molfraktion aufzustellen.
Durch genaue Bestimmung des Ar- Anteils in Draufsicht sowie im Querschnitt konnte der Ar-Anteil erfolgreich mit der Probenhärte korreliert werden. Dies zeigt, dass die Ar- Atome für die Bildung der stabilen Struktur wesentlich sind. Zudem konnte mittels Röntgendiffraktometrie (XRD) beobachtet werden, dass die Gitterkonstante der Struktur umso größer wird, je mehr Ar in die pseudo-γ Phase eingebaut wurde.
In REM-EDX Linescans an Querschnittproben wurde eine inhomogene Ar-Verteilung festgestellt. Der höchste Ar-Anteil wurde immer an der Grenzfläche zum WC-Substrat gemessen. Für den Rest der Probe wurden unterschiedliche Argonprofile gefunden, die von einem linearen Abfall im gesamten Film bis zu einem zweiten, kleineren Maximum des Ar-Anteils reichen.
Untersuchungen im Transmissionselektronenmikroskop (TEM) ergaben, dass die Unterschiede im Ar-Molanteil tatsächlich mit den Strukturmerkmalen der pseudo-γAluminiumoxidphase zusammenhängen. Für die im TEM untersuchten Proben wurde eine Mehrschichtstruktur an der Grenzfläche zum Substrat mit hohen Ar-Molanteilen bis zu 10 at% gefunden. Für den Rest der Probe wurden unterschiedliche Merkmale für die Probe mit höherer und niedrigerer Härte gefunden. Die Probe mit hoher Härte zeigte säulenförmige Körner mit einem konstanten Ar-Molanteil bei $\approx$ 2 at%, während die Probe mit geringer Härte kleinere Körner mit abnehmendem Ar-Molanteil zur Oberseite des Films zeigte.

Im Hinblick auf die elektrische Charakterisierung wurden zwei verschiedene Kontaktierungsmethoden erfolgreich angewendet, sowohl DC-gesputterte Au-Kontakte als auch mit HIPIMS abgeschiedene $Ti_{0.33}Al_{0.67}N$-Kontakte. DC-Au-Kontakte zeigten niedrige ohmsche Widerstandswerte bei Raumtemperatur und halbleitendes Verhalten bei temperaturabhängigen Messungen. An denselben Proben wurde auch das Verhältnis der Thermokraft zur Wärmeleitfähigkeit von pseudo-γ Aluminiumoxid bestimmt, wobei ein positives Vorzeichen der Thermokraft festgestellt wurde.
Temperaturabhängige Messungen des elektrischen Widerstandes wurden auch an Proben mit $Ti_{0.33}Al_{0.67}N$ auf pseudo-γ Aluminiumoxid durchgeführt. Alle Proben zeigten in Arrhenius-Diagrammen gekrümmte Linien der elektrischen Leitfähigkeit, wie sie für einen polykristallinen Halbleiter erwartet werden. Durch die sorgfältige Auswahl des richtigen Modells zur Erklärung der Krümmung können Einblicke in die für das angewandte Modell wesentlichen Strukturmerkmale wie Kornstruktur und Homogenität der Filme gewonnen werden.

Für die weitere Verwendung von pseudo-γ Aluminiumoxid als TCO wurde die Möglichkeit untersucht, die Struktur auf verschiedene Substrate zu übertragen. Dünne Aluminiumoxid Filme wurden auf WC-Substrat (als Referenz) und auf elektrisch isolierendem SiO_2 abgeschieden, was in beiden Fällen zur gleichen pseudo-γ Aluminiumoxidphase führte. Alle angewandten

Charakterisierungsmethoden wie XRD, REM und REM EDX zeigten, dass die abgeschiedenen Aluminiumoxidfilme identisch sind und nicht vom Substratmaterial abhängen.

Die Optimierung des Kontaktierungsverfahrens für pseudo-γ Aluminiumoxid Schichten gilt es weiterhin zu optimieren. Insbesondere die Abscheidung strukturierter Kontakte auf Proben mit isolierenden SiO_2-Substraten ist wichtig, um den spezfischen elektrischen Widerstand und die absoluten Thermokraftwerte zu bestimmen. Aufgrund seiner günstigen Ausgangsmaterialien ist pseudo-γ Aluminiumoxid ein hervorragender Kandidat für den zukünftigen Einsatz als transparentes leitfähiges Oxid.

Thesis Structure

This thesis consists of three parts and nine chapters in total.

- **Part I: Transparent conductive oxides and pseudo-γ aluminum oxide**
    - *Chapter 1* gives an introduction to transparent conductive oxides and their physical properties. The current state of research is presented as well as an overview of TCO materials, their distinct properties and applications in current technology.
    - *Chapter 2* introduces the family of different aluminum oxide phases, their deposition techniques, crystal structures and properties. In addition, the deposition technique for the pseudo-γ aluminum oxide samples analyzed in this thesis are introduced and an sample overview is presented.
- **Part II: Advanced characterization techniques and sample preparation**
    - *Chapter 3* is an introduction to electron microscopy. The motivation for electron microscopy in general is presented as well as an overview of the instruments that were used in this thesis. Qualitative as well as quantitative techniques are explained in detail for SEM and TEM investigation .
    - *Chapter 4* contains an introduction to sample preparation for electron microscopic investigation. The preparation of plan-view and cross-section samples for SEM is explained in detail, as well as cross-section samples for TEM investigation.
    - *Chapter 5* gives an overview of measurement techniques for accessing the sample properties, e.g. mechanical properties (hardness) and electrical properties (temperature dependent resistance, thermopower).
- **Part III: Structure-property correlation**
    - *Chapter 6* presents the investigation of the role of argon in the formation of the pseudo-γ aluminum oxide phase. Structural analysis using XRD, SEM imaging and quantitative EDX were used to establish a structure-property correlation and link the mechanical properties to structural features of the samples.
    - *Chapter 7* focuses on pseudo-γ aluminum oxide as a TCO. Methods of contacting are introduced and room temperature measurements of the electrical resistance are presented. The optical properties are presented and prove that despite its electrical conductivity, pseudo-γ aluminum oxide remains optically transparent in the visible range.
    - *Chapter 8* shows the result of temperature dependent measurements of the electrical resistance of pseudo-γ aluminum oxide. A detailed investigation of the exact shape of the Arrhenius plots were linked to the structural properties of the samples and a structure-property correlation was established.
    - *Chapter 9* presents in depth TEM investigation on pseudo-γ aluminum oxide thin films. Bright- and dark-field imaging, together with electron diffraction, energy dispersive x-ray spectroscopy and electron energy loss spectroscopy gives insight in the formation process of the hard pseudo-γ aluminum oxide phase. Argon incorporation was successfully linked to the structural formation on a nanometer scale.

Contents

III. Structure-property correlation 33

Part I

Transparent conductive oxides and pseudo-γ aluminum oxide

1. Transparent conductive oxides

1.1. Motivation

The first report on a transparent conductive oxide (TCO) was published as early as 1907, when Bädeker discovered a way to oxidize cadmium and obtain a transparent, yet electrically conductive material [1]. The development of modern electronics in recent years gave rise to a increasing demand for materials that are electrically conductive but do not block the visible light [2].
The wide use of LCD displays or touchscreens in mobile devices demand for a transparent electrode. In these applications, individual pixels or screen areas must be contacted without blocking the emitted light of the screen [3, 4].
In photovoltaic devices, transparent electrodes can be used to increase their efficiency. In contrast to non transparent methods of contacting a solar cell (e.g. printed Ag fingers), transparent electrodes do not cause any shading loss and act as an antireflection coating in addition [5, 6, 7].
A different field of use for TCOs is their application as window coatings. In fact, the first industrial application used TCOs as a resistive heater for aircraft windows, to avoid icing of the windows at high altitude [8]. Their spectrally selective properties (transparent in the optical, absorbing in the infrared) allow TCO coated windows to also act as so-called low emission windows to reduce the energy consumption of buildings [9, 10].
Further areas of application for TCOs can be found in the overviews of Dixon et al. or Ginley et al. [2, 4].

Due to the wide variety of applications for TCOs, it is not surprising that their economic importance is also immense. The market for TCOs as transparent electrodes in displays alone had a volume of US $ 97 billion in 2014, and by 2020 a market volume of US $ 135 billion is expected [2].
In Europe and the US, solar control window coatings are mandated for new buildings, resulting in a multi billion dollar market for TCO window coatings [2]. But the introduction of TCOs into new fields, such as window coatings in the automotive industry, will enhance growth of the overall market for TCOs in the future [11].

1.2. Physical background of TCOs

The electrical conductivity of solids is described by the band model. Due to the overlap of the discrete atomic orbitals, bands of allowed energies for the electrons are formed. For a metal, the electrons can easily move through the crystal due to free energy states in the valence band. For semiconducting materials, the electrons must first be excited from the valence band into the conduction band. In this case, the energy gap E_g between the upper valence band edge E_{VBM} and the lower conduction band edge E_{CBM} must be overcome, for example by the absorption of a photon.
Is the energy band gap larger than ≈ 3.1 eV, photons from the visible spectrum can no longer lift electrons into the conduction band. The photon can traverse the material without being absorbed and the material appears transparent. Table 1.1 shows the band gap energies of some transparent materials.

In the case that no electrons can be lifted into the conduction band, no charge carriers are available for the current transport and the material is an electrical insulator. Although this matches, for example, with SiO_2 (i.e. glass) from Table 1.1, indium tin oxide (ITO) is in fact a good electrical conductor, despite its high band gap energy.

To explain the conductivity of a TCO, the term energy gap has to be used more differentiated and a distinction has to be made between the fundamental band gap (that is the energy difference between valence band and conduction band edge) and the optical band gap (i.e. the lowest energetic allowed optical transition) [2].

Material	Direct band gap [eV]	Reference
SiO_2	7.6 - 9.6	[12, 13, 14]
ITO	3.3 - 3.7	[15, 16, 17]
α Al_2O_3	8.8 - 8.9	[18, 19]
γ Al_2O_3	7.0 - 8.7	[19, 20, 21]

Table 1.1.: Direct band gap energies for various oxides. The variation for each material is due to different characterization methods and variations in the crystal structures.

These two energy gaps can be different, as described for TCOs by the Moss-Burstein effect [22, 23].

When doping a semiconductor, impurities are introduced which provide localized states within the energy band gap. In the case of n-doping (in fact, most TCOs are n-type), these are electron donor levels just below the conduction band edge. As doping increases, the orbitals of the dopant atoms may overlap and form a new band within the original band gap. This newly formed band can also overlap with the conduction band of the host material.

As a result, electrons from the impurity band can be excited to the conduction band with little or (almost) no energy transfer necessary. The Fermi level E_{Fermi} is therefore shifted from the band gap into the conduction band. Instead of the original, fundamental band gap

$$E_g = E_{CBM} - E_{VBM} \tag{1.1}$$

the optical band gap transforms to

$$E_g^{opt} = E_{Fermi} - E_{VBM} \tag{1.2}$$

see also Figure 1.1a.

The electric charge carriers are now provided by the doping atoms. They can move easily within the conduction band and can form an electrical current. Due to energy and momentum conservation rules, optical transitions are only allowed for interband transitions but not for intraband transition. Therefore, free electrons (or to be more general, free carriers) are available for the current transport (due to the small fundamental band gap), but no absorption of photons in the optical range is allowed (due to the large optical band gap).

To compare the electrical properties of a TCO to other conductors, a good way is to take a

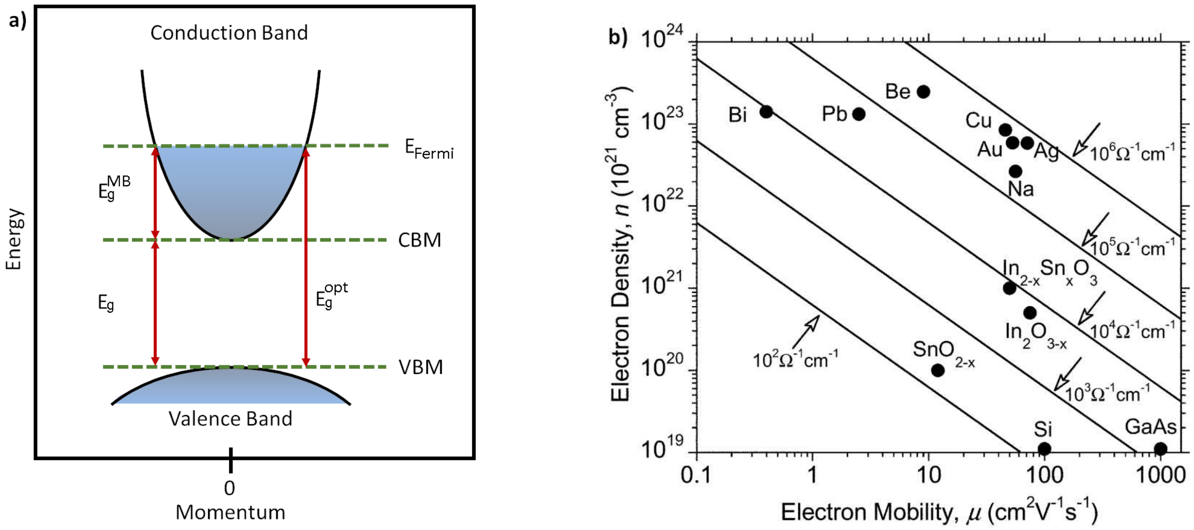

Figure 1.1.: a) Band diagram for the Moss Burstein effect, adapted from [2, 23]. **b)** Classification of electrical conductors according to their electron density and mobility, taken from [24].

look at their free carrier density n and the mobility of these carriers μ. The electrical conductivity σ of a material depends fundamentally on these two properties according to

$$\sigma = ne\mu, \tag{1.3}$$

where e is the carrier's charge. Figure 1.1b gives a map for different conductors according to the carrier density and mobility, see also [24].

Metals are outstanding electrical conductors as they show very high electron mobility as well as high charge carrier densities. Semiconductors show similar carrier mobility as compared to metals, but the carrier density is several orders of magnitude lower. This is due to the source of the free carriers. In a metal, each atom is considered to provide one electron to the charge carrier density. In semiconductors however, the charge carriers are provided by the doping atoms.

Semi-Metals such as Bismuth or Lead provide high electron densities, but very small carrier mobilities.

TCOs are located on this classification map somewhere between metals and semiconductors. Similar in carrier mobility to both, TCOs show lower carrier densities as metals, but higher than semiconductors (as they are heavily doped to form the impurity band).

The reason why not all heavily doped semiconductors are transparent in the visible range and conductive at the same time is due to many-body effects. These effects can reduce the band gap and cancel out the Moss-Burstein effect [25, 26]. In TCOs however, these effects are not strong enough to completely suppress the Moss-Burstein effect, giving rise to their name-giving characteristic features.

1.3. Overview of different TCOs

The historical starting point of transparent conductive oxides were intrinsically doped materials. First industrial applications were made possible by the discovery of Harold McMaster [2, 27], who was able to deposit transparent conductive SnO_2 by means of chemical vapor deposition (CVD).

A few years later, Rupprecht discovered tin-doped indium oxide (ITO), an extrinsically doped TCO [28]. Further development has resulted in many different n-type TCOs, but some p-type TCOs have also been discovered, such as CuAlO, CuGaO, SrCuO, AgInO and ZnO [29]. Particularly noteworthy here are nickel oxides, in which both n-type and p-type conduction was found [30].

The many different TCO materials show distinct electrical properties, such as conductivity, but also differ in their mechanical and chemical properties (e.g. hardness and chemical durability). For industrial applications where considerable quantities of large areas have to be coated, the method of deposition has to be taken into account as well.

From all these different properties and aspects, the best candidate for a specific application can be selected from the family of TCOs. A good overview of the different selection criteria is provided by Gordon [31].

By far the most important representative of TCOs is indium tin oxide (ITO). It shows outstanding electrical and optical properties [32] and can be deposited on large areas [31].

Despite the benefits of ITO, the use of this material is linked to major disadvantages, notably the availability of indium. The global deposits of indium are estimated to run between 15 000 t and 50 000 t respectively (depending on the report), of which more than ⅔ (or ½ respectively) are located in China [33].

The annual demand for indium is about 1000 t per year [33], meaning that any expansion of indium needs will bring existing reserves to their limits within a short amount of time.

In order to cover the high consumption in comparison to the global reserves, in 2013 about half of the indium demand was covered by recycling already (e.g. from ITO sputtering targets).

This shortage has a big impact on the price and especially the price stability of indium. The indium price per kg in 2011 alone ranged from US $ 520 in January to US $ 875 in June [34].

The uncertainties in medium-term availability and price development explain the great interest and multiple research efforts to find alternative material that is equivalent in electrical and optical properties to ITO but does not rely on rare or expensive elements. An overview of the various material systems that are under investigation as an ITO replacement is provided by Minami [35].

But also other approaches, such as insulating glasses with electrically conductive carbon nanotubes are being studied [36].

A new candidate for the TCO family is pseudo-γ aluminum oxide, which is the subject of this work. Right behind oxygen and silicon, aluminum is the third most common element by mass of the earth's crust and in the last ten years the price of aluminum has fluctuated between US $ 1.3 and US $ 2.8 per kg [37]. Together with the already proven deposition method of dual magnetron sputtering, pseudo-γ aluminum oxide does not suffer from the major drawbacks associated with the use of ITO.

The next section gives an introduction to this new and exciting aluminum oxide phase.

2. Pseudo-γ aluminum oxide thin films

2.1. Aluminum oxide phases

2.1.1. Overview

Various forms of aluminum oxides exist that show outstanding mechanical and electrical (i.e. insulating) properties. Together with the easy availability of aluminum as a raw material, this led to an extensive use of aluminum oxide in a wide variety of applications.

Due to its high energy band gap, aluminum oxide is well suited as a gate-dielectric material in Si-transistor fabrication. Aluminum oxide is chemically stable and survives the Si processing steps without damage [38, 39]. But it is also possible to use aluminum oxide layers as diffraction barrier [40, 41], in display production [42], or also in long-term [43] or even short-term storage media [44].

The aluminum oxide thin films investigated in this work were deposited as wear protection coatings on cemented tungsten carbide (WC) substrates. Cemented WC has outstanding mechanical properties (especially a very high hardness), but decomposes by oxidation into a powdery phase. γ aluminum oxide is particularly suitable as a protective coating for WC based tools, due to the low thermal conductivity ($6\,\frac{\mathrm{W}}{\mathrm{m\,K}}$ over a wide temperature range [45]), oxidation resistance [46] and the very high hardness (for γ aluminum oxide Gao et al. report 2837 Vickers [47]).

For the deposition of aluminum oxides, both chemical vapor deposition (CVD) and physical vapor deposition (PVD) can be used. The disadvantage of CVD processes is the high process temperature (substrate temperature above 1000 °C), which has a negative effect on the adhesion of the coating to the substrate due to the cooling process [48].

In response to this, PVD deposition techniques became more and more popular since the deposition temperature is much lower in comparison to CVD.

2.1.2. α aluminum oxide and the transition phases

Different aluminum oxide phases occur in nature e.g. in the form of orthohydroxide ($Al(OH)_3$) as well as metahydroxide ($AlO(OH)$), where both groups can still be divided into different modifications, which differ in their crystal structure.

Upon heating, these starting materials can deoxidize and, depending on the starting material, develop different transition phases at different transition temperatures, see Figure 2.1a.

A total of 24 phases of aluminum oxide are known, which can be further subdivided into the α series (α, κ, χ) and γ series (γ, η, δ, θ) [52]. The α series has rhombohedral symmetry with hexagonal close packed oxygen anions, see also Figure 2.1b [53]. Regardless of the starting material and the corresponding series of transition phases, the α phase is the transformation endpoint for heating above about 1400 K [50], see also Figure 2.1a.

Besides the technical applications of (not exclusively but also) α aluminum oxide, there exist two varieties of the α aluminum oxide phase that can be found in nature, best known as sapphire or, when doped with Chromium, ruby.

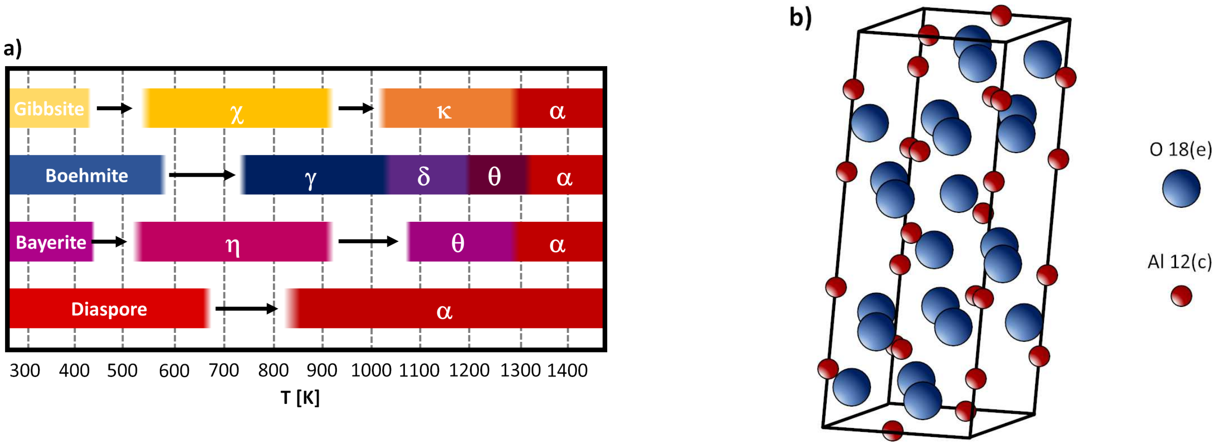

Figure 2.1.: a) Transition diagram for different aluminum oxide phases during heating, adapted from [49, 50]. **b)** Unit cell of α aluminum oxide according to [51].

2.1.3. γ aluminum oxide

The transition phases of the γ series is created by heating boehmite. However, γ aluminum oxide has also been created by other methods, for example by small particle plasma spray [45], low power plasma thermal spraying [47] or inverted cylindrical magnetron sputtering [54].
The starting point to explain the crystal structure of γ aluminum oxide is the cubic Mg_3O_4 spinel. Starting from this structure, the Mg atoms are removed from their positions and Al atoms are placed on the empty spaces. However, to preserve the Al_2O_3 stochiometry, 3 of the 24 cation sites must remain vacant, see Figure 2.2. This leads to partially unoccupied sublattices of the tetrahedrally and octahedrally coordinated aluminum positions. The exact distribution of

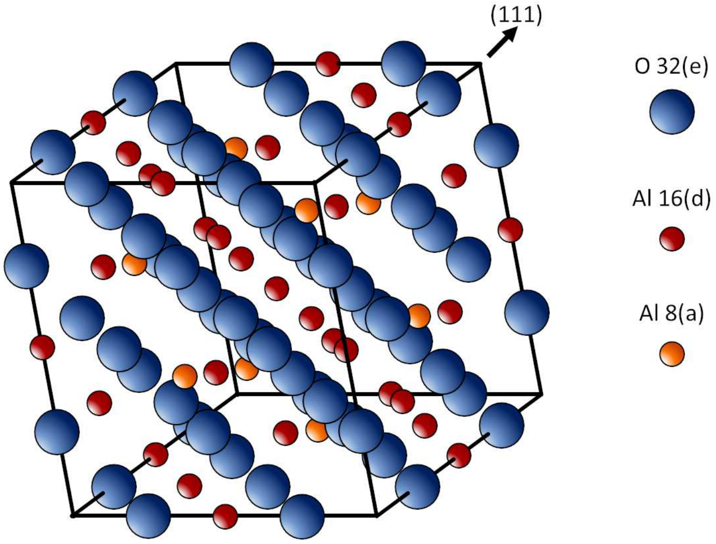

Figure 2.2.: Unit cell of γ aluminum oxide, colorized adaption from [49].

Al atoms on these sublattices and to what extent the actual crystal structure deviates from the idealized defective spinel structure, is still under debate.
Based on the comparison of x-ray and neutron diffraction experiments, Snyder and Zhou at-

tributed the structural disorder of γ aluminum oxide to a disordered Al sublattice [49]. However, the structure they determined could not satisfactorily explain the experimental results, the mismatch of their Rietvield analysis lead to a remaining error of 10%.
Further experimental studies by means of x-ray diffraction (XRD), electron energy loss spectroscopy (EELS), TEM imaging and diffraction and theoretical ab initio calculations were unable to clarify the structure of γ aluminum oxide beyond doubt [21, 55].

2.1.4. Pseudo-γ aluminum oxide

Pseudo-γ aluminum oxide was first described in 2011 by Engelhart et al. [56]. Using dual magnetron sputtering (DMS), they deposited thin films of aluminum oxide which structure could not be assigned to any of the known phases of the aluminum oxide system. The best match was found for the γ phase, which is why the concept of pseudo-γ aluminum oxide was introduced. The three important points in which the pseudo-γ phase differ from the known γ phases will be briefly presented here:

1. Electron diffraction of pseudo-γ in the TEM showed both crystalline and amorphous features (i.e. high amorphous background and small intensity Bragg peaks). The crystalline spots only occurred for lattice spacings smaller than $d_{max} = 2.04$ Å. Engelhart et al. showed by dark-field images in TEM that the grains of polycrystalline pseudo-γ aluminum oxide contribute to both amorphous-like diffraction and crystalline spots simultaneously [56].
2. Even for the standard-γ phase, the analysis using XRD is very demanding and no final crystal structure has been reported so far. Although Zhou and Snyder attributed the disorder to the Al sublattice, the exact defect positions remain unclear and reports are inconsistent [21, 49, 55, 57, 58]. For pseudo-γ, the XRD diffractogram is even worse in terms of crystallinity. Compared to the data of Zhou and Snyder, the pseudo-γ phases show only few, broad peaks low in intensity on a very high background [56].
3. The pseudo-γ phases were deposited by dual magnetron sputtering, with Ar serving as the sputtering gas. TEM energy dispersive x-ray spectroscopy (EDX) clearly showed that Ar was incorporated into the aluminum oxide phase, which might stabilize the crystal structure of pseudo-γ aluminum oxide and affect the hardness of the material. Engelhart determined a mole fraction ratio ${}^{Al}/_{Ar}$ of 17 (corresponding to about 40.0 at% Al and 2.3 at% Ar). Standard-γ does not contain any Ar, but residual hydrogen is found in the structure as a remnant of the starting material [49].

The incorporation of Ar into the aluminum oxide structure can greatly affect its properties. In other material systems, the influence of Ar on the structure and properties has already been investigated. For example, in Bi_2Te_3 and Sb_2Te_3 thin films, a reduction in thermal conductivity was achieved by Ar incorporation [59]. In bulk Bi_2Te_3, a natural nanostructure was generated as well as removed by sputtering with Ar ions.
Since its first publication, other groups have investigated aluminum oxide films with similar features as observed for the pseudo-γ phase of Engelhart. Particularly noteworthy here are Kumar et al., who have achieved similar TEM electron diffraction results in DC sputtered γ aluminum oxide [60]. However, they did not find Ar in their structure, despite using an O_2 and Ar atmosphere during sputtering.

Even before Engelhart coined the term pseudo-γ aluminum oxide, Sridharan et al. performed TEM diffraction analysis on magnetron sputtered γ aluminum oxide, using Ar as a sputtering gas [61]. Like Engelhart, they observed amorphous and crystalline features in TEM diffraction patterns and attributed both features to the grains and not to an amorphous phase. Unfortunately, they do not report on any investigation on the chemical composition with respect to Ar.

2.2. Sample fabrication

2.2.1. Dual magnetron sputtering

Pseudo-γ thin films were deposited using reactive dual magnetron sputtering (DMS) in a Hauzer HTC1000 equipment [62]. A review of DMS in general can be found in [63].
Aluminum was provided by pure metallic targets (size $\approx 81.5\,\mathrm{cm} \times 16.0\,\mathrm{cm}$), arranged on two opposite sides of the sputtering chamber, see Figure 2.3. Sputtering power was set to $6\,\frac{\mathrm{W}}{\mathrm{cm}^2}$.
The sputtering chamber is evacuated and partly filled with oxygen and argon. Due to collisions with electrons, the Ar atoms are first excited and finally ionized. The positive ions are then accelerated towards the negative cathode and free Al ions are created upon impact.
These Al ions can condensate on the substrate, where they react with oxygen from the residual gas and form aluminum oxide (reactive sputtering).
During the sputtering of the aluminum target, secondary electrons are created, necessary to keep up the ionization process. Magnets behind the target create a magnetic field parallel to the target surface, forcing the secondary electrons on a helical movement. This results in a higher electron density right above the target surface and enhances the deposition rate.
During the sputtering process, both metallic targets change their polarity simultaneously,

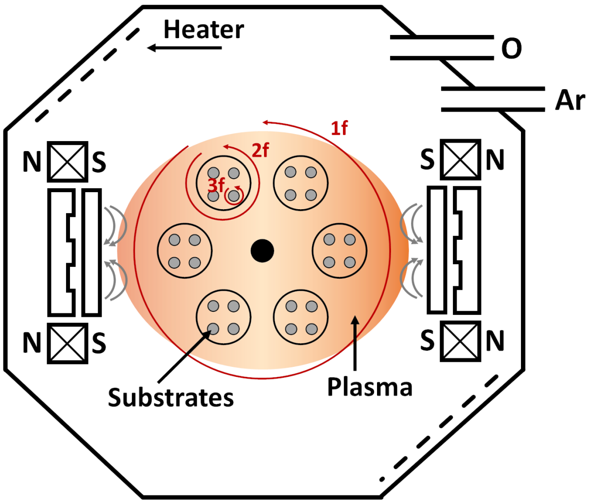

Figure 2.3.: Sketch of a Hauzer HTC DMS sputtering chamber. The three possible sample rotation axes are shown by red arrows. Figure adapted from [64]

switching from cathode to anode and vice versa. This prevents oxidation of the metallic targets, improves the deposition quality and extends the long term process stability [63].
Oxygen partial pressure was kept constant at 0.1 Pa during the sputtering process, while the sputtering gas (argon) was kept at 0.5 Pa. As a substrate, mirror polished cemented tungsten carbide was used. During deposition, the substrate was kept at 500 °C. To control the thickness of the deposited layer and to achieve a homogenous coverage of the whole substrate surface, the substrates are rotated during the sputtering process.
As shown in Figure 2.3, the samples are mounted on drums. If only the overall and the small drum are moving, the samples are labeled as twofold rotated (2f). In addition, an extra rotation can be turned on to rotate the samples around their mounting axes. These samples are called threefold rotated (3f), and experience a reduced film growth (in terms of thickness), but a homogeneous growth on all sides of the substrate.

2.2.2. High power impulse magnetron sputtering

A subset of the samples analyzed in this thesis was covered with an additional $Ti_{0.33}Al_{0.67}N$ layer (in the following labeled TiAlN) on top of the aluminum oxide layer. For their intended use as wear resistive coatings, multilayer coatings of oxide and nitride layers can improve the long term stability of cutting tools [65, 66]. In this work, the TiAlN layer proved to be a good electrical contact for the aluminum oxide layers.
The deposition techniques used for the nitride layers was high power impulse magnetron sputtering (HIPIMS). Using this technique, the sputtering process is run using a pulsed power supply, reaching higher peak power densities in comparison to DMS [67]. Nitride layers deposited by HIPIMS show an improved film to substrate interface and no voids within the films [68].

2.2.3. Sample overview

The samples under investigation in this thesis were provided by Walter Ag Tübingen. Figure 2.4 shows a sketch and photograph of sample 4:S3S1. The goal was to analyze the crystal structure and the role of argon in forming the conductive pseudo-γ phase.

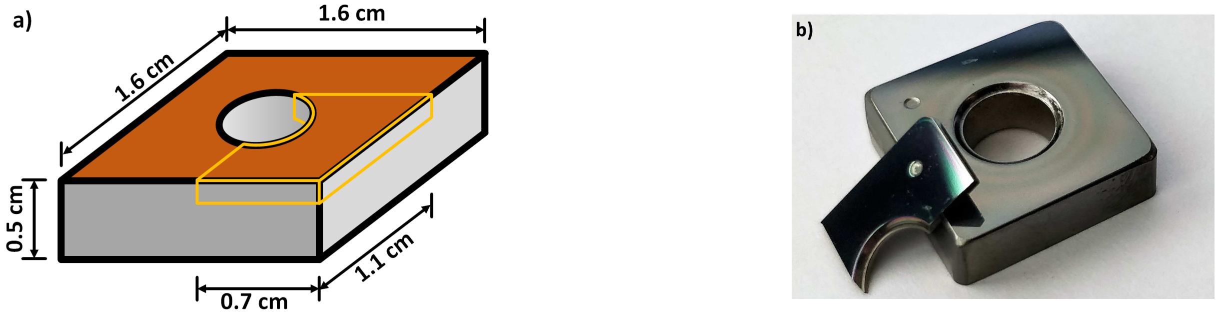

Figure 2.4.: a) Sketch of the samples with the WC substrate in gray, the deposited film is shown in red. The hole in the middle is for mounting the sample during deposition. Samples are cut along the indicated yellow line for smaller cryostat samples. **b)** Photograph of full- and cryostat samples of sample 4:S3S1.

In total, four different series of samples were provided, each putting emphasis on a different feature for the investigation. The name of each sample is of the form *n:SxSy*, where *n* is the overall sample number, *x* the number of the series and *y* the sample number within its series. The sample hardness (HV and Youngs' modulus) was determined by Walter Ag.

- Series 1 covers a wide range of hardness values, starting from a low hardness sample (2:S1S2) to a good sample with high hardness (1:S1S1), see Table 2.1. This allows the investigation of possible correlation in e.g. the crystal structure or the Ar mole fraction for low and high hardness samples.

Series	Sample ID	Batch	Material by DMS	Deposition bias [V]	Sample mounting	Young's modulus [GPa]	HV [Vickers]
1	1:S1S1	1	Al_2O_3	-125	2f	323	2268
1	2:S1S2	2	Al_2O_3	-125	2f	270	1618
1	3:S1S3	3	Al_2O_3	-125	2f	271	1947

Table 2.1.: Sample ID and deposition parameters for all samples of series 1. The mechanical properties are given as Young's modulus and Vickers hardness.

- Series 2 provides an additional layer of TiAlN on top of the pseudo-γ aluminum oxide layer, see Table 2.2. The nitride layer acts as a mechanically stable electrical contact for the transport measurements of the pseudo-γ aluminum oxide phase. Hardness measurements revealed compound properties for all samples.

Series	Sample ID	Batch	Material by DMS	Deposition bias [V]	Material by HIPIMS	Deposition bias [V]	Sample mounting
2	10:S2S1	8	Al_2O_3	-125	TiAlN	-100	2f
2	11:S2S2	8	Al_2O_3	-125	TiAlN	-100	3f
2	12:S2S3	9	Al_2O_3	-125	TiAlN	-100	2f
2	13:S2S4	9	Al_2O_3	-125	TiAlN	-100	3f

Table 2.2.: Sample ID, deposition parameters and mechanical properties for all samples of series 2.

- Samples of series 3 all show very high hardness values, but differ in the layer thickness, see Table 2.3. This allows analysis on the thickness dependence of the electrical properties, but also on the structural features of the aluminum oxide films.

Series	Sample ID	Batch	Material by DMS	Deposition bias [V]	Sample mounting	Young's modulus [GPa]	HV [Vickers]
3	4:S3S1	4	Al_2O_3	-125	2f	352	2900
3	5:S3S2	4	Al_2O_3	-125	3f	352	2900
3	6:S3S3	5	Al_2O_3	-125	2f	343	2583
3	7:S3S4	5	Al_2O_3	-125	3f	343	2583

Table 2.3.: Sample ID, deposition parameters and mechanical properties for all samples of series 3.

- For the samples of Series 4, tungsten carbide and oxidized Si substrates were used simultaneously during the deposition process, see Table 2.4. This enabled a detailed microstructural and chemical analysis of the pseudo-γ aluminum oxide film in the TEM and check the possibility to transfer the pseudo-γ phase to different substrates. Hardness and Young's modulus was measured for samples with WC substrate.

Series	Sample ID	Batch	Material by DMS	Deposition bias [V]	Sample mounting	Young's modulus [GPa]	HV [Vickers]
4	8:S4S1:WC	6	Al_2O_3	-90	2f	331	2435
4	8:S4S1:SiO_2	6	Al_2O_3	-90	2f	-	-
4	9:S4S2:WC	7	Al_2O_3	-125	2f	380	2930
4	9:S4S2:SiO_2	7	Al_2O_3	-125	2f	-	-

Table 2.4.: Sample ID and deposition parameters for all samples of series 4. For samples with WC substrate, the mechanical properties are given as well.

The different characterization techniques are described in detail in the following chapter 3. For electrical measurements in the cryostat, small samples were cut out of the full samples, see Figure 2.4b.

Part II

Advanced characterization techniques and sample preparation

3. Electron microscopy

3.1. Introduction

Structural analysis and a following structure-property correlation is elementary to truly understand the origin of characteristic features of the samples. In this thesis, thin films of aluminum oxide and titanium aluminum nitride with film thickness in the micrometer range were deposited on tungsten carbide substrates.
To analyze such small structures, light microscopy is no longer feasible due to the limits of the lateral resolution in the range of hundreds of nanometer. In contrast, electron microscopy enables the study of structural features down to the nanometer scale and even beyond.

In addition to the imaging features of electron microscopy, the interaction of the electrons with the atoms of the sample under investigation gives access to chemical analysis by energy dispersive x-ray spectroscopy (EDX) in SEM and TEM as well as electron energy loss spectroscopy (EELS) in TEM. Table 3.1 gives an overview of the resolution features by electron microscopy techniques applied in this thesis.

Electron mircroscopy technique	Lateral resolution
SEM EDX	1-2 µm
SEM Imaging	100-500 nm
TEM Imaging	<1 nm
TEM EDX/EELS	1-25 nm

Table 3.1.: Lateral resolution of different electron microscopy techniques used in this thesis.

Only by extensively applying both SEM and TEM techniques, it was possible to establish a structure-property correlation for the pseudo- γ thin films, that were analyzed in this thesis. Special care was taken to prepare high quality samples for the microstructural analysis. With this it was possible to perform e.g. EDX linescans that trace the elemental distribution across the aluminum oxide films, determine the chemical composition of the films and reveal a multilayer structure at the interface between the aluminum oxide film and the WC substrate.
In addition to the microstructural features, mechanical (i.e. hardness) and electrical (e.g. resistance vs temperature) properties were measured.
Structure-property correlation was established based on this data that gives a deeper understanding of the aluminum oxide films and enables the development of a road map for further investigation and film development.

3.2. Scanning electron microscopy (SEM)

3.2.1. Imaging

All SEM investigation for this thesis was performed using a Philips XL30, shown in Figure 3.1a.
In case of the Philips XL30, primary electrons are generated using a field emission gun and can

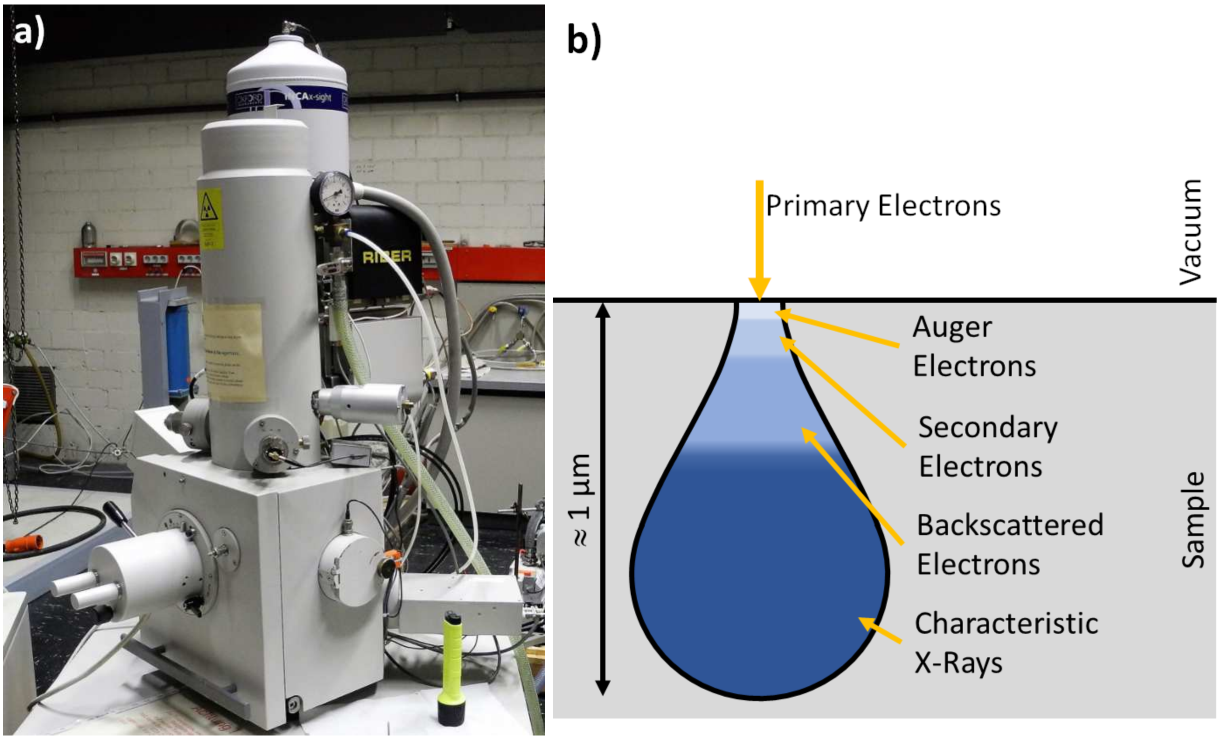

Figure 3.1.: a) Photograph of the Philips XL30 SEM that was used for this thesis. **b)** Sketch of the excitation volume and electron-sample interaction in a SEM.

be accelerated to energies ranging from 2 to 30 keV. The electron energy is an important parameter that has to be chosen carefully to the imaging mode or the quantitative chemical analysis.
The electrons are focused by magnetic lenses in the microscope column to a fine spot of only a few nm in diameter. This spot can then be rastered across the sample. Since the exact position of the spot on the sample is known to the instrument, it can take the recorded signal and construct an image out of the localized information.
Any signal that can be acquired via the SEM is generated by the interaction of the incoming electron beam (the primary electrons) and the sample's atoms.
When an electron hits the sample, it will scatter from the sample atoms until it lost all its energy or left the sample after multiple scattering events. Figure 3.1 illustrates the excitation volume within the sample. Even though the primary beam has only a few nm in diameter, the excitation volume can extend to the micrometer range due to the scattering process. The actual extent of the excitation volume can be controlled by the energy of the primary electrons.
One possible signal that can be used in a SEM is based on the secondary electrons, that are generated within the entire excitation volume. Due to their small energies in the eV range, only secondary electrons that are generated close to the sample surface can actually leave the sample and be detected.
Images based on secondary electrons are therefore especially sensitive to the sample surface and highlight the topography of the sample with a good lateral resolution (approx. 50 nm).
A different signal source for SEM imaging are backscattered electrons (BSE). Primary electrons can be scattered (after multiple scattering events) back to the sample surface, having energies of a few keV. Heavy atoms backscatter more electrons than light atoms in the sample. As a result, the contrast obtained by BSE images is much more sensitive to the material of the sample,

but has a worse lateral resolution (approx. 500 nm) in comparison to secondary electron images.

To avoid charging effects that will lead to a poor image quality, the sample under investigation needs to be electrically grounded.
In case the sample itself is not electrically conductive, a thin metallic layer (usually gold) has to be deposited on the sample surface. This layer needs to be thick enough to provide a current path for the electrons to the ground, but thin enough not to dominate the signal generation for the imaging process.
A more detailed explanation of the signal generation in the SEM can be found in [69, 70].

3.2.2. Energy dispersive x-ray spectroscopy

Scattering processes between the primary electrons and the sample atoms can, aside from the generation of secondary electrons, lead to characteristic x-ray radiation. Its generation is based on the same process as in a standard x-ray tube as discovered by Wilhelm Conrad Röntgen [71]. The x-ray spectrum generated in a SEM will show a continuous bremsstrahlung background, but also characteristic peaks originating from distinctive electron transitions within the sample atoms.
X-ray detectors can be sensitive to the x-ray photon energy (EDX) or their wavelength (WDX). WDX has a higher energy resolution in comparison to EDX (by one order of magnitude [70]), but EDX can acquire the whole spectrum at once and is therefore much faster. The Philips XL30 was equipped with a Si(Li) energy dispersive x-ray (EDX) detector from Oxford Instruments.
The characteristic x-rays can be used for a quantitative chemical analysis, but special care has to be taken during acquisition and interpretation of the EDX data.
As a first step, the energy of the primary electrons needs to be higher than the binding energy of the electrons in the sample atoms. If this is not the case for a specific element, no characteristic x-ray emission can be observed, despite the fact that the element is present in the sample. The ionization cross-section for a specific series of x-ray lines of a specific element is zero for energies below the binding energy and has a maximum at an overvoltage of ≈ 3 (i.e. the ratio of the energy of the primary electrons to the binding energy).
Before the acquired spectra can be evaluated, a so called ZAF correction has to be applied, where three effects are taken into account:

- **Z** is the atomic number correction related to the stopping power of the element. Not all incident primary electrons will generate x-ray radiation but will be backscattered. Excited atoms in the sample can release their energy not only in form of an x-ray photon, but also as an Auger electron. These effects depend of the atomic number of the elements and need to be taken into account when performing quantitative chemical analysis.
- **A**: X-rays are generated everywhere within the excitation volume and need to travel through the sample material before they can be detected. Depending on the distance to the sample surface, the probability of absorption increases exponentially and depends strongly on the atomic number of the elements of the material.
- **F**: In some cases, the absorption of an x-ray photon by an atom of the sample can lead to the emission of a secondary x-ray photon characteristic to the absorbing element. As a result, the relative intensities of the x-ray peaks is altered.

All these corrections are performed iteratively to determine the quantitative chemical analysis.

3.3. Transmission electron microscopy (TEM)

3.3.1. Zeiss 912 Omega TEM

For this thesis, a Zeiss 912Ω TEM was used. Figure 3.2a shows a photograph of the microscope and 3.2b a sketch of the electron path through the microscope column.

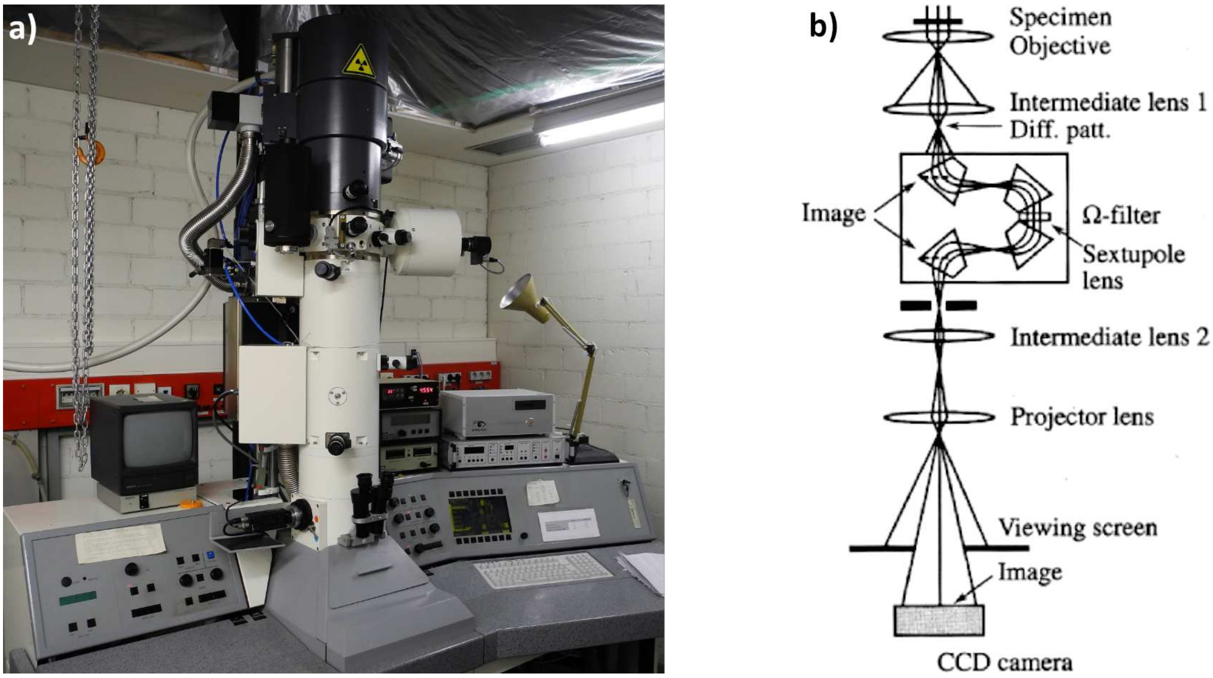

Figure 3.2.: **a)** Photograph of the Zeiss 912 Ω TEM used in this thesis. **b)** Sketch of the microscope column and the electron path.

As an electron source, the instrument is equipped with an LaB_6 filament. The electrons are accelerated to an energy of 120 keV (corresponding to an electron wavelength of 3.35 pm). The Zeiss 912 Ω is equipped with additional features:

- Köhler illumination system to provide an even and parallel illumination of the sample. This illumination system also provides the possibility to switch between wide area illumination and spot illumination [72].
- Low background double tilt holder with a tilting range of ±60°/±30° in the x/y axis.
- Stray aperture was used to reduce hole count artefacts in EDX analysis. Uncollimated electrons can hit the metal apertures of the microscope or a thicker part of the sample and create unwanted x-ray emission. This leads to distortions of the EDX spectra and the quantitative chemical analysis. Using a stray aperture, such unwanted x-ray photons are blocked and cannot reach the detector, enabling high accuracy EDX analysis (<1at%) with lateral resolution in the sub-micron range. This method was established and successfully put to test by Peranio for the analysis of heavy elements in bulk Bi_2Te_3 [73].

- An Si(Li) x-ray detector with an ultra thin window was used to acquire energy dispersive x-ray spectra with an energy resolution of 132 eV at the Mn-$K_{\alpha,1}$ line. The spectra were processed and evaluated for quantitative chemical analysis using the INCA software package [74].
- The Ω energy filter allows many additional acquisition mode in the TEM [75]. The filter generates a 1:1 achromatic image of its entrance plane. All electrons from the entrance image are focused again in the exit plane, but they now have a different angle to the optical axis depending on their energy (or rather their energy loss). All electrons of the same energy will be focused below the image plane at the same point, generating an electron energy loss spectrum that can be used for chemical analysis [76, 77].
  Using a slit aperture, it is possible to only allow electrons with a certain energy loss to contribute to the image. This can be used for energy filtered images and diffraction patterns that show clearer contrast due to the now blocked diffuse background of inelastically scattered electrons.
- The CCD camera features 14 bit intensity resolution and 2048 × 2048 pixel, allowing the acquisition of high quality images with a high dynamic range.

The different acquisition modes that were applied during this thesis are described in the following sections.

3.3.2. Acquisiton techniques and parameters

Different acquisition modes are available when operating a TEM that enable the analysis of different microstructural features or chemical analysis of the sample. For this thesis, different imaging techniques (i.e. energy filtered bright- and dark-field) were used, using the parameters given in Table 3.2.

	Imaging	Diffraction pattern
Condenser Aperture	#3: (MIS Aperture)	#3: (MIS Aperture)
Objective Aperture	#3: 3.5 mrad	-
Selective Area Aperture	-	#3: 700 nm
Width of energy slit aperture	10 eV	10 eV
Magnification	100k / 20k / 50k	-
Camera length		290 mm

Table 3.2.: Acquisition conditions for imaging and electron diffraction in the TEM.

All images were acquired with the 10 eV energy slit inserted, centered around zero energy loss. With this technique, most of the inelastically scattered electrons are removed from the electron beam and cannot contribute (in a negative way due to chromatic aberration of the magnetic lenses) to the image. This improves the contrast quality and resolution of the image greatly [78].

In electron diffraction patterns, the strongest contribution to a diffuse background originates from energy loss due to plasmon excitation [79]. Zero energy loss filtering removes such electrons and improves the contrast in diffraction patterns, leading to a higher accuracy in the structural analysis.

Spectra	Emission current [µA]	Spot size [nm]	Objective aperture[mrad]	Spectrum magnification [x]
Low loss	<1	10	3.5	125
Core loss	3	50	8.1	125

Table 3.3.: Acquisition conditions for low loss and core loss EELS.

In imaging, the energy loss due to inelastic scattering is a parasitic effect. However, it can actually be used for electron energy loss spectroscopy (EELS) to gain chemical insight on the sample. Depending on the energy range under investigation, zero loss spectroscopy (plasmonic losses, energy loss up to approx. 50 eV) and core loss spectroscopy (ionization edges of elements) can be distinguished. Table 3.3 gives an overview of the parameters used for EELS in this thesis.

EELS was performed together with TEM EDX, to combine the advantages of the two different analytical methods. The parameters for the acquisition of the EDX spectra are given in Table 3.4. The samples are tilted by 15° towards the detector to maximize the x-ray yield.

	Emission current [µA]	Spot size [nm]	Acquisition time[s]
Thin sample area	6	50	120
Thick sample area	6	80	120

Table 3.4.: Acquisition conditions for EDX in the TEM.

The different acquisition modes are explained in more detail in the following sections.

3.3.3. Conventional TEM

In principle, conventional transmission electron microscopy relies on two signal sources, (i) the transmitted beam for bright-field imaging and (ii) one (or multiple) diffracted beams for dark-field images [80]. The electrons from the incident beam can scatter elastically (none or negligible energy loss, see section 3.3.4) or inelastically (energy loss due to plasmon excitation or ionization, see 3.3.2).

With increasing sample thickness, more and more inelastic scattering events take place, lowering the energy of the electrons. As a result, the area under investigation has to be very thin (< 100 nm).

Using energy filtering imaging, it is possible to improve the image quality by removing inelastically scattered electrons for thin sample regions. For thicker sample regions, almost all electrons undergo multiple inelastic scattering events and no purely elastically scattered electrons are available for imaging.

The most common acquisition technique for conventional TEM is the so called two beam condition. By tilting the sample with respect to the incoming electrons, (ideally) only one set of crystal planes fulfill the scattering condition and the intensity is maximized in the transmitted and one diffracted beam. Using this technique, the image quality is improved and is especially suitable to image crystal defects [80].

3.3.4. Electron diffraction

Electron diffraction in the TEM is a powerful tool to analyze the crystal structure and orientation of the sample. A detailed investigation can be found in [80].

Diffraction occurs, when the incoming electrons are scattered from the atoms of the crystal structure, leading to constructive and destructive interference of the outgoing electrons, see Figure 3.3. An electron scattered from the upper atom in Figure 3.3 has to travel a shorter distance before and after the scattering event in comparison to an electron scattered from the bottom atom. This leads to a phase shift between the electrons, depending on the displacement of the atoms in the crystal (and therefore the crystal structure). This phenomenon is described by the Bragg equation:

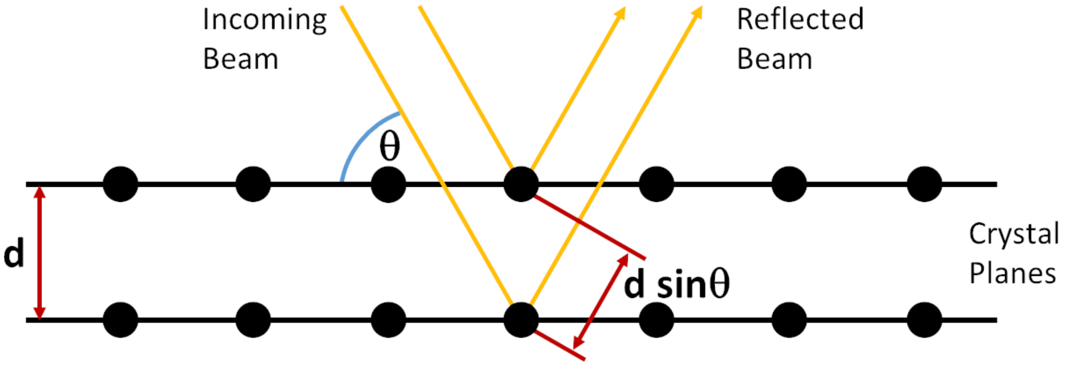

Figure 3.3.: Sketch of Bragg's diffraction mechanism. Two beams with the same wavelength are scattered by periodically arranged atoms.

$$n\ \lambda = 2\ d_{hkl}\ sin(\theta_{hkl}), \tag{3.1}$$

where n is a positive integer, λ the wavelength of the incident wave, d_{hkl} the spacing between two (hkl) lattice planes and θ_{hkl} the Bragg angle [81].

How strongly an atom can scatter an incoming wave in any direction θ is described by the atomic form factor $f(\theta)$. For electron diffraction, the atomic form factor is the Fourier transform of the atomic potential and is therefore different for each element.

In compound materials, where different elements are present within the unit cell of the crystal, the relative location of these elements has to be considered. The addition of all scattered electrons (in terms of amplitude and phase) leads to the kinematic structure factor

$$F_{hkl} = \sum_j f_j(\theta_{hkl})\ exp(2\pi i\ \overrightarrow{G_{hkl}}\ \overrightarrow{r_j}), \tag{3.2}$$

where $\overrightarrow{r_j}$ is the position of the jth atom in the unit cell. The sum is evaluated over all atoms in the unit cell and gives a value F_{hkl} for every possible reflection (hkl).

The intensity I_{hkl} of any (hkl) reflection is directly linked to the square of the structure factor

$$I_{hkl} \propto F_{hkl}^2 \tag{3.3}$$

When using a different scattering technique (e.g. x-ray diffraction), the scattering capability of each element will change in comparison to electron scattering. The intensities of the same (hkl) reflection of the same structure can therefore be different. This makes the combination of different kinds of diffraction experiments a powerful tool to analyze the crystal structure.

In this thesis, x-ray diffraction and electron diffraction in the TEM was used to analyze the crystal structure of the samples.

3.3.5. Analytical electron microscopy

3.3.5.1. Overview

In contrast to conventional TEM modes, where inelastically scattered electrons are blocked as much as possible to improve image quality, analytical electron microscopy relies on the information hidden in the electron energy loss.

In fact, there is a huge amount of information in the inelastic scattering processes that can be used to analyze the sample, especially for chemical analysiss. Two different methods were applied in this thesis:

- EELS takes a closer look at the amount of energies that electrons have lost by their passage through the sample.
- EDX is based on the energy transfer from the primary electrons to the sample atoms, that is released as a characteristic x-ray photon.

3.3.5.2. Energy dispersive x-ray spectroscopy

In TEM EDX, the generation of x-ray photons happens due to the same process as in SEM. Due to scattering with the beam electrons, the specimens atoms can be put in an excited state. One way to release this excitation energy is by emitting a characteristic x-ray photon.

In this thesis, a Si(Li) EDX detector from Oxford instrument was used to record the spectra of these x-ray photons.

In comparison to SEM EDX, TEM EDX provides one major advantage. Since in TEM, the thickness of the sample under investigation needs to be less than 100 nm, absorption and fluorescence effects that take place in thick samples can be neglected. As a result, ZAF corrections are not required. In addition, there is no bremsstrahlung background in the EDX spectra.

This simplifies the quantiative evaluation of TEM EDX spectra in comparison to SEM EDX counterpart. The quantification in TEM EDX is based on the Cliff-Lorimer equation

$$\frac{C_A}{C_B} = k_{AB}\ \frac{I_A}{I_B}, \tag{3.4}$$

where C_A, C_B are the weight percent of elements A and B, I_A, I_B the intensity of the charac-

teristic x-ray lines and k_{AB} is the Cliff Lorimer coefficient [82].
Together with the normative constraint ($\sum C_i = 1$), this methods enables the analysis of the mole fractions ratios of the elements in the sample without the need of a standard to compare the spectra to. In case the k_{AB} is not available for the specific elements A and B, they can be derived from their coefficient to a third element C using

$$k_{AB} = \frac{k_{AC}}{k_{BC}}, \tag{3.5}$$

[83]. Therefore, it is only necessary to keep a list of k_{AB} factors of all elements in reference to one specific element.
The accuracy of this method obviously depends greatly on the values used for the k_{AB} factors. Table 3.5 gives an overview of the k_{AB} factors that were used in this thesis (with Si as the reference element, i.e. $k_{Si} = 1$). Spectra acquisition and evaluation was performed using the INCA software package [74].

Element	Atomic number	X-ray line	Energy [eV]	k factor
O	8	$K_{\alpha 1}$	0.52	2.250
Al	13	$K_{\alpha 1}$	1.48	1.039
Ar	18	$K_{\alpha 1}$	2.96	1.040

Table 3.5.: Cliff Lorimer k factors for quantitative EDX analysis in the TEM for 120 keV primary electrons (values are given with Si as a reference material). k factors taken from INCA software, line energies taken from Zschornack [84]

3.3.5.3. Electron energy loss spectroscopy

Inelastic scattering events occur due to the coulomb interaction of the incoming electrons and the bound electrons within the sample. The scattering event and therefore the energy loss of the beam electron depends on the possible excitations of the bound electrons.
An EELS spectrum can be divided into three regions with respect to the energy loss, depending on the different excitation mechanisms [77].
A major part of the electrons will travel through the sample without any energy loss. In an EELS spectrum, they will form a peak centered around 0 eV, called the zero loss peak.
In the low loss region, the energy losses correspond to plasmonic excitation and interband transitions. Plasmonic energies are characteristic for a specific structure and can serve as a bar code for unknown phases [85].
Even higher energy losses can be linked to inner shell ionization processes and is therefore characteristic for a specific chemical composition. By carefully addressing the shape and energetic position of recorded ionization edges, it is possible to investigate the chemical surrounding of the ionized element, since the electron energies are influenced by the chemical bonds the element is forming with its neighbors (see for example Grunes et al. for the fine structure of the O-K edge [86] or Hansen et al. of the Al L edge [87]).

For EELS analysis, the sample has to be sufficiently thin. In thicker samples, many electrons

will experience multiple scattering events, leading to peaks corresponding to all possible combinations of energy losses in the spectra. To avoid multiple scattering, the sample should be thinner than the mean free path of the electrons.
As an example, the mean free path of 120 keV electrons in Si is about 55 nm [88].

4. Sample preparation

4.1. SEM cross-section and plan-view samples

The accuracy of any electron microscopic study depends on the quality of the sample. Therefore, special care has to be taken to prepare artifact free, high quality samples for SEM as well as for TEM investigation.
One advantage of the SEM is the possibility to analyze bulk samples, as long as they are electrically conductive. In this thesis, two different kinds of SEM sample preparation methods were applied, cross-section and plan-view.
For plan-view (PV) analysis in this thesis, no special preparation step had to be taken to enhance conductivity since all samples were already electrically conductive. To remove any contamination from the sample surface, every sample was put in an ultrasonic ethanol bath for 5 minutes before mounting into to SEM chamber.
For cross-section (CS) analysis, different steps were necessary for samples with tungsten carbide (WC) and SiO_2 substrates.
WC substrate samples were cut and polished at Walter AG to create a flat surface. Since the topographic contrast is strong for secondary electron imaging in SEM, a polished surface will enhance the atomic number contrast and highlight different phases in the images. The cut samples were embedded in an conductive resin to avoid charging effects during imaging.

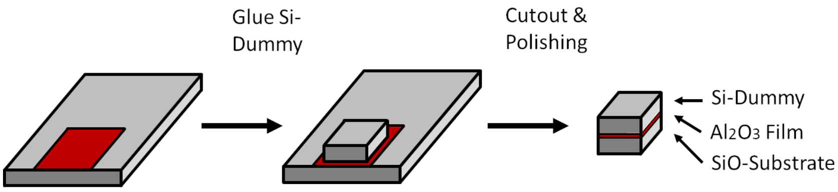

Figure 4.1.: Processing steps for cross-section SEM sample preparation on SiO_2 substrate samples.

Samples with SiO_2 substrate were prepared at the University of Tübingen for cross-section analysis, see Figure 4.1. To enhance the mechanical stability, small 3 mm × 3 mm pieces of a Si wafer were glued on top of the film. Small pieces of approx. 1.5 mm × 3.0 mm were cut from the covered samples using a diamond wire saw.
The small pieces were then polished using a tripod holder and diamond foils with grain sizes from 3 to 0.5 µm. After a cleaning step in an ultrasonic ethanol bath, the sample surfaces were ion etched with 1 kV Ar^+ ions, 3 mA source current for 10 minutes (milling angle 10° from top) to remove any remains from the polishing steps.

4.2. TEM cross-section samples

The cross-section sample preparation for the TEM is similar as for the SEM. In fact, SEM CS samples can be used as a starting point for TEM CS samples.
For TEM investigation, the sample has to be thinned down to 100 nm and even less to be transparent to the electron beam and to avoid multiple inelastic scattering events, see also 3.3.5.3.
SEM CS samples are glued with their polished side on a star holder and diamond foils (grain

sizes 3 to 1 µm) are used to thin down the sample to approximately 20 µm by mechanical polishing.
Further thinning of the samples has to be done using ion etching. The sample is removed from the star holder and glued to an aluminum ring, see Figure 4.2. In the ion mill, the sample is bombarded with Ar^+ ions (3 kV acceleration voltage, 3 mA source current) from the top and bottom at an angle of 12°. The milling process is continued until a hole appears at the interface of the sample and the Si cover. A final polishing step is performed for one hour with Ar^+ ions with a smaller milling angle of 10° and a reduced acceleration voltage of 1 kV.

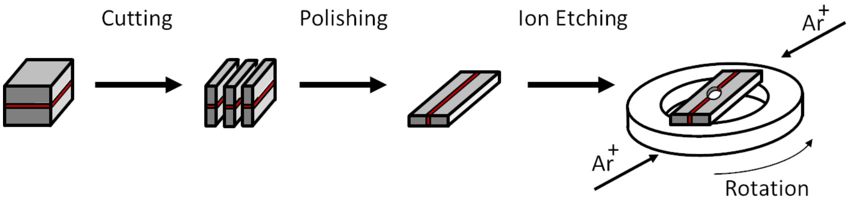

Figure 4.2.: Processing steps for cross-section TEM sample preparation on SiO_2 substrate samples.

5. Property measurements

5.1. Hardness

The original purpose of the pseudo-γ aluminum oxide films was as a wear resistive coating on cutting tools. It was therefore of great interest to determine the mechanical stability of the thin films and link this to other measured properties.

The mechanical properties were determined using nano-intendation by Walter AG. A small tip (Vickers tip) is lowered onto the sample surface and an increasing load is applied. Simultaneously, the displacement of the tip (i.e. the penetration of the tip into the sample under investigation) is measured.

After increasing the load to 15 mN (within 20 s) and waiting for 10 s (creep time), the load was released again within 20 s.

From the recorded load vs displacement data hardness values using the Oliver Parr method can be calculated [89, 90]

$$H = \frac{P_{Max}}{A}, \tag{5.1}$$

where H is the hardness, P_{Max} is the maximum load and A is the area of the indentation caused by the tip. In case of large areas A, it can easily be measured using a light microscope. But in case of very small areas (i.e. that they cannot be measured with a light microscope), it has to be estimated from the contact depth h_c using

$$A = f(h_c) \tag{5.2}$$

$$h_c = h_{Max} - \epsilon \frac{P_{Max}}{S} \tag{5.3}$$

where ϵ is a geometry factor of the tip ($\epsilon = \frac{3}{4}$), h_{Max} is the maximal depth and S is the stiffness which can be calculated from the slope of the displacement curve right after reducing the load. The functional dependence of the area from the contact depth has to be calibrated carefully by independent measurements.

5.2. Electrical properties

Electrical measurements were performed at room temperature using a Keithley 2420 sourcemeter. High accuracy resistance measurements can be achieved by performing a voltage sweep, i.e. by acquiring the current reading of the source meter for a predefined list of increasing voltages. A linear fit can then be used to calculate the slope of the voltage - current readings according to Ohm's law.

The advantage of the sourcemeter is that no additional equipment is needed in the measurement circuit to probe the current (or voltage respectively) through the sample. In addition, in case of low ohmic samples, 4-Wire measurements were performed to reduce the influence of the wires on the measurements result.

In this case, two pair of wires are used, two for the voltage and current reading each, see Figure 5.1a.

In 4-Wire configuration, the voltage measurement is more sensitive to the voltage drop across the sample, since the voltage drop across the wires (for the voltage measurement) is reduced due to a lower current through these wires.

While the resistance at room temperature is essential to probe the electrical properties of a sample, temperature dependent measurements of the electrical resistance gives access to a deeper understanding of the characteristic features of the sample. Temperature dependent measurements were performed on small cut-outs of the samples (approx. 0.5 cm × 1 cm) in an optical cryostat, see Figure 5.1b.

Using liquid nitrogen and a resistive heater, it was possible to measure the resistance (using the 4-Wire setup) across a wide temperature range from 80 K to 300 K.

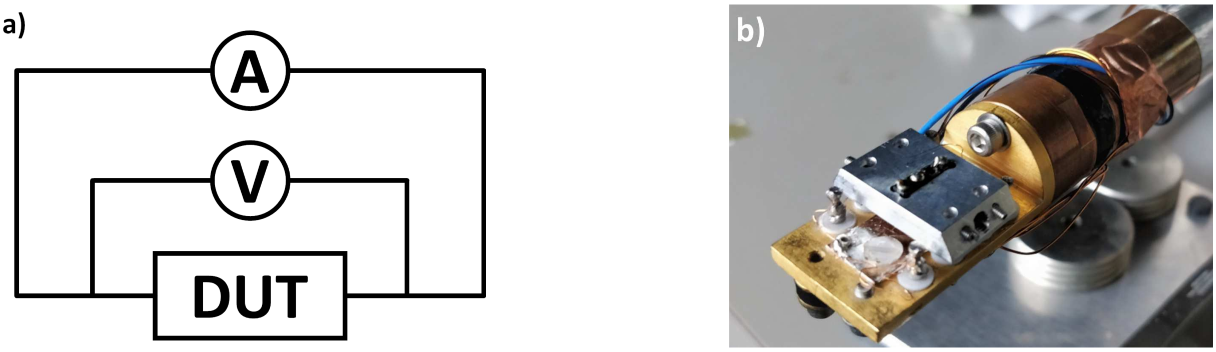

Figure 5.1.: a) Sketch of 4-Wire measurement to precisely measure low ohmic resistance samples. **b)** Photograph of the sample mounted onto the cooling finger of the cryostat.

5.3. Structure-property correlation

For this thesis, various investigation techniques were performed on pseudo-γ aluminum oxide thin films to probe either the structural features (e.g. layer structure, crystal structure, quantitative chemical analysis) as well as mechanical (e.g. hardness) and electrical properties (e.g. resistivity).

To achieve a deeper understanding of the properties and functionality of the samples, the results and insights of single measurements have to be combined in a structure-property correlation, see also Figure 5.2.

This way, mechanical properties such as hardness can be linked to structural features such as Ar mole fraction in the pseudo-γ aluminum oxide film and give an insight on how the Ar incorporation affects the crystal structure of the film.

Only by carefully performing a structure-property correlation, a deeper understanding of the samples is achieved and it is possible to develop a road map for further investigation and sample development.

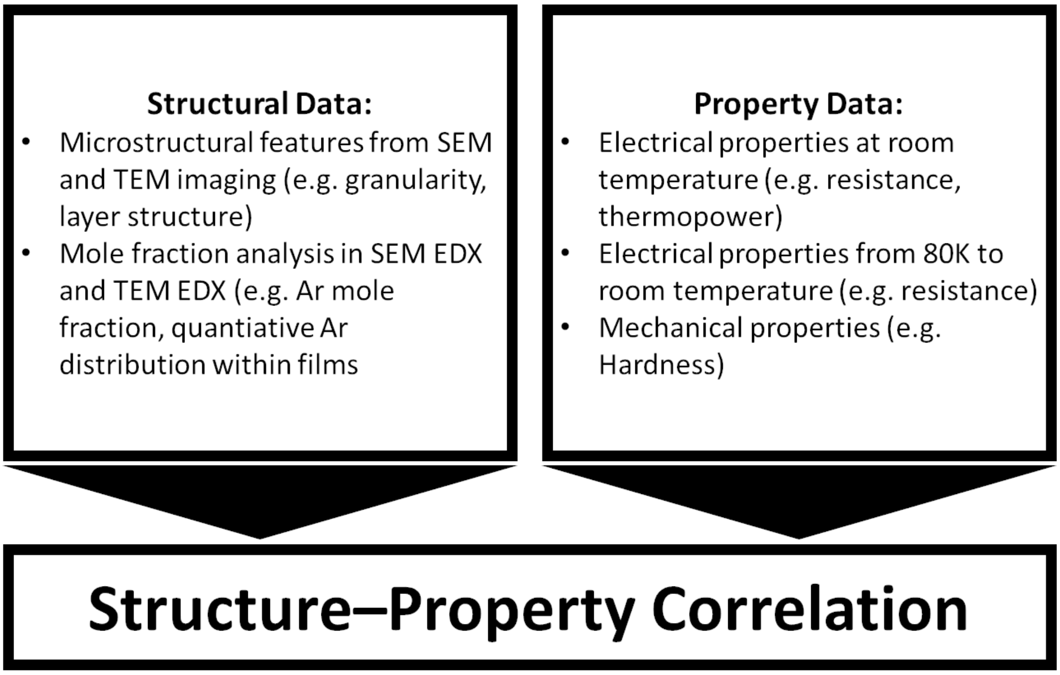

Figure 5.2.: Diagram to highlight the necessary steps for structure-property correlation on pseudo-γ aluminum oxide thin films.

Part III

Structure-property correlation

6. Pseudo-γ aluminum oxide thin films: Argon incorporation, hardness and structure-property correlation

6.1. Introduction

The pseudo-γ aluminum oxide phase was described for the first time in 2011 [56] and is structurally related to a disordered spinel structure [91]. It shows outstanding features in electron diffraction i.e. crystalline spots together with an amorphous-like background. Recent investigations showed that the phase also exhibits outstanding electrical properties and electrical property measurements can contribute to the understanding of the physical properties.
Since structural analysis turns out to be difficult to interpret, other property measurements appeared to be necessary. The electronic structure of γ aluminum oxide was investigated by Ealet et al. [21]. These samples were grown by thermal oxidation of Al in air. Electron diffraction patterns with sharp spots corresponding to the spinel structure were obtained. This structure is in contrast to the findings of pseudo-γ for which such sharp spots are not present [56]. A sketch of the electronic structure for γ aluminum oxide is given in Figure 10b of [21], its relevance, however, is not clear.
Particularly the Ar content was considered to be important. Ar is introduced during deposition by the sputtering process and has a rather large solubility in the defect spinel structure. It was shown unambiguously to be present by EDX in the TEM, Figure 7a in [56]. An $^{Al}/_{Ar}$ mole fraction ratio of 17 was determined, i.e. 40 at% Al yielding about 2.3 at% Ar. We have identified the presence of Ar in various material systems, i.e.

- in the formation of the pseudo-γ phase of aluminum oxide [56],
- in thin films of Bi_2Te_3 and Sb_2Te_3 prepared by sputtering [59],
- in Bi_2Te_3 bulk materials sputtered with Ar, in which a natural nanostructure could be established by sputtering with Ar ions [92]. In addition, other thin film processes were described for which Ar was incorporated into deposited films, i.e. NiO thin films [93].

Since Ar can be used to generate specific material properties its content needs to be measured on a quantitative basis. This was achieved here by EDX analysis in the SEM, which is a standardless analysis. The quantitative analysis of Ar is a key for a better understanding of structure-property relation in pseudo-γ aluminum oxide. X-ray diffraction does not allow for unambiguous answers with respect to the structural analysis, additional chemical analysis gives simple numbers for the Ar content and yields the Ar content over the range of the film thickness.

In the work followed here, the main application of pseudo-γ thin films deposited by PVD are wear resistant coatings. Therefore, improved mechanical properties of the films are of greatest importance. A correlation of the Ar content with the hardness of the coated substrates was the goal of this work. It required that both the Ar mole fraction and the hardness can be measured quantitatively with high accuracy. This is shown to be the case as will be documented in this chapter.

6.2. Experimental procedure

6.2.1. Sample preparation

For the structural analysis in this chapter, samples from series 1,3 and 4 on tungsten carbide substrates were used. More details are given in Tables 2.3, 2.3 and 2.4 in section 2.2.3. The relevant information and film thickness measured in the SEM is given in Table 6.1.

Sample ID	Young's modulus [GPa]	HV [Vickers]	Thickness of Al_2O_3 film [µm]	Roughness of Al_2O_3 film [nm]	Granularity
1:S1S1	323	2268	0.76 ± 0.01	78 ± 14	no
2:S1S2	270	1618	1.47 ± 0.03	157 ± 47	≈ 229 nm
3:S1S3	271	1947	1.64 ± 0.10	160 ± 53	≈ 194 nm
4:S3S1	352	2900	1.64 ± 0.09	68 ± 19	no
5:S3S2	352	2900	0.65 ± 0.04	41 ± 8	no
6:S3S3	343	2583	1.28 ± 0.06	74 ± 20	no
7:S3S4	343	2583	0.56 ± 0.02	30 ± 7	no
8:S4S1	331	2435	1.06 ± 0.06	69 ± 30	no
9:S4S2	380	2930	1.04 ± 0.04	75 ± 30	no

Table 6.1.: Aluminum oxide thin films deposited on WC substrates of series 1, 3 and 4. Deposition bias during magnetron sputtering is given, as well as the sample hardness. The layer thickness, granularity and surface roughness of the films were determined at multiple areas by SEM.

6.2.2. X-ray diffraction acquisition

The x-ray diffraction patterns were acquired by grazing incidence mode (GIXRD) on a diffractometer from Panalytical (Empyrean). Cu-K_α-radiation with line focus was used for the analysis (using 40 kV and 40 mA). The incident beam was defined by a 2 mm mask and a $\frac{1}{8}°$ divergence slit in addition with a x-ray mirror producing a parallel x-ray beam. The sideways divergence was controlled by a Soller slit (0.04°). For the diffracted beam path a 0.18° parallel plate collimator in conjunction with a proportional counter (0D-detector) was used. The measurement was done in grazing incidence mode (Ω = 1°). The 2θ range was 20° to 80° with a step size of 0.03° and a counting time of 10 s.

6.3. Results and discussion

6.3.1. Structural analysis by XRD and SEM

XRD diffractograms were acquired for all samples of all three series (see Figure 6.1). The results are given in Table 6.2. To maximize intensity of the thin aluminum oxide film on the

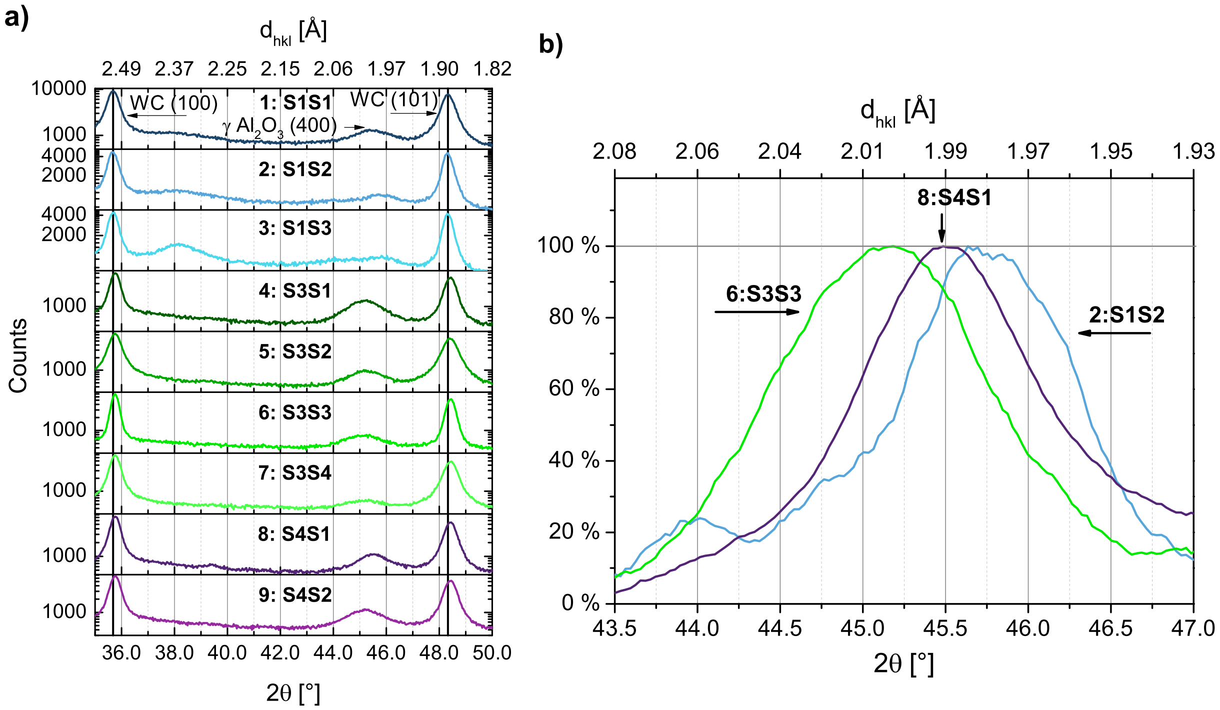

Figure 6.1.: **a)** X-ray diffractograms in grazing incidence geometry for all samples 1-9. The diffractograms are dominated by two peaks originating from the WC substrate (WC (100) and WC(101)), indicated by arrows. All samples show a small, broad peak near 45.5°. **b)** Demonstration of peak shift of the (400) γ aluminum oxide peak for samples 2:S1S2, 6:S3S3 and 8:S4S1. The diffractograms were smoothed by an moving average filter and normalized to 100%

substrate, the diffractograms were acquired in grazing incidence geometry. Due to the small angle between the incoming x-ray beam and the sample surface, it is more surface sensitive as compared to Bragg Brentano geometry.

Each diffractogram is dominated by peaks originating from the hexagonal tungsten carbide (WC) substrate, i) one at $2\theta = 35.68°$ corresponding to the (100) peak of the substrate and ii) at 48.33°, corresponding to the (101) peak respectively. Besides the substrate peaks, only broad peaks with small intensities can be attributed to the aluminum oxide films.

A peak near 2θ 45.5° can be identified in all diffractograms and can be attributed to the (400) peak of pseudo γ aluminum oxide. The center of this peak is slightly shifted for each sample with respect to the other samples (see Figure 6.1b). The corresponding d values to the 2θ show a spread of 1.3%, ranging from 1.977 Å for sample 2:S1S2 and 2.009 Å for sample 6:S3S3.

Extra care has to be taken to analyze the position of peaks with low intensity due to noise and a poor peak-to-background ratio. To address these issues, a nonlinear background subtraction, as well as a combined fit to the (400) aluminum oxide peak and the (101) WC substrate peak was performed. A comparison of the data and the fit is given in the Appendix B. Figure 6.2 shows the 2θ values plotted against the obtained Vickers-hardness and shows a negative linear correlation.

Only for sample 3:S1S3, a peak close to $2\theta = 38.20°$ can be identified that is not visible in the diffractograms of the other samples and is close to the (311) reflection of γ aluminum oxide.

Sample ID	HV [Vickers]	XRD $2\theta_{400}$[°]	d_{400} [Å]	Peak-to-background ratio
1:S1S1	2268	45.47 ± 0.03	1.995 ± 0.001	1.3
2:S1S2	1618	45.76 ± 0.05	1.983 ± 0.002	0.2
3:S1S3	1947	45.90 ± 0.08	1.977 ± 0.003	0.2
4:S3S1	2900	45.19 ± 0.01	2.007 ± 0.001	2.3
5:S3S2	2900	45.23 ± 0.01	2.005 ± 0.001	1.4
6:S3S3	2583	45.14 ± 0.01	2.009 ± 0.001	1.0
7:S3S4	2583	45.18 ± 0.04	2.007 ± 0.002	0.6
8:S4S1	2435	45.52 ± 0.03	1.993 ± 0.001	1.7
9:S4S2	2930	45.21 ± 0.03	2.006 ± 0.001	1.9

Table 6.2.: XRD peak positions of (400) pseudo-γ aluminum oxide peak for all samples 1-9. The peak positions were determined in XRD diffractograms by a combined fit to the film peak near 45° and the WC(101) peak. The corresponding d values are given, calculated from 2θ values and the wavelength of the Cu Kα line. The given error is derived from the fit.

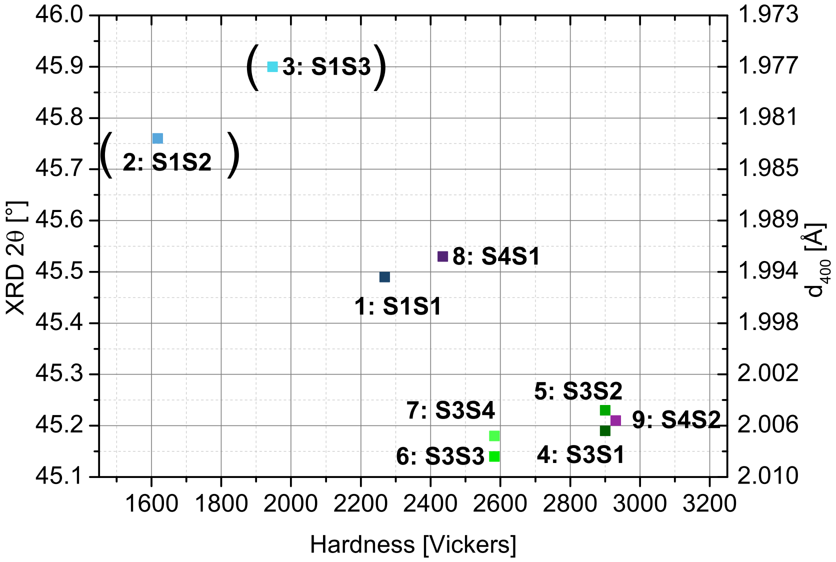

Figure 6.2.: Correlation diagram of the (400) pseudo-γ aluminum oxide peak position in XRD (d_{400} values respectively) vs film hardness. A clear negative correlation can be seen. The data points corresponding to samples 2:S1S2 and 3:S1S3 are in brackets, indicating their poor peak-to-background ratio according to Table 6.2.

All samples were investigated in cross-section in the SEM. The samples are oriented in such a way, that the tungsten carbide substrate is visible at the bottom of the image.
Figure 6.3a shows an overview image at 25000 magnification of sample 1:S1S1, a sample with high hardness. A corresponding high magnification image is shown in Figure 6.3b. This sample is representative for all samples with high hardness: i) over the whole cross-section, the film covers the substrate homogeneously with only small deviations in the film thickness (less than 80 nm, see Table 6.1 and ii) a granular structure is not visible, the film appears dense and mono-

lithic. Figure 6.3c and 6.3d show an overview and close up image of a sample 2:S1S2, which shows less hardness.

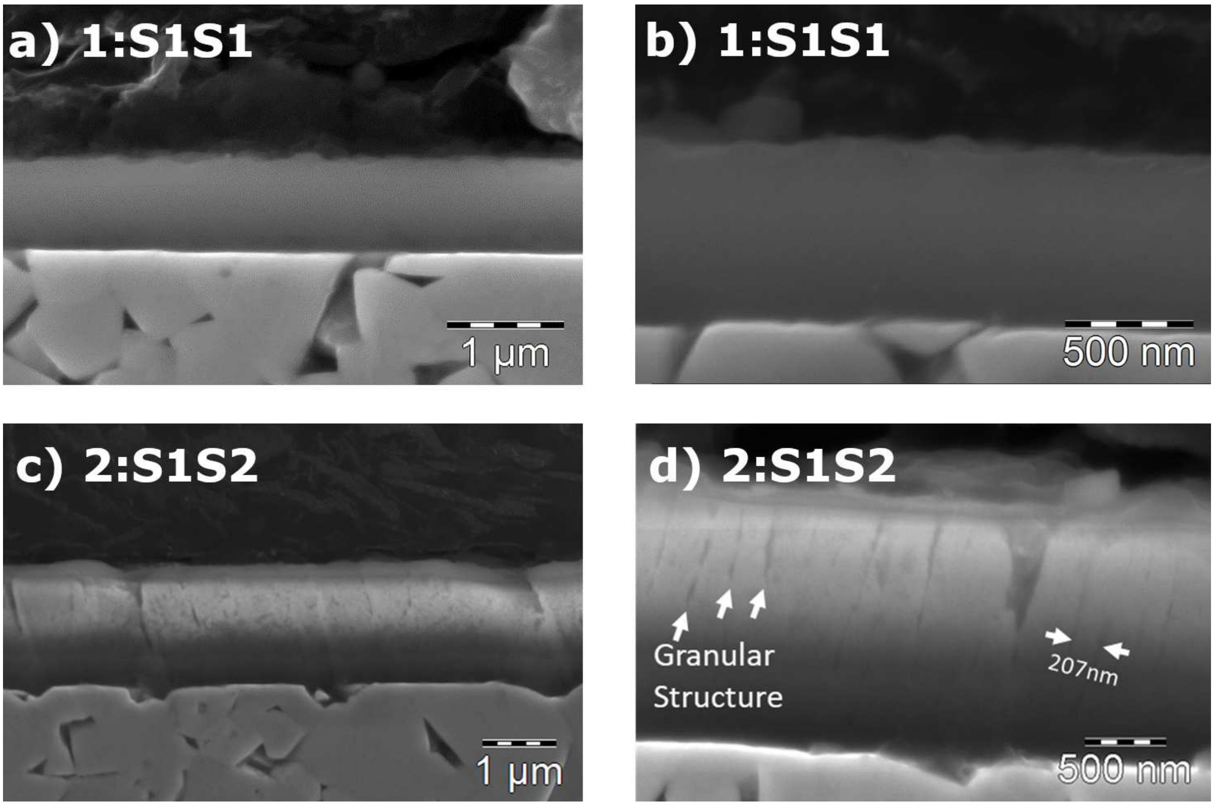

Figure 6.3.: SEM cross-section analysis of sample 1:S1S1(top row) and sample 2:S1S2 (bottom row) in low (left column) and high (right column) magnification. Sample 1:S1S1 shows a homogenous film, while sample 2:S1S2 shows a granular structure with an average granular size of $\approx$ 229 nm.

Again, the substrate was covered over the whole cross-section area by a film with only small variation in film thickness. In contrast to samples with high hardness values, a granular structure, perpendicular to the film can be seen (i.e. parallel to the growth direction). The granular spacing appears to be approximately 229 nm in size. The roughness of the films with low hardness was determined to be in the range of 160 nm (see Table 6.1) and is higher compared to the roughness of high hardness samples.

6.3.2. Chemical analysis by EDX point spectra

EDX spectroscopy in plan-view

Elemental analysis was performed by EDX in the SEM for all samples in plan-view configuration. By adjusting the electron primary energy in a range from 10 keV to 15 keV, the excitation volume of the electron beam can be controlled. The acceleration voltage is increased until the tungsten peak originating from the substrate appears in the spectra. By carefully adjusting the acceleration voltage, the excitation volume can be adjusted to cover the whole aluminum oxide film.

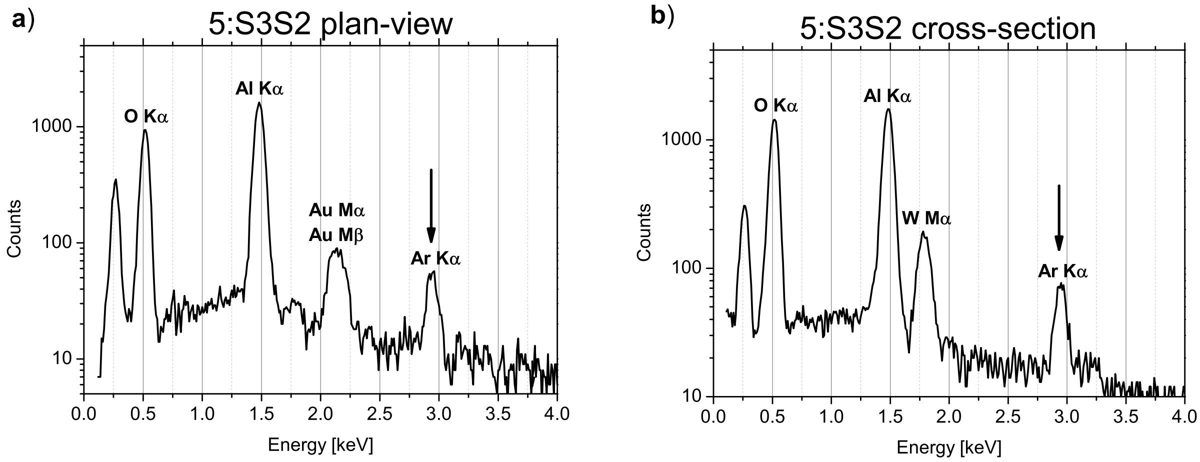

Figure 6.4.: EDX spectra at 10 keV for sample 5:S3S2, acquired in **a)** plan-view and **b)** cross-section configuration. In plan-view, a Au peak emerges due to a sputtered Au Film on top of the film. In cross-section, a tungsten peak is visible in the spectrum due to the WC substrate. The $^{Al}/_{Ar}$ (and peak-to-background ratio) was determined as 16.4 (4.6) for **a)** and 14.5 (4.0) for **b)**

For all samples, 9 to 23 spectra were acquired at multiple positions, spread out across the whole sample surface. Each individual spectrum was quantitatively analyzed with respect to Al-, O- and Ar- mole fractions and the obtained results were averaged to give the chemical composition for each individual sample. Figure 6.4 shows a typical spectrum of the plan-view analysis for sample 5:S2S3 acquired at 10 kV acceleration voltage. An Ar peak at 2.95 keV is visible in the spectrum with a peak-to-background ratio of 4.6. The Au peak originates from a thin, sputtered Au layer on top of the sample.

The results of the plan-view elemental analysis are given in 6.3. Ar mole fractions values are

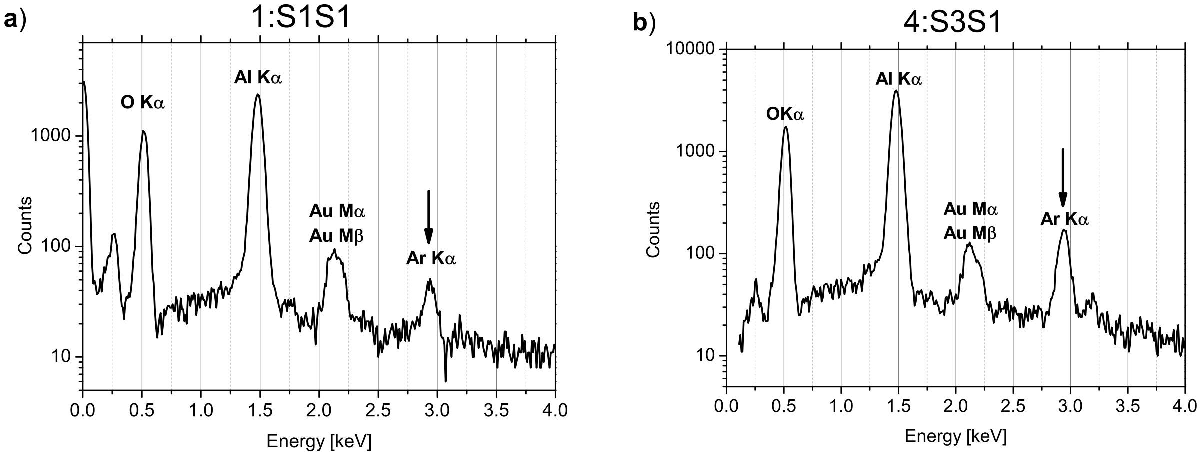

Figure 6.5.: EDX point spectra at 10 keV for **a)** sample 1:S1S1 and **b)** sample 4:S3S1 in plan-view. Sample 1:S1S1 yielded the highest Al to Ar mole fraction ratio. Still a clear peak for Ar at 2.8 keV can be seen with a peak-to-background ratio of 2.9. For sample 4:S3S1, Ar mole fraction ratio was the highest in plan-view analysis, yielding a peak-to-background ratio of 6.8.

ranging from smallest values of 1.03 at% for sample 1:S1S1 to the highest values of 2.26 at% for sample 4:S3S1 respectively. The Al to Ar ratio was determined as well, with values ranging from 36.5 for sample 1:S1S1 to 16.1 for sample 4:S3S1.

Sample ID	Al [at%]	O [at%]	Ar [at%]	Al to Ar ratio
1:S1S1	37.57 ± 1.03	61.40 ± 1.05	1.03 ± 0.07	36.5
2:S1S2	36.63 ± 1.38	61.91 ± 1.37	1.46 ± 0.14	25.1
3:S1S3	33.51 ± 0.61	65.10 ± 0.58	1.38 ± 0.11	24.3
4:S3S1	36.44 ± 0.97	61.29 ± 1.04	2.26 ± 0.16	16.1
5:S3S2	35.19 ± 0.24	62.66 ± 1.25	2.15 ± 0.24	16.4
6:S3S3	35.75 ± 1.52	62.14 ± 1.48	2.11 ± 0.21	16.9
7:S3S4	30.94 ± 0.58	67.21 ± 0.57	1.85 ± 0.12	16.7
8:S4S1	32.50 ± 0.46	66.30 ± 0.56	1.19 ± 0.12	27.3
9:S4S2	32.54 ± 1.31	65.38 ± 1.44	2.07 ± 0.19	15.7

Table 6.3.: Quantitative chemical analysis on all samples of series 1,3 and 4 by SEM EDX spectra acquired in plan-view for Al, O and Ar. The Al to Ar ratio is given as well.

Figure 6.5 shows spectra acquired for sample 4:S3S1 (highest Ar mole fraction in plan-view) and sample 1:S1S1 (lowest Ar mole fraction in plan-view). Even for the smallest Ar mole fraction, a clear Ar peak is visible with a peak-to-background ratio of 2.9, as compared to a peak-to-background ratio of 6.8 for sample 4:S3S1. This shows that even for the smallest detected Ar mole fraction, the peak was clearly above the detection limit of SEM EDX.

EDX spectroscopy in cross-section

Quantitative EDX analysis in SEM was carried out for all samples in cross-section configuration and 10 kV acceleration voltage. The electron beam was positioned in the middle of the aluminum oxide film to maximize the overlap of the excitation volume with the aluminum oxide film. Spectra were recorded at least at three different positions in cross-section with 1 to 3 spectra at every position. The quantitative analysis was performed with respect to Al, O and Ar and the results were averaged for each individual sample.

An example spectrum is shown in Figure 6.4b for sample 5:S3S2. Again, a clear Ar peak is visible with a peak-to-background ratio of 4.0. Due to the thin aluminum oxide film of sample 5:S3S2 (650 nm, see Table 6.1), a small peak from the WC substrate can be seen at 1.8 keV. The results of the quantitative chemical analysis of all samples are given in Table 6.4 for an Al and Ar analysis. Figure 6.6 presents a correlation diagram of the argon mole fraction determined in plan-view and cross-section configuration. The linear correlation shows that by carefully adjusting the acceleration voltage to the film thickness, quantitative analysis of Ar is consistent in plan-view and cross-section. Given the inhomogeneous distribution of Ar across the film thickness (see section 6.3.3) and the complicated Ar signal generation for EDX in the SEM, this result is not trivial but very important for a further interpretation. Figure 6.7 shows the Ar mole fractions plotted against the hardness.

High hardness values are only achieved by high levels of Ar mole fractions above 1.5 at%,

Sample ID	Al [at%]	O [at%]	Ar [at%]	Al to Ar ratio
1:S1S1	29.99 ± 0.56	69.12 ± 0.55	0.89 ± 0.05	33.8
2:S1S2	31.13 ± 0.23	67.78 ± 0.29	1.09 ± 0.15	28.6
3:S1S3	32.49 ± 0.63	66.25 ± 0.58	1.29 ± 0.09	25.6
4:S3S1	29.91 ± 0.25	68.22 ± 0.23	1.87 ± 0.06	16.0
5:S3S2	30.09 ± 0.34	67.83 ± 0.38	2.08 ± 0.11	14.5
6:S3S3	30.05 ± 0.25	67.92 ± 0.30	2.03 ± 0.09	14.8
7:S3S4	28.89 ± 0.08	69.27 ± 0.15	1.84 ± 0.09	15.7
8:S4S1	31.36 ± 0.26	67.24 ± 0.50	1.40 ± 0.28	22.4
9:S4S2	29.28 ± 0.32	68.76 ± 0.44	1.96 ± 0.13	14.9

Table 6.4.: Quantitative chemical analysis with respect to Al, O and Ar by EDX spectra acquired in cross-section at multiple areas.

while all samples with Ar mole fractions below 1.5 at% show significantly less hardness. Excluding samples 2:S1S2 and 3:S1S3 (the two poorest samples with respect to hardness) a linear trend is visible. These two samples show the lowest intensity of the (400) peak close to 45.5° indicating a poor crystallinity (see Figure 6.1). A granular microstructure was identified only

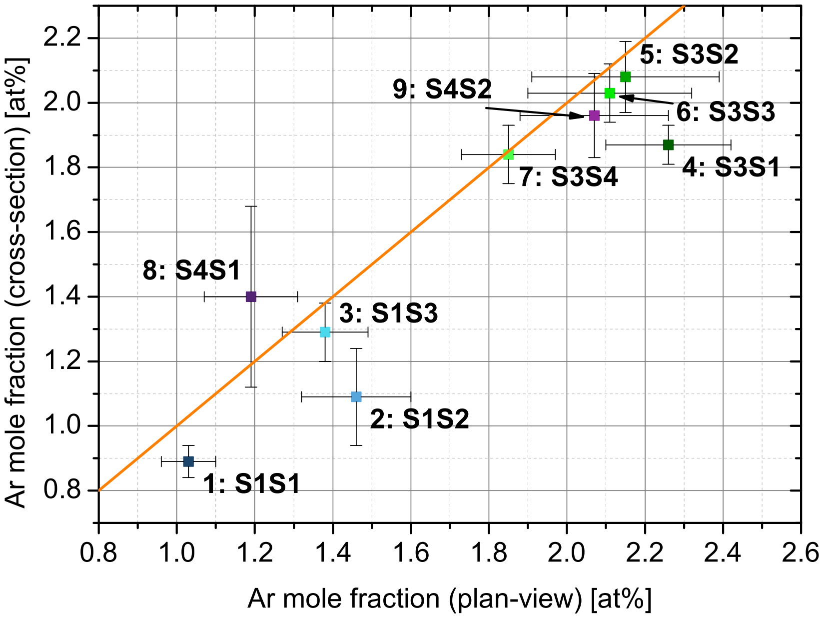

Figure 6.6.: Correlation diagram of Ar mole fraction determined by SEM-EDX in both plan-view and cross-section for all samples of both series. A clear linear correlation can be seen.

for these samples by SEM. For a correlation with hardness, these samples have to be treated separately. This indicates, that if a certain level of crystallinity is visible in the XRD analysis, a higher Ar mole fraction leads to higher hardness values, see also Chapter 6.3.4.

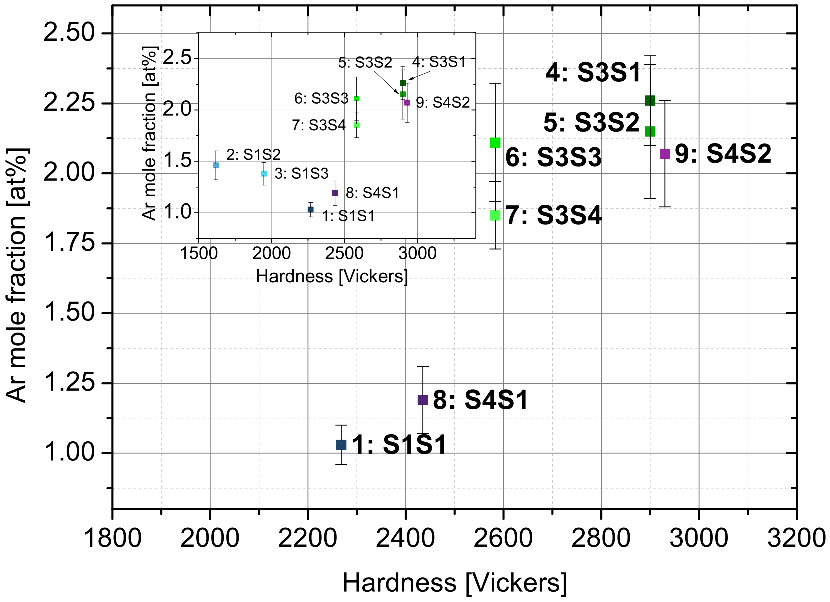

Figure 6.7.: Correlation diagram of the Ar mole fraction with the hardness in Vickers for pseudo-γ aluminum oxide thin films of samples 1 and 4-9. The highest values in hardness are achieved by samples with the highest Ar mole fraction. The inlay shows the corresponding diagram for all samples 1-9.

6.3.3. Chemical analysis by EDX line scans in cross-section

For all cross-section samples, EDX line scans were performed in the SEM at 15kV acceleration voltage. These line scans reveal the elemental distribution across the aluminum oxide films. Multiple spectra at multiple locations were acquired for each sample, the corresponding line scans are given in the Appendix A. For all samples, Al and O distributions follow the dimensions of the structure, giving a gaussian distribution across the center of the film. The Ar content shows a clear deviation in comparison to that of Al and O for all samples.

At the bottom edge (i.e. interface to WC substrate), the Ar content exhibits a similar strong increase, comparable to Al and O distribution. Across the film, the Ar content decreases before the distribution of Al and O drops at the top of the film. The maximum of the Ar distribution was always found at the interface with the WC substrate. For the rest of the film, three typical patterns were identified: i) an almost linear decay up to the top of the film ii) a constant Ar distribution across the rest of the film and iii) a second, smaller peak in the middle of the aluminum oxide film. Such different patterns were found for different samples, but even within one sample.

6.3.4. Structure-property correlation

Due to the intended use of the coated samples as a cutting tool, the investigation and understanding of the mechanical properties is of highest interest.

As described in section 2.2.1, many parameters are available during deposition to optimize the mechanical properties of pseudo-γ aluminum oxide.

But if only mechanical properties are studied, the optimization of the deposition parameters is reduced to trial and error. Therefore, the investigation of structural properties and their correlation to the mechanical properties is of highest importance.

Sample ID	Deposition bias [V]	Young's modulus [GPa]	HV [Vickers]	Plan-view Al to Ar ratio	XRD $2\theta_{400}$[°]
8:S4S1	-90	331	2435	27.3	45.52 ± 0.03
9:S4S2	-125	380	2930	15.7	45.21 ± 0.03

Table 6.5.: Summary of series 4 samples with different deposition bias voltages. Mechanical properties, structural and chemical features are given to highlight the influence of the deposition bias voltage.

During deposition, the applied bias voltage is important in order to achieve the surface energy necessary for the growth process, and thus atomic mobility. The energy is necessary to achieve crystalline structures in a growing layer. Table 6.5 gives an overview of the two samples of series 4, where different bias voltages were applied. Even lower bias values (of -40 V) lead to the formation of amorphous aluminum oxide structures. The optimal deposition bias of -125 V leads to the formation of the sample with the highest hardness value of 2930 Vickers and Youngs modulus of 380 GPa.

This is in agreement with results obtained by Sridharan et al. on γ aluminum oxide, where amorphous structures were seen for a bias voltage of -30 V and crystalline structured emerged starting from bias voltages of -70 V, but higher substrate temperature were needed [61].

In other material systems, the importance of the deposition bias was examined as well, e.g. in TiAlC, where a negative correlation was observed by Pang et al. [94]. In addition, they determined a decrease of the sp3 to sp2 molecular orbital ratio with increasing bias, leading to a crystal structure with decreased mechanical properties. For TiSiN, the highest hardness values were achieved with a deposition bias of -150V [95], similar to the optimal deposition bias of -125 V for pseudo-γ aluminum oxide in this work and -150 V obtained by Engelhart et al. [56].

The influence of the bias voltage on the crystalline structure has to be considered when insulating layers are grown using the PVD process, which applies for example to a large number of metal oxide compounds. During growth, the effectively applied bias potential is reduced with increasing layer thickness, because of the insulating properties of the layer material. Consequently, this worsens the growth conditions at the layer surface and can ultimately lead to exclusively or primarily amorphous structures being grown.

The structural investigation revealed that the sample hardness is directly linked to the incorporation of Ar into the structure, see Figure 6.7. The high deposition bias apparently leads to the beneficial incorporation of argon into the defect spinel structure.

For samples 2:S1S2 and 3:S1S3, quantitative SEM EDX revealed Ar mole fractions of 1.09 to 1.29 at%. However, these samples showed lowest hardness values of 1618 and 1947 Vickers and granular structure in SEM CS images.

The bias potential has to provide the necessary energy to incorporate the argon atoms into the spinel structure. If this is not the case, amorphous regions with high Ar mole fractions are formed, lowering the mechanical properties of the sample. This is also seen for samples of

series 4 in Table 6.5, where the higher deposition bias leads to the formation of the aluminum oxide film exhibiting the highest hardness value of all samples and the incorporation of the highest Ar mole fractions.
Both samples were investigated in the TEM in section 9 for further investigation of the influence of argon incorporation for the mechanical properties.

6.4. Conclusion

The pseudo-γ aluminum oxide phase was introduced in 2011 and is structurally related to a disordered spinel structure. Pseudo-γ aluminum oxide films deposited on WC substrate show high hardness values. Ar introduced by the sputtering gas plays the most important role in the formation of pseudo-γ aluminum oxide films. Ar shows influence on film property (i.e. hardness) by stabilizing the hard phase. X-ray diffractograms yield only a small number of peaks, low in intensity on a large background. However, the (400) peak of pseudo-γ aluminum oxide correlated with the physical properties, i.e. the hardness decreased with (i) increasing angle of the peak and (ii) with the decreasing peak-to-background ratio of the (400) peak.
The bias potential significantly influenced the structure of the films deposited at about 550 °C. High absolute bias voltages (-125 V) yielded crystalline films, low absolute bias deposition (-40 V) yielded amorphous films. The quality of the crystalline films of pseudo-γ with respect to hardness was best for (-125 V). A detailed analysis of the Ar mole fraction and distribution of Ar was carried out here. A detailed measurement procedure was established for determining the Ar mole fraction based on quantitative EDX analyses in plan-view and cross-section. Only by following this procedure a reliable determination of the Ar mole fraction is possible. This in turn is required for establishing a correlation of the Ar mole fraction with the hardness and Young's modulus.

7. Pseudo-γ aluminum oxide thin films: a conductive, optically transparent oxide and methods of contacting

7.1. Introduction

Transparent conductive oxides (TCO) are still an active field of research due to their wide range of possible applications. The combination of optical transparency in conjunction with electrical conductivity makes this class of materials an ideal choice for optoelectronic devices, photovoltaic devices, light emitting diodes or even displays [96, 97, 98, 99].
The most popular transparent conductive oxide is indium tin oxide (ITO) [96, 98], but many other materials have been discovered [35]. Gallium oxides are of great importance for this work, due to their chemical similarity to aluminum oxides (both Al and Ga are in the group 13 of the periodic table).
In the work presented here, the main application of pseudo-γ thin films deposited by PVD are wear resistant coatings. Due to their outstanding structural properties (high hardness, chemical inertness and corrosion resistance [100]) and the easily available components (i.e. no indium or gallium), a transparent conductive aluminum oxide is an ideal candidate for applications of TCOs where durability and cost effectiveness is of great importance.

7.2. Experimental procedure

7.2.1. Sample preparation

For the analysis of the electrical and optical properties of pseudo-γ aluminum oxide in this chapter, samples from series 1,3 and 4 on tungsten carbide substrates were used. More detail is given in Tables 2.1, 2.3 and 2.4 in section 2.2.3. The relevant information and film thickness

Sample ID	Young's modulus [GPa]	HV [Vickers]	Thickness of Al_2O_3 film [µm]	Roughness of Al_2O_3 film [nm]	Granularity
1:S1S1	323	2268	0.76 ± 0.01	78 ± 14	no
2:S1S2	270	1618	1.47 ± 0.03	157 ± 47	≈ 229 nm
3:S1S3	271	1947	1.64 ± 0.10	160 ± 53	≈ 194 nm
4:S3S1	352	2900	1.64 ± 0.09	68 ± 19	no
5:S3S2	352	2900	0.65 ± 0.04	41 ± 8	no
6:S3S3	343	2583	1.28 ± 0.06	74 ± 20	no
7:S3S4	343	2583	0.56 ± 0.02	30 ± 7	no
8:S4S1	331	2435	1.06 ± 0.06	69 ± 30	no
9:S4S2	380	2930	1.04 ± 0.04	75 ± 30	no

Table 7.1.: Aluminum oxide thin films deposited on WC substrates of series 1, 3 and 4. Mechanical properties are given as Young's modulus and Vicker's hardness. The layer thickness, granularity and surface roughness of the films were determined at multiple areas by SEM imaging.

measured in the SEM is given in Table 7.1.

7.2.2. Electrical measurements at RT

To measure the electrical resistance of the pseudo-γ aluminum oxide films, thin Au layers were deposited on top of the aluminum oxide films. The WC substrate itself is conductive and acts as a back contact. The measurement setup is illustrated in Figure7.1a. Top contact to the metalization was established by lowering spring contacts onto the Au metalization. This way, the resistance can be measured between the top and the bottom of the sample (in the following named cross-plane resistance) and between different spring contacts on the sample top (in the following named in-plane resistance). Resistance was determined by measuring the current during a voltage sweep from 0 mV to 20 mV and fit of the slope of the measurement data.

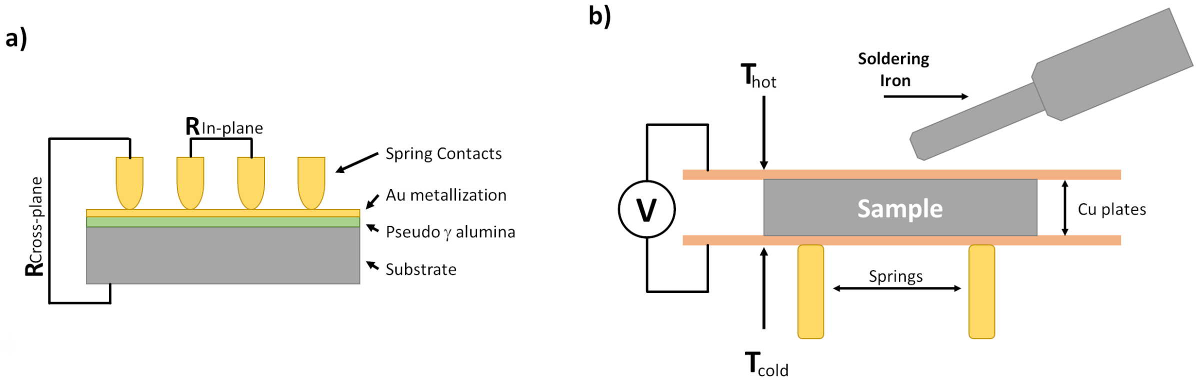

Figure 7.1.: **a)** Experimental setup for resistance measurements. Top contact is realized by four spring contacts to the metalization, bottom contact is achieved by the full coverage of the conductive WC substrate. The resistance can be measured in cross-plane between a single finger and the substrate or in in-plane configuration between two different fingers. **b)** Experimental setup for the thermopower measurement. The sample is sandwiched between two Cu plates that act as contacts for the temperature and voltage measurement.

7.2.3. Electrical measurements in cryostat

Small pieces were cut out of the samples (10 mm x 5 mm x 1 mm) and mounted in an optical cryostat. The cross-plane resistance was measured in a temperature range between 80 K and room temperature (RT) by the same technique as for the room temperature measurement.

7.2.4. Electrical measurements: thermopower

The setup for the thermopower measurement is shown in Figure 7.1b. The sample is placed between two Cu-plates and kept in place by springs. Two thermocouples are attached to the Cu-plates (one to the top and one to the bottom plate) to measure the temperature difference across the film with high precision. Using a sourcemeter and the Cu-plates as contacts, the voltage generated by the sample can be measured simultaneously. To heat up the top Cu-plate, a soldering iron is used.

7.3. Results

7.3.1. Structural and optical properties

Detailed structural analysis of the samples are summarized in chapter 6. It was found that the deposited films were pseudo-γ aluminum oxide, which show crystalline spots as well as an amorphous background in electron diffraction. A significant amount of argon (up to 2.26 at%) was found in the films, originating from the sputtering process, and a correlation to its structure was established. Important for the understanding of the electrical measurement results are the structural differences between samples with high and low hardness values. In SEM imaging, films yielding low hardness (i.e. samples 2:S1S2 and samples 3:S1S3) exhibit a granular structure, perpendicular to the film (i.e. parallel to the growth direction) with a granular size of approximately 200 nm. Films yielding large hardness on the other hand showed a homogeneous film that appears dense and monolithic rather than a granular microstructure. An SEM image of samples 2:S1S2 and 3:S1S3 is shown in Figure 7.2.

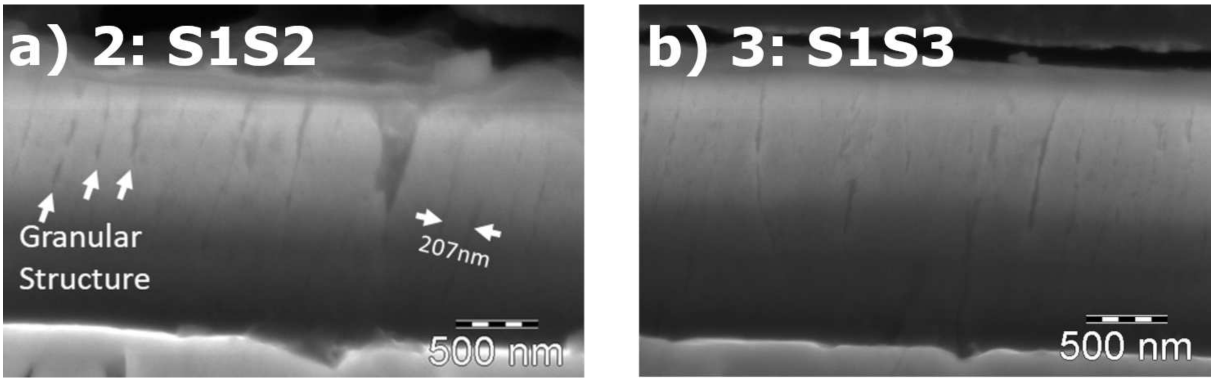

Figure 7.2.: SEM cross-section analysis of **a)** sample 2:S1S2 and **b)** sample 3:S1S3. Sample 2:S1S2 (3:S1S3) shows a granular structure with an average granular size of $\approx$ 229nm (194nm)

To investigate the optical properties of the pseudo-γ aluminum oxide thin films, small pieces were analyzed using transmission light microscopy (see Figure 7.3). The pseudo-γ aluminum oxide film surface was covered using a black marker. The sample was mounted as shown in Figure 7.3a, i.e. the films were aligned in parallel to the illumination from below. By bringing the microscope out of focus, the thin films were visible as a bright blue line. Since the film was covered by the opaque marker, the light had to travel through the thin pseudo-γ aluminum oxide layer. With this, it is clearly shown that the pseudo-γ aluminum oxide films are optically transparent.

For samples 5:S3S2 and 7:S3S4, spectroscopic ellipsometry measurements were conducted. Polarized light is directed to the sample surface and the amplitude ratio (Ψ) and phase shift (δ) of parallel and perpendicular polarization to the sample surface is recorded. The two samples were chosen because of their thin aluminum oxide films (less than 650 nm) to avoid strong interference effects during the measurement.The incident beam angle was set to 75°, the wavelength range was set to 400 nm and 900 nm to cover the optical part of the spectrum.

A pure piece of WC substrate was characterized as well. For a measurement with only one interface (i.e. air to WC substrate), the dielectric function can be extracted directly from the

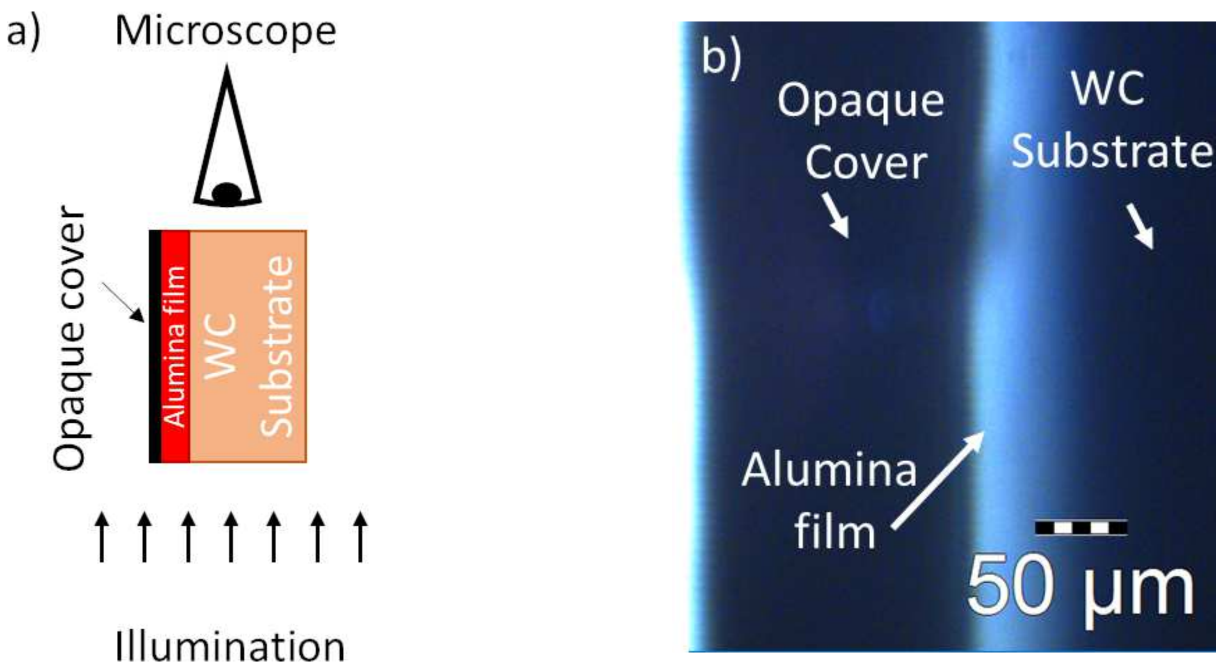

Figure 7.3.: **a)** Sketch of the transparency check for the pseudo-γ aluminum oxide samples. Samples are illuminated in parallel to the film structure, thus guiding the light through the aluminum oxide film. **b)** Lightmicroscopic image of sample 4:S3S1 in cross-section. On the left side, the opaque cover is visible, on the right the non-transparent substrate. The film is clearly visible by a bright line in between.

measurement for every wavelength. To determine the dielectric function of the pseudo-γ aluminum oxide film, a simple model was set up consisting of the reference substrate covered by the aluminum oxide film. Film roughness was taken into account by a thin effective medium layer according to Bruggemann [101]. Film thickness was set to the values determined in SEM,

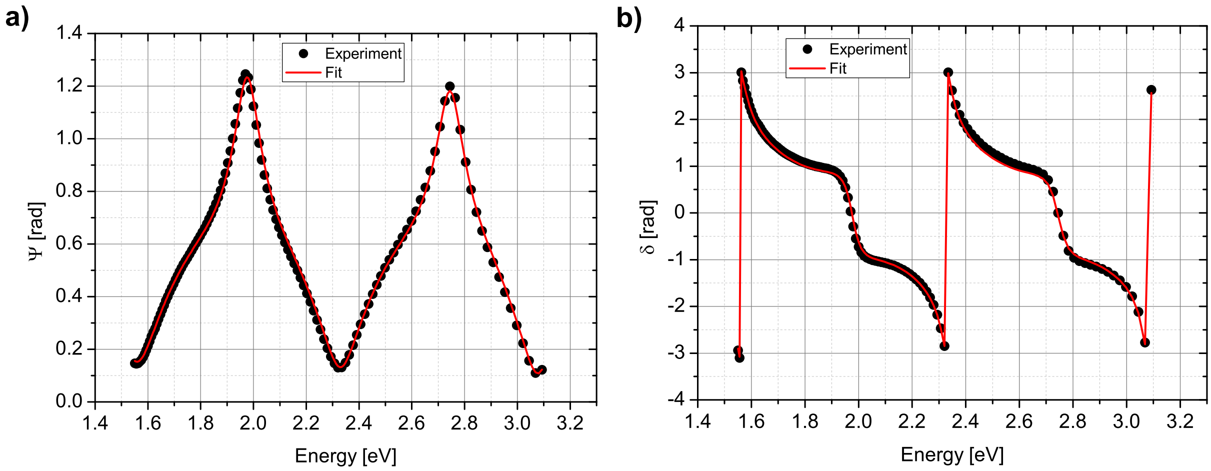

Figure 7.4.: Experimental data points for **a)** the amplitude ratio Ψ and **b)** phase shift δ of sample 7:S3S4. Only every second data point (with respect to the energy) is shown. The fit is plotted as a red line and shows good agreement with the experimental results.

see Table 7.1. For transparent materials, Cauchy dispersion model with Urbach absorption is mostly used in literature [102, 103] and was also successfully applied to transparent conductive oxides [104, 105, 106]. In the Cauchy- Urbach model, three parameter A,B and C are available for describing the real part of the refractive index

$$n = A + \frac{B}{\lambda^2} + \frac{C}{\lambda^4} \tag{7.1}$$

and three parameter α, β and γ for the complex part

$$k = \alpha\, exp\left(\beta\left(\frac{hc}{\lambda} - \gamma\right)\right). \tag{7.2}$$

Sample ID	A	B [µm^2]	C [µm^4]	α	β [eV^{-1}]	γ [eV]	n @550 nm	k @550 nm
5:S3S2	1.697	0.0054	-0.00005	0.0073	0.0002	4.1523	1.697	0.007
7:S3S4	1.674	0.0041	0.00002	0.0089	0.0179	4.1199	1.674	0.009

Table 7.2.: Fit parameter for the cauchy Model (A, B and C) with Urbach absorption (α, β and γ) for samples 5:S3S2 and 7:S3S4. The complex refractive index ($n - ik$) is calculated for a wavelength of 550 nm.

Figure 7.4 shows the measurement parameters Ψ and δ in combination with the model fit for sample 7:S3S4. It shows good agreement for both parameters. Table 7.2 gives the fit parameters for the Cauchy-Urbach model for both samples, as well as the complex refractive index for the pseudo-γ aluminum oxide film at 550 nm. Absorption is linked to the complex part k of the refractive index and is small for both samples, proving that the films are in fact transparent in the optical range.

7.3.2. Full area metalization of the films

Metalization of the pseudo-γ aluminum oxide thin films on WC substrates was essential for electrical measurements. Pseudo-γ aluminum oxide films were dense and had a flat surface with a small surface roughness of 30-160 nm (see Table 7.1). Direct contacting on the bare surface in absence of a designated deposited electrical contact did not yield reliable results. Either the measured resistance was not reproducible or the resistance was out of range (>20 MΩ). Therefore, contacts were deposited by DC sputtering using a gold target in a standard DC sputtering machine for gold layer deposition for scanning electron microscopic investigations. The sputtering gas was Ar (pressure 0.07 mbar). The deposition rate can be controlled by the pressure in the sputtering chamber.

The thickness of the deposited gold film was controlled by the duration of the sputtering process. Plan-view SEM EDX analysis was performed on sputtered samples and the peak ratio of Au and Al peaks was determined. In addition, EDX spectra were simulated using Monte Carlo methods in the DTSA II software package [107] for Au layers of different thickness. In Figure 7.5d, a measured spectrum for a sample with 40 s sputtering duration is shown in combination with the simulated spectra with 40 nm thick Au layer. The simulated spectrum was normalized with respect to the Al peak to match the experimentally determined spectrum since only the peak ratios are of interest.

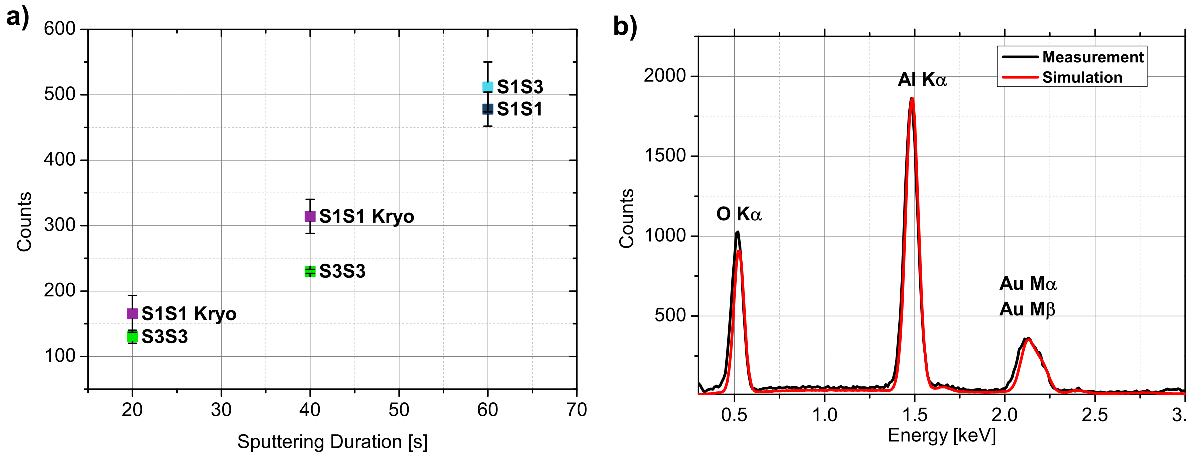

Figure 7.5.: **a)** EDX counts of Au peak (Au layer thickness) versus the duration of the Au sputtering process for different samples of series 1 and 3. **b)** Comparison of a recorded SEM EDX spectrum for a sample with sputtered Au (for 40 s) to a simulated spectra with a 40 nm thick Au layer. The simulated spectrum is normalized to match the Al peak of the experimentally measured spectrum.

By comparing the experimentally determined ratios of the Al-Peak vs Au-Peak (for samples with known sputtering duration) to the ratios in the simulated spectra (with known Au layer thickness), it was possible to determine a deposition rate of 1 nm Au layer thickness to 1 s sputtering duration (Figure 7.5c).

The gold films showed good adherence to the aluminum oxide films and passed a scotch tape test. Different thicknesses were adjusted and the electrical resistance was measured. It was found that a thickness of 40 nm was optimal for achieving reproducible results and a saturation in the measured resistance was detected (more details in the Appendix C). Electrical resistance of the so contacted pseudo-γ aluminum oxide films ranged from 8 Ω to 122 Ω (Table 7.3) at room temperature. 8 Ω were measured for high-quality films with high hardness and no granularity visible whereas up to 122 Ω were measured for granular films. The reproducibility of these measurements was high and local variations of the resistivity were limited (50 % for 7:S3S4).

7.3.3. Resistivity between 80 K and room temperature

The resistance values measured in cross-plane of the fully metalized samples at room temperature are given in Table 7.3. With a 40 nm Au metalization, sample 1:S1S1 and samples 4:S3S1 to 7:S3S4 showed low ohmic resistance values from 7.8 Ω to 11.9 Ω. Samples 2:S1S2 and 3:S1S3 showed higher resistance values of 45.4 Ω (sample 2:S1S2) and 122 Ω (sample 3:S1S3) respectively. These two samples are also outstanding with respect to their structural properties (see Table 7.1), i.e. their low hardness values and the observed granularity in the pseudo-γ aluminum oxide films.

Sample ID	Thickness of Al_2O_3 film [µm]	Granularity	Nominal thickness of Au layer [nm]	Resistance at RT [Ω]	In-plane to cross-plane
1:S1S1	0.76 ± 0.01	no	40	11.9 ± 2.4	0.82 ± 0.08
2:S1S2	1.47 ± 0.03	≈ 229 nm	40	45.4 ± 7.8	0.69 ± 0.08
3:S1S3	1.64 ± 0.10	≈ 194 nm	40	122 ± 64	0.97 ± 0.07
4:S3S1	1.64 ± 0.09	no	40	10.1 ± 2.2	0.86 ± 0.06
5:S3S2	0.65 ± 0.04	no	40	7.8 ± 1.6	0.92 ± 0.04
6:S3S3	1.28 ± 0.06	no	40	11.6 ± 1.9	0.86 ± 0.06
7:S3S4	0.56 ± 0.02	no	40	9.0 ± 1.2	0.93 ± 0.06
8:S4S1	1.06 ± 0.06	no	40	8.4 ± 1.0	0.51 ± 0.06
9:S4S2	1.04 ± 0.04	no	40	11.5 ± 3.1	0.59 ± 0.17

Table 7.3.: Room temperature resistance obtained for samples 1 to 7, contacted by a full area Au electrode with a nominal thickness of 40 nm. The thickness of the pseudo-γ aluminum oxide film and the granularity of the film were obtained by cross-section SEM imaging.

All samples were measured in cross-plane and in in-plane (see Figure 7.1). In Figure 7.6b, possible current paths are given for the in-plane measurement:

- Current path **a** is dominating in case of a thick metalization. The in-plane resistance is expected to be lower than the cross-plane resistance.
- **b)** describes current flow through the aluminum oxide film.
- **c)** The current flow crosses the pseudo-γ film twice. Therefore, the in-plane resistance is twice the cross-plane resistance.

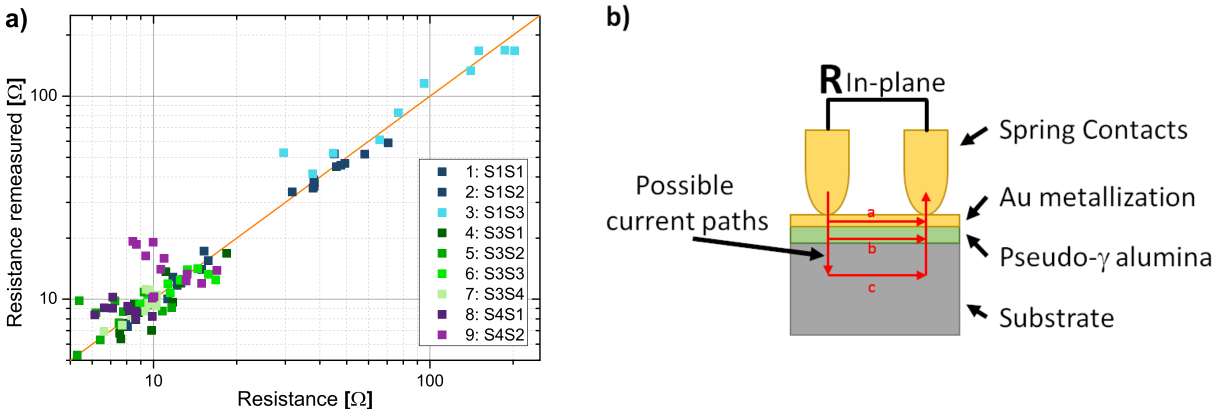

Figure 7.6.: **a)** Reproducibility for the resistance measurements is checked by measuring the resistance at multiple locations on the sample (x-axis) and remeasured at the same position after remounting the sample (y-axis). An orange line indicates a perfect one to one match. **b)** Possible current paths for the in-plane resistance measurements.

Resistance measurements of pure WC substrate pieces yielded low ohmic resistance values (less than 0.1 Ω), the resistivity of pseudo-γ is therefore expected to be higher in comparison to that

of WC. As a consequence, current path **b** can be ruled out.
To determine the dominating current path (**a** or **c**), it is helpful to calculate the ratio of the in-plane resistance to twice the cross-plane resistance. For current path **a**, this ratio tends towards zero and only for current path **c** towards one. This ratio is also given in Table 7.3.
For sample 2:S1S2, this ratio yields a value of 0.69 and values between 0.82 - 0.93 for samples 1 and 3 to 7, indicating that current path (c) is dominating.

To prove reproducibility of the electrical measurements, every sample was measured in a systematic way at different positions of the sample surface. After removing and remounting the sample, the resistance was measured again at the same positions. Figure 7.6a shows the re-measured resistance of each position plotted against the resistance of the first measurement. It shows clearly how the second measurement reproduces the resistance of the first measurement. To measure the temperature dependence of the electrical resistance, a small piece (10 mm x 5 mm x 1 mm) was cut out of sample 1:S1S1 and mounted in an optical cryostat. To improve the setup quality and remove parasitic resistances (i.e. wire resistances), a 4-wire setup was established. The resistance was measured at different temperatures starting from 80 K to 300 K.

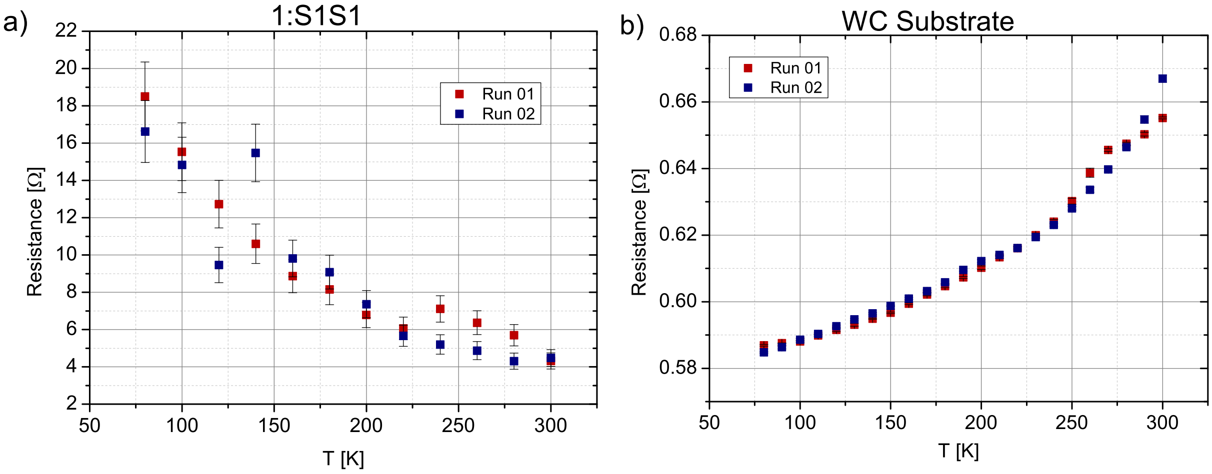

Figure 7.7.: **a)** Cross-plane resistance of Sample 1:S1S1 from 80 K to 300 K. The resistance increases exponentially with decreasing temperature. **b)** Temperature-dependent resistance of a pure WC substrate piece.

The results are shown in Figure 7.7a. Both measurement runs show a clear increase in the resistance with decreasing temperature as is typical for a semiconductor. At 80 K, the resistance is increased by a factor of 4 in comparison to the resistance at 300 K. In addition, Figure 7.7b shows the temperature dependence of a pure WC substrate piece, which exhibits metallic behavior (i.e. decreasing resistance with decreasing temperature). This shows once again that the current is in fact passing through the pseudo-γ aluminum oxide phase.

7.3.4. Thermopower measurements at room temperature

Thermopower of pure WC substrate

To measure the thermopower of the pseudo-γ aluminum oxide films, the conductive WC substrate needs to be taken into account. Since the temperature difference is applied across the whole sample (i.e. substrate and the film), a part of the voltage signal will be generated by the substrate alone. Consequently, extra care has to be taken.
The thermopower for a pure WC substrate was determined in order to infer the thermopower contribution attributed to the pseudo-γ phase. Using a soldering iron, the top Cu-plate was heated up to a temperature difference of 15 K and the following cooling was recorded, showing linear behavior of the voltage with respect to the temperature difference.
The Seebeck coefficient of the substrate was determined using $S = -\frac{V}{\delta T} = -14.7\frac{\mu V}{K}$. The raw data of the thermopower measurement is shown in Figure 7.8, where the ratio of the measured voltage to the temperature difference across the sample is given.

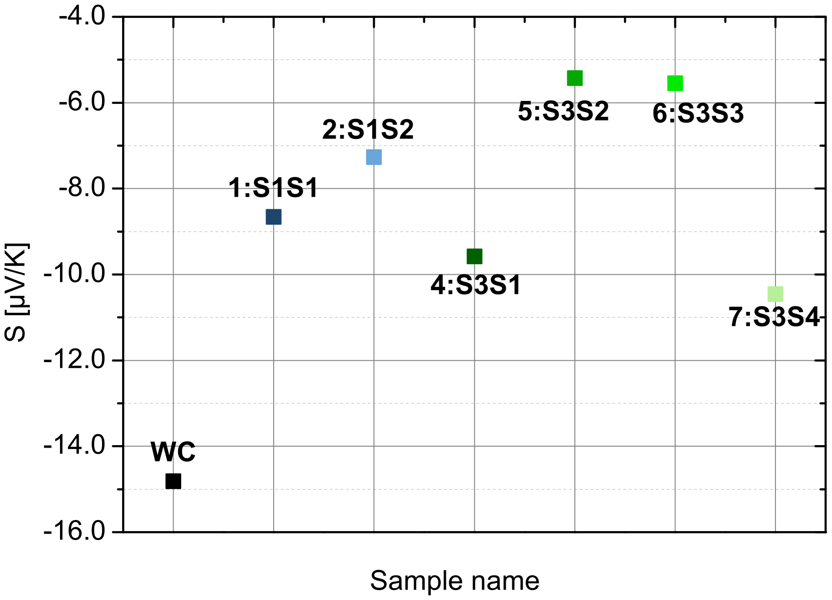

Figure 7.8.: Raw Data for thermopower measurement without any correction according to equation 7.6. Please note that the x-axis carries no information other than the sample name.

Thermopower of pseudo-γ aluminum oxide films on WC substrate

The generated electromotive force of the full sample is made up of contributions of the WC substrate and the pseudo-γ aluminum oxide film. The overall voltage signal across the sample is therefore

$$V_{Total} = V_{Al_2O_3} + V_{WC}. \tag{7.3}$$

In the steady state case, the generated voltage signal can easily be linked to the temperature difference across the corresponding film

$$V_i = S_i \, \Delta T_i \tag{7.4}$$

(where *S* is the thermopower). In the steady state the heat flux at the interface of the film and the substrate has to be conserved

$$\lambda_{Al_2O_3} \, \nabla T_{Al_2O_3} = \lambda_{WC} \, \nabla T_{WC} \tag{7.5}$$

Where λ is the thermal conductivity.
As a result, the thermopower of the pseudo-γ aluminum oxide film can be expressed as

$$S_{Al_2O_3} \approx \frac{\lambda_{Al_2O_3}}{\lambda_{WC}} \frac{d_{WC}}{d_{Al_2O_3}} \cdot \left(-\frac{V_{Total}}{\Delta T} - S_{WC} \right), \tag{7.6}$$

where *d* is the thickness of the layers. A more detailed derivation for equation 7.6 is given in the Appendix D.
The voltage and temperature differences were measured directly. Using a high precision spring platform, the substrate thickness was determined. For the pseudo-γ aluminum oxide film, thickness values were measured in the SEM (see Table 7.1). Since the Seebeck coefficient of WC was previously determined, only its thermal conductivity was taken from literature as 110 $\frac{\text{W}}{\text{m K}}$ [108].
Using equation 7.6, it is possible to determine the ratio of the Seebeck coefficient to the thermal conductivity of pseudo-γ aluminum oxide. The results for samples 1 and 2 of series 1 and all of series 3 are given in Table 7.4.

Sample ID	1:S1S1	2:S1S2	4:S3S1	5:S3S2	6:S3S3	7:S3S4
$\frac{S_{Al_2O_3}}{\lambda_{Al_2O_3}}$ $[\frac{\mu\text{V/K}}{\text{W/(m K)}}]$	59 ± 4	46.2 ± 0.2	30 ± 1	111 ± 3	42.6 ± 0.7	86 ± 4

Table 7.4.: Ratio of the thermopower and the thermal conductivity of the pseudo-γ aluminum oxide film for samples 1:S1S2 and 2:S1S2 of series 1 and all samples of series 3. The ratio's unit can be reduced to $\frac{\mu\text{m}}{\text{A}}$.

7.4. Discussion

7.4.1. Metalization

For the application of pseudo-γ aluminum oxide as an conductive oxide, contacting and hence metalization of the film plays an important role. Large area Au contacts deposited by DC sputtering exhibit reproducible results in terms of electrical resistance, but small area contacts did not.
Metalization is still an important task (see also 8). Poor adhesion between Au (in our case for small area contacts) and oxide substrates is a well-known problem [109, 110]. Zhang et al. did

a detailed investigation on the mechanism of sputtered Au on TiO layers [111]. More research in the future is necessary to improve the small area metalization to enable measurements of the specific resistance.

7.4.2. Transport and optical properties

Electrical resistance

Typically, aluminum oxide phases are known to be electrically insulating [112, 113]. In the literature, there are multiple measurements and simulations of the electrical band gap for different aluminum oxide phases. For α aluminum oxide, a high band gap value of 8.7 eV to 8.8 eV is given based on simulations [21, 114] and photoemission experiments [115]. Filatova et al. performed x-ray photoelectron spectroscopy measurements and report a band gap value of 7.0 eV for amorphous and 7.6 eV for γ aluminum oxide respectively [20].
The results obtained here show on multiple samples of pseudo-γ aluminum oxide that this phase is in fact an electrical conductor. Using DC sputtered large area Au contacts, low ohmic resistance values were achieved, see Table 7.3. The structural differences of pseudo- to standard-γ aluminum oxide, especially the Ar content, might play the key role in the formation of the electrical conduction mechanism, but further work is needed to determine the exact process. The temperature dependence clearly shows semiconducting behavior of the pseudo-γ aluminum oxide phase.

Thermopower

The conductive WC substrate limited the direct measurement of the thermopower of pseudo-γ aluminum oxide to the determination of the ratio of the thermopower to the heat conductivity. Su et al. report a value of $6\,\frac{\mathrm{W}}{\mathrm{m\,K}}$ for the heat conductivity of standard-γ aluminum oxide [45]. Based on this value, it is possible to estimate the absolute thermopower of pseudo-γ aluminum oxide to be in the range from $180\,\frac{\mu\mathrm{V}}{\mathrm{K}}$ to $666\,\frac{\mu\mathrm{V}}{\mathrm{K}}$.
These results are outstanding in terms of their absolute values and the positive sign in comparison to other transparent conductive oxides. Orita et al. report on thermopower measurements of $\mathrm{InGaO_3(ZnO)}_n$ yielding $-53\,\frac{\mu\mathrm{V}}{\mathrm{K}}$ to $-66\,\frac{\mu\mathrm{V}}{\mathrm{K}}$ [116]. On $\mathrm{Ga_2O_3}$ - $\mathrm{In_2O_3}$ - $\mathrm{SnO_2}$, Edward et al. achieved values between $-75\,\frac{\mu\mathrm{V}}{\mathrm{K}}$ and $-175\,\frac{\mu\mathrm{V}}{\mathrm{K}}$ [117]. Other groups also report negative thermopower for different TCOs [118, 119].
Kawazoe et al. report a positive thermopower of $183\,\frac{\mu\mathrm{V}}{\mathrm{K}}$ for $\mathrm{CuAlO_2}$, which is explained by an excess of oxygen [120]. In NiO thin films, it is even possible to change the sign of the thermopower (from $-30\,\frac{\mu\mathrm{V}}{\mathrm{K}}$ to $60\,\frac{\mu\mathrm{V}}{\mathrm{K}}$) by different post deposition annealing steps [30, 93]. Future work on pseudo-γ aluminum oxide films deposited on a non-conductive substrate will be necessary to determine the absolute thermopower of these films.

Optical transparency

The pseudo-γ aluminum oxide oxide films investigated in this work have proven to be optically transparent by spectroscopic ellipsometry measurements. Houska et al. give an overview of the refractive index as well as the extinction coefficients for α, γ and amorphous aluminum oxide phases for different deposition methods at a wavelength of 550 nm [103]. All structures show low values for the extinction coefficient, for their γ aluminum oxide sample they report a small extinction coefficient of k_{550nm} $=4 \times 10^{-4}$, close to the values determined for pseudo-γ aluminum oxide given in Table 7.2.

Khanna et al. also present experimental proof of the optical transparency of γ aluminum oxide for a wavelength range of 250 nm to 900 nm [54]. It is noteworthy that they show XRD diffractograms of their samples, where the dominating peaks are in fact the (400) and (440) peaks, while the (222) peak of standard-γ aluminum oxide is missing. It might very well be that their structure was much closer to pseudo-γ aluminum oxide than standard-γ aluminum oxide.

7.4.3. Structure-property correlation

No obvious correlation was found between the electrical properties determined in this work and the structural properties of the samples, see Figure 7.9a. Samples 2:S1S2 and 3:S1S3 show the highest resistance, as well as the highest fluctuation in the measured resistance. Only for these two samples a granular structure was observed in SEM, as well as a high surface roughness, see Table 7.1. This indicates that a part of the measured resistance is made up of the metalization itself and its contact resistance to the aluminum oxide film. The high surface roughness might inhibit a planar coverage of the aluminum oxide film with the sputtered Au, resulting in a higher electrical resistance. Samples 4:S3S1 and 5:S3S2 (6:S3S3 and 7:S3S4 respectively) were deposited in the same batch and were also contacted in the same DC sputtering cycle. Therefore, for these four samples it is justified to assume similar contact quality of the metalization. Sample 5:S3S2 is of the same batch as sample 4:S3S1, but with a smaller layer thickness due to an additional superimposed rotation during deposition (the same is true for samples 6:S3S3 and 7:S3S4 respectively). Therefore it is expected that the thinner aluminum oxide films will result in a lower resistance according to Ohm's law.

However, the change in the resistance does not match the change in the layer thickness in a linear way.

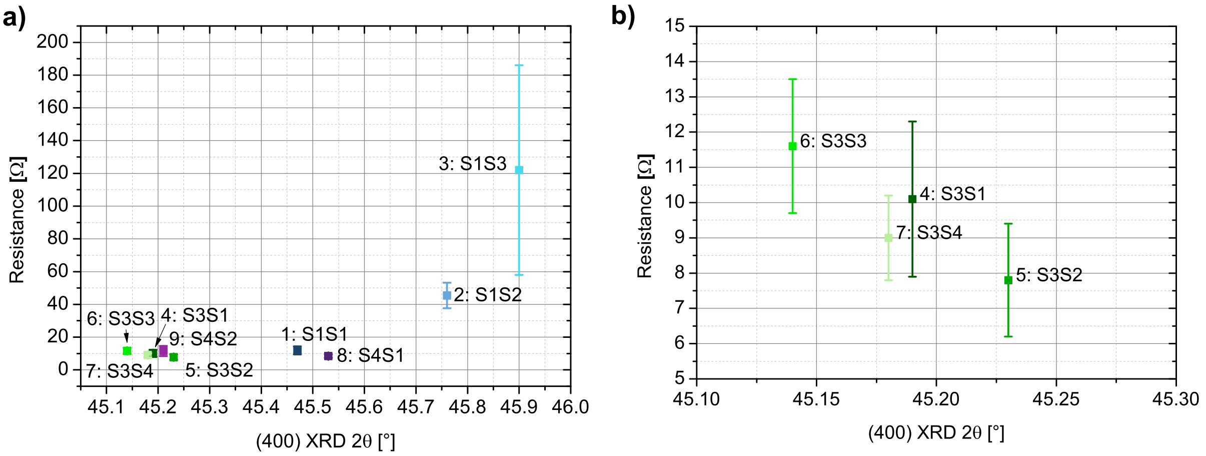

Figure 7.9.: a) Resistance of the fully covered samples are plotted against the 2θ angle of the (400) peak in XRD. **b)** Close-up to the samples of series 3.

To explain this discrepancy, it is necessary to take the structural results into account. For all samples of series 3, a shift in the (400) peak position was detected in XRD measurements. Therefore, the change in resistance cannot be solely attributed to geometric differences, but rather stems partly from a different crystal structure (lattice parameters) as seen in the shift of the XRD peak, see Figure 7.9.

This indicates that there might be an underlying structure-property correlation between the electrical properties and the crystal structure of the pseudo-γ aluminum oxide films, that is revealed if a reliable structured metalization process can be established.

7.5. Conclusion

Pseudo-γ aluminum oxide was introduced in 2011 and is related to the disordered spinel structure of γ aluminum oxide, while showing distinct features. It was found that Ar, introduced during the deposition process, plays the most important role in the formation of the pseudo-γ aluminum oxide phase. In addition to the outstanding structural properties, it was shown here that pseudo-γ aluminum oxide is in fact a transparent conductive oxide.

Spectroscopic ellipsometry measurements showed that the pseudo-γ aluminum oxide films are transparent in the visible range. Electrical resistance measurements at room temperature on fully metalized samples showed low resistance values about $10\,\Omega$. The metalization of the pseudo-γ was achieved in a reproducible manner for large area contacts. However, further work is still needed to improve the contacting process to investigate the electrical properties in a more advanced manner using structured contacts.

The ratio of the thermopower to the heat conductivity were measured and indicate that the pseudo-γ aluminum oxide films have high, positive thermopower values, while still showing low electrical resistance values. In conclusion, the pseudo-γ aluminum oxide films are an interesting candidate for future research on transparent conductive oxides, due to their outstanding structural properties and no expensive materials such as indium or gallium are contained in the structure.

8. Temperature dependent structure-property correlation of pseudo-γ aluminum oxide thin films

8.1. Introduction

Cemented tungsten carbide (WC) is a widely used material for cutting tools, making up more than 50 % of the billion dollar market for cutting tools in 2013 [121]. WC shows outstanding mechanical properties such as high hardness values up to 2250 Vickers [122] and friction toughness [123, 124]. An overview over different consolidation processes and their impact on sample properties can be found in [125].
When exposed to high temperatures, tungsten carbide oxidizes [126, 127], which has a negative impact on the mechanical properties [128]. Due to their use as cutting tools, depending on the cutting speed, high temperatures up to 1200 °C can be reached due to friction [129, 130].
To avoid oxidation, WC tools can be covered with a protective layer, for instance by deposition of multilayer structures of aluminum oxide (Al_2O_3) and TiAlN. The use of single nitride layers is possible [131], but multilayer structures of nitride, carbide or oxide layers are more common due to the combination of their individual advantages (e.g. in terms of hardness or chemical resistance) [65, 66, 131, 132, 133, 134].

Nitride layers alone can reach extraordinary mechanical properties (hardness up to 4000 Vickers [135]). In multilayer structures, they also serve as an adhesive layer for oxide layers and improve the crystal quality of the coating layers [134].
Aluminum oxide layers show low thermal conductivity (13 $\frac{\mathrm{W}}{\mathrm{m\,K}}$ at 760 K for α aluminum oxide [136], 6 $\frac{\mathrm{W}}{\mathrm{m\,K}}$ over a wide temperature range for γ aluminum oxide). Therefore, such layers are especially suitable to prohibit the transformation of the WC substrates into a powdery phase. In addition, aluminum oxide layers also provide a high chemical resistance and remarkable mechanical properties [46].
Using dual magnetron sputtering (DMS) with Ar as a sputtering gas, pseudo-γ thin films were produced and characterized in 2011, showing hardness values up to 2348 Vickers [56].
The first electrical characterization was performed on samples that featured DC sputtered Au contacts, showing small contact resistances but adhesion to the oxide layer needs to be improved, which is a common problem in contacting oxides of any kind [109, 110, 111].
In this work, pseudo-γ aluminum oxide was deposited on WC substrates with an additional TiAlN layer on top. As explained before, such multilayer structures are common to enhance the mechanical properties of cutting tools. In this case, the TiAlN layer served as a low ohmic resistance contacting layer to the aluminum oxide [137]. Due to their thin layer structures (typically in the nm to µm range, [134, 138]), structural analysis is very demanding on multilayer systems.
The correlation of structural information (e.g. standard x-ray diffraction and scanning electron microscopy) with results of electrical measurements (especially temperature dependent resistance measurements) proves to be a powerful tool to analyze thin multilayer structures.

8.2. Experimental procedure

8.2.1. Sample preparation

Table 8.1 gives an overview over all samples under investigation in this chapter. More detailed information about samples from series 1 and 2 are given in Tables 2.3, 2.3 and 2.2 in section 2.2.3.

TiAlN layers were deposited using high power impulse magnetron sputtering (HIPIMS) on top of a pseudo-γ aluminum oxide layer [67]. Sample 14:TiAlN consists of a single TiAlN layer deposited on a WC substrate which served as a reference.

Series	Sample ID	Batch	Thickness of Al_2O_3 film [nm]	Thickness of TiAlN film [nm]
1	1:S1S1	1	760 ± 10	-
2	10:S2S1	8	1762 ± 39	521 ± 39
2	11:S2S2	8	885 ± 31	294 ± 21
2	12:S2S3	9	658 ± 77	431 ± 51
2	13:S2S4	9	365 ± 5	260 ± 10
X	14:TiAlN	10	-	445 ± 27

Table 8.1.: Sample IDs and layer thickness for pseudo-γ aluminum oxide and TiAlN layers. The film thickness was determined in SEM.

8.2.2. Temperature dependent electrical measurements

Room temperature measurements of the electrical resistance were performed with spring contacts for the top side contact, see also section 7.2.2. No extra steps were needed to achieve good electrical contact to the thin films. The resistance was calculated from a linear fit of the acquired current readings to a voltage sweep from $-10\,\mathrm{mV}$ to $10\,\mathrm{mV}$. In this range, the samples always showed ohmic, i.e. linear behavior.

For temperature dependent measurements, small parts (10 mm x 5 mm) were cut out of the sample. To reduce the thermal mass, the substrate thickness was reduced to a few mm. Small samples were mounted in an optical cryostat and the films were contacted using a spring contact platform. The same voltage sweep was performed for cryostat measurements as for the room temperature measurements.

Using liquid nitrogen and a small resistive heater, the resistance was measured over a temperature range starting from 80 K to room temperature.

8.2.3. X-ray diffraction acquisition

X-ray diffractograms were acquired in grazing incidence using the Cu-K_α-Line. For more details of the experimental setup, see also section 6.2.2. Due to the thin layer structures (in the µm range), most of the generated signal originates from the WC substrate. By using grazing incidence geometry (incident angle kept constant at $\Omega = 1°$), the intensity of the peaks attributed to the film is maximized. In addition, the γ aluminum oxide (400) peak is overlapping with the (200) TiAlN and (101) WC substrate peak. Therefore, special care has to be taken during diffractogram analysis. By carefully performing a peak deconvolution and a combined fit of all peaks with a nonlinear background subtraction it was possible to identify and analyze the (400) pseudo-γ aluminum oxide peak in all spectra.

8.3. Results and discussion

8.3.1. Structural analysis in XRD and SEM

X-Ray diffractograms were acquired for all samples of series 2 and are shown in Figure 8.1a in the range $2\theta = 35°$ to $50°$. For all four samples, the diffractogram is dominated by two peaks originating from the WC substrate at $2\theta = 35.6°$ (WC (100)) and $2\theta = 48.4°$ (WC (101)). Besides the substrate peaks, only broad peaks with small intensities can be attributed to the aluminum oxide and TiAlN films. Two peaks at $2\theta = 37.7°$ and $2\theta = 43.4°$ can be attributed to

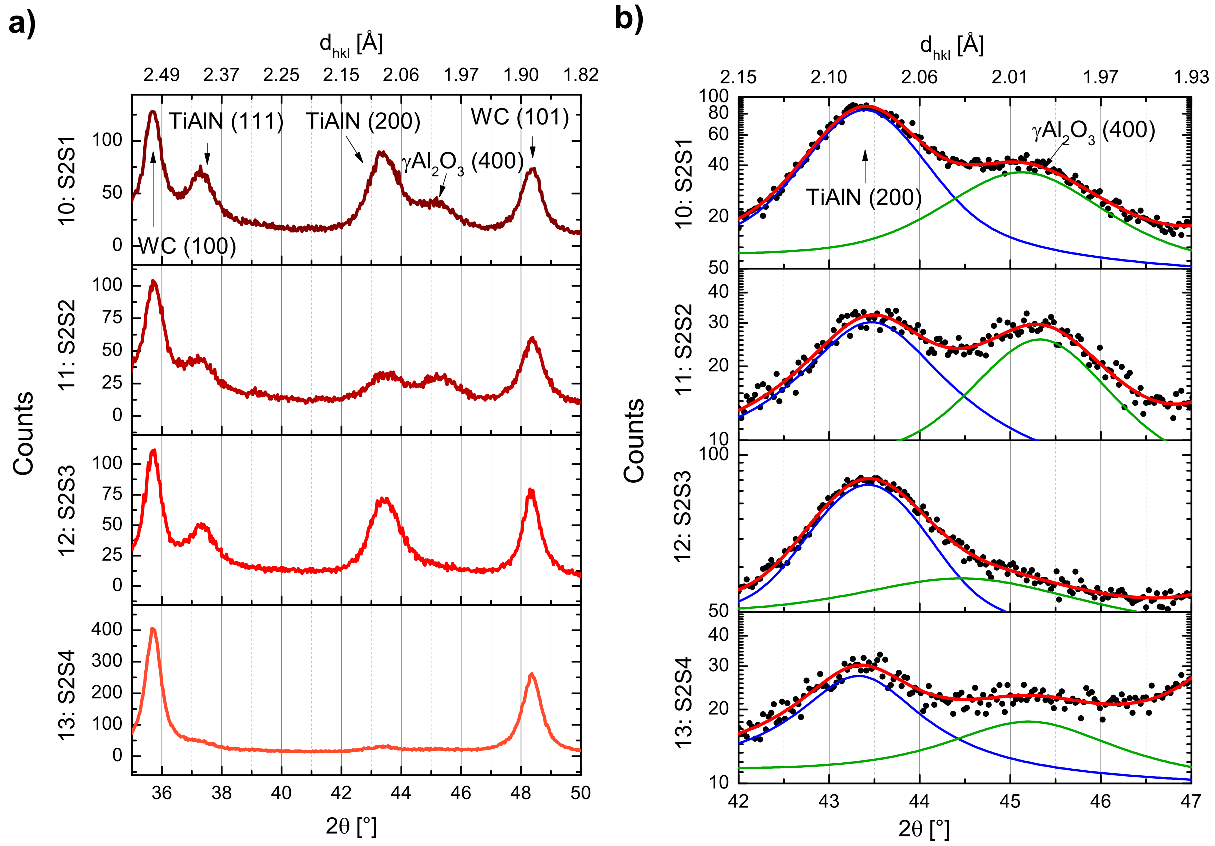

Figure 8.1.: **a)** X-ray diffractogram of all samples 10:S2S1 to 13:S2S4 in grazing incidence mode. **b)** X-ray diffractogram in logarithmic scale in combination with the peak fit (red: overall fit, blue: TiAlN (200) peak fit, green: γ aluminum oxide peak fit).

Sample ID	XRD 2θ[°]	d_{400} [Å]
10:S2S1	45.13 ± 0.02	2.009 ± 0.001
11:S2S2	45.33 ± 0.02	2.001 ± 0.001
12:S2S3	44.50 ± 0.67	2.036 ± 0.029
13:S2S4	45.21 ± 0.26	2.006 ± 0.011

Table 8.2.: Results of XRD experiment (2θ) and calculated d values for γ aluminum oxide (400) peaks using Cu K_α line.

TiAlN (111) and TiAlN(200) respectively.

In the evaluation performed in section 6.3.2, the XRD-2θ value of the (400) peak of γ aluminum oxide was determined and correlated with the sample hardness and Ar mole fraction. Unfortunately, the γ aluminum oxide (400) peak is partly overlapping with the TiAlN (200) peak for samples of series 2. Only by performing a nonlinear background subtraction followed by a peak deconvolution fit to the TiAlN (200), γ aluminum oxide (400) and the WC (101) simultaneously, it was possible to get reproducible results for the γ aluminum oxide (400) peak position, see Table 8.2.

Figure 8.1b shows the diffractograms for $2\theta = 42°$ to $47°$ in logarithmic scale together with the intensity of the TiAlN (200), the γ aluminum oxide (400) and the overall intensity determined by the fit.

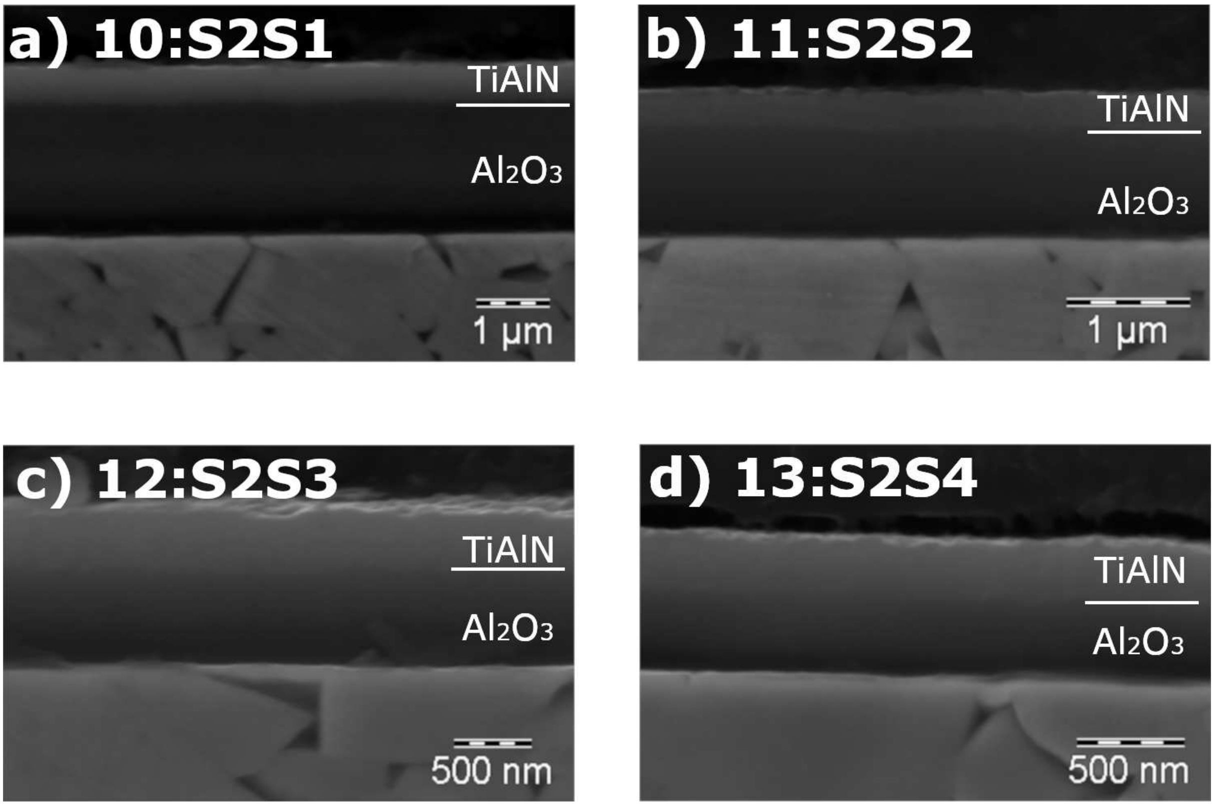

Figure 8.2.: SEM cross-section images of sample 10:S2S1 (**a**), sample 11:S2S2 (**b**), sample 12:S2S3 (**c**) and sample 13:S2S4 (**d**). The samples are oriented such that the substrate is at the bottom of the image.

Cross-section samples were analyzed in the SEM with an acceleration voltage of 10 kV, see Figure 8.2. The WC substrate is seen at the bottom of the image. For all samples, the aluminum oxide film fully covers the substrate homogeneously and the interface to the TiAlN layer appears to be sharply defined. No granular structure was seen as for samples of series 1 with small hardness values, see section 6.3.1.

8.3.2. Quantitative and qualitative chemical analysis using SEM EDX

Quantitative analysis in cross-section

To analyze the Ar mole fraction in the pseudo-γ aluminum oxide films, quantitative EDX in SEM was carried out for cross-section samples. The acceleration voltage was set to 10 kV and the electron beam was positioned in the middle of the aluminum oxide film to maximize the overlap of the excitation volume with the aluminum oxide film. For each sample, at least 10 spectra were acquired at different position across the whole cross-section. Quantitative analysis was carried out for aluminum, oxygen and argon and the averaged results of all acquired spectra are given in Table 8.3. Ar mole fractions range from 1.93 at% for sample 11:S2S2 to 3.04 at% for sample 12:S2S3, yielding slightly higher values as were obtained on the samples of series 1,3 and 4 without a TiAlN layer, see Table 6.4 in section 6.3.2.

Sample ID	Al [at%]	O [at%]	Ar [at%]	Al to Ar ratio
10:S2S1	32.51 ± 1.78	65.40 ± 2.23	2.09 ± 0.48	15.6
11:S2S2	32.45 ± 0.59	65.62 ± 0.59	1.93 ± 0.17	16.8
12:S2S3	34.48 ± 2.75	62.48 ± 0.33	3.04 ± 0.69	11.4
13:S2S4	37.25 ± 1.03	60.18 ± 0.92	2.57 ± 0.40	14.5

Table 8.3.: Quantitative chemical analysis on all samples of series 2 by SEM EDX in cross-section. Spectra were evaluated with respect to Al, O and Ar.

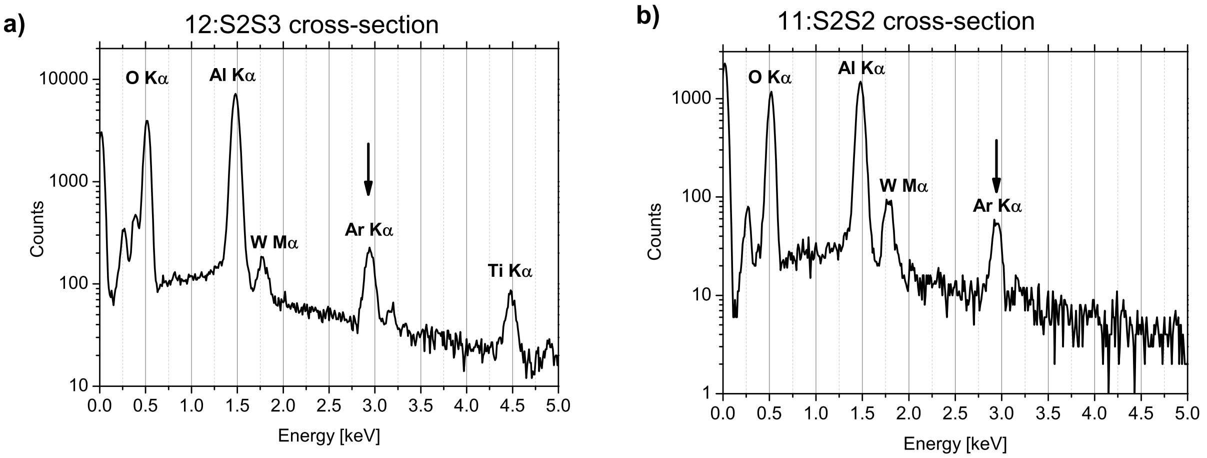

Figure 8.3.: EDX point spectra at 10 keV for **a)** sample 12:S2S3 and **b)** sample 11:S2S2 in cross-section taken in the SEM.

Due to the thin aluminum oxide layer (see Table 8.1), the excitation volume extends into the adjacent material. Therefore, x-rays from the substrate and the TiAlN layer are generated, the latter results in increased counts of the aluminum K_α line. As a result, the Al mole fraction for thin aluminum oxide layers (samples 12:S2S3 and 13:S2S4) is higher in comparison to samples with thicker aluminum oxide layers.

Qualitative linescan analysis in cross-section

For all samples of series 2, EDX line scans were acquired in the SEM with 15 kV acceleration voltage at different positions. Such linescans do not provide quantitative analysis, but show the elemental distribution across the thin films. The spectra are all oriented such that the interface to the substrate is located on the left of the image, see Figures in the Appendix B. The oxygen and titanium linescans of all samples follow the dimension of the corresponding films, showing sharp increases in intensity at the film interfaces. Aluminum is present in both films. As a result, the lines show a sharp increase at the interface to the WC film (similar to the oxygen line) and a drop in intensity at the top end of the TiAlN layer (similar to the Ti line).

The Ar content exhibits the same features that were identified for samples with no TiAlN films of series 1, 3 and 4, see section 6.3.3. All samples show a sharp increase in the Ar content at the interface to the WC susbtrate, similar to the oxygen and aluminum content. This is expected for a sharp interface between the WC substrate and the aluminum oxide film. The maximum Ar content is located close to the interface to the WC substrate. For the Ar content profile across the aluminum oxide film, samples 10:S2S1 and 11:S2S2 show three different types, similar to samples of series 1, 3, and 4: i) an almost linear decay in Ar intensity towards the interface to the TiAlN layer, ii) a constant Ar distribution across the rest of the aluminum oxide film and iii) a second, smaller peak within the aluminum oxide film.

Samples 12:S2S3 and 13:S2S4 have smaller aluminum oxide film thickness, see Table 8.1. The line profiles of the Ar content show the same sharp increase at the interface to the WC substrate, but also a sharp decrease at the interface to the TiAlN layer which is not observed in thicker samples.

This indicates that the aluminum oxide film is similar for all samples at the interface to the WC substrate, where the highest Ar mole fractions are observed. The rest of the film differs for all samples, showing different Ar mole fractions in comparison to the lower part of the film. A detailed investigation of the different layers of the pseudo-γ aluminum oxide films is given in chapter 9.

For samples of series 1, 3 and 4, a correlation was established that linked the sample hardness to the Ar mole fraction as well as to the position of the (400) peak position in XRD. Due to the layer structure of the samples of series 2, no hardness value can be attributed to the aluminum oxide layer. Figure 8.4 shows a plot of the γ aluminum oxide (400) peak position vs the Ar mole fraction of all samples. To highlight the results of series 2 samples, the data points of series 1, 3 and 4 are shown in gray (see Figure 6.2 in chapter 6 for a colorful plot of samples of series 1, 3 and 4). A clear trend can be seen for all samples, including samples of series 2. A higher Ar mole fraction is linked to a smaller 2θ value, and consequently a higher d_{hkl} value. This indicates that a higher Ar mole fraction leads to a larger lattice constant in the pseudo-γ aluminum oxide thin films.

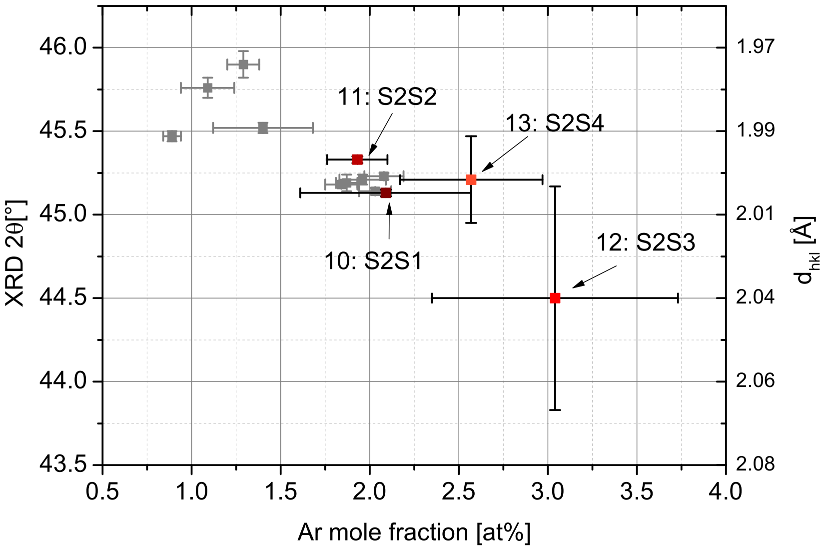

Figure 8.4.: Correlation diagram of the (400) γ aluminum oxide peak position vs Ar mole fraction determined by SEM EDX (in cross-section) for all samples of all series. Datapoints of series 1,3 and 4 are shown in gray, series 2 samples are shown in red. A linear correlation can be seen.

Despite the thin films of samples 12:S2S3 and 13:S2S4, it was possible to analyze their structural and chemical properties. All results indicate that the aluminum oxide films of series 2 samples are similar to that of series 1, 3 and 4. The additional treatment during the HIPIMS deposition of the TiAlN layer does not change the structure of the pseudo-γ aluminum oxide films. This is important for the interpretation and correlation of the electrical measurements in the next section to the structural properties obtained here.

8.3.3. Electrical properties

8.3.3.1. Electrical resistance at room temperature

Electrical resistance was measured for all samples at room temperature. The TiAlN layer served as a contact for the aluminum oxide film, additional preparation steps as for pure aluminum oxide samples were not necessary, see section 7.3.2. The edges of the samples were grinded and polished in parallel to the film to prohibit any current flow from the TiAlN layer directly to the WC substrate.

The TiAlN layer was contacted by metal pins while the WC substrate acted as a back contact. The resistance was measured in cross-plane (i.e. from one of the pins to the substrate) but also in in-plane (between pins). By comparing the resistance value for the cross-plane and the in-plane measurement, it is possible to identify the current flow across the film. For this, the ratio of the resistance in in-plane configuration to twice the cross-plane resistance is calculated.

In case that the in-plane resistance is twice the cross-plane resistance (i.e. ratio of one), the current flow is crossing the aluminum oxide layer twice. A short circuit between the pins through the TiAlN layer would reduce the ratio to values smaller than one. For more details about the possible current paths see Figure 7.6 in section 7.3.3.

Sample ID	Thickness of Al_2O_3 film [nm]	Thickness of TiAlN film [nm]	Cross-plane electrical resistance [Ω]	In-plane to cross-plane
10:S2S1	1762 ± 39	521 ± 39	115 ± 19	0.84
11:S2S2	885 ± 31	294 ± 21	550 ± 92	0.92
12:S2S3	658 ± 77	431 ± 51	194 ± 36	0.85
13:S2S4	365 ± 5	260 ± 10	1619 ± 366	0.95
14:TiAlN	-	445 ± 27	3.2 ± 1.0	-

Table 8.4.: Sample IDs, layer thickness and electrical resistance for all samples of series 2 and the reference sample 14:TiAlN. The last column gives the ratio of the in-plane resistance to twice the cross-plane resistance.

The resistance was measured at different positions across the samples and the results were averaged, see Table 8.4. In addition to the samples of series 2, a reference sample consisting of WC substrate with a single TiAlN on top was investigated. The electrical resistance at room temperature shows large variations between the samples from 115 Ω for sample 10:S2S1 to 1619 Ω for sample 13:S2S4. The in-plane to cross-plane ratio is close to one (smallest value 0.84 for sample 10:S2S1), indicating that the current is in fact crossing the pseudo-γ aluminum oxide layer.

The resistance values are much higher in comparison to Au contacted pseudo-γ aluminum oxide films of series 1, 3 and 4, where room temperature resistance was in the range of 9-11 Ω for high hardness samples.

The TiAlN layer has a higher electrical resistance in comparison to the Au contacts of section 7.3. The measured thickness of the TiAlN layer of sample 14:TiAlN was about 10x higher than the sputtered Au contacts (see Table 8.4 and Table 7.3 in section 7.3.3) but shows higher resistance values in comparison to values measured for pure WC substrate (0.5 Ω).

This indicates that the higher resistance of samples of series 2 is a result of the lower electrical conductance of the TiAlN layer in comparison to sputtered Au contacts. The mechanical stability of the TiAlN contact layer was outstanding, no scratches or damages were observed during the measurement. As a result, the TiAlN layer provides a high-ohmic contact to the pseudo-γ aluminum oxide layer, but is mechanically more durable than the Au contacts that were scratched off during repeated electrical measurements.

The higher resistance of the TiAlN layer also provides an explanation for higher resistance values measured on thinner samples. To investigate the current flow through the TiAlN contact layer and to estimate the electrical resistivity of the pseudo-γ film, current flow simulations were performed for sample 10:S2S1 using COMSOL Multiphysics [139]. Only sample 10:S2S1 was used for the simulations due to the highest film thickness and comparable TiAlN thickness to the reference sample 14:TiAlN.

As a first step, the current flow through the reference sample was simulated, using the film thickness determined in SEM and the overall electrical resistance from Table 8.4. The contact area of the metal pin was estimated from light microscopic images of scratched Au contacts to be 6.25 μm^2. The electrical resistivity of tungsten carbide was taken from [140]. To reduce the computational load, a rotational symmetry perpendicular to the film interfaces was assumed, see Figure 8.5.

The simulation result gave an estimated resistivity for the TiAlN layer of $\rho_{TiAlN} = 0.015\,\Omega cm$.

In the next step, sample 10:S2S1 was simulated using the TiAlN resistivity determined for reference sample, film thicknesses from SEM and overall resistance from Table 8.4.

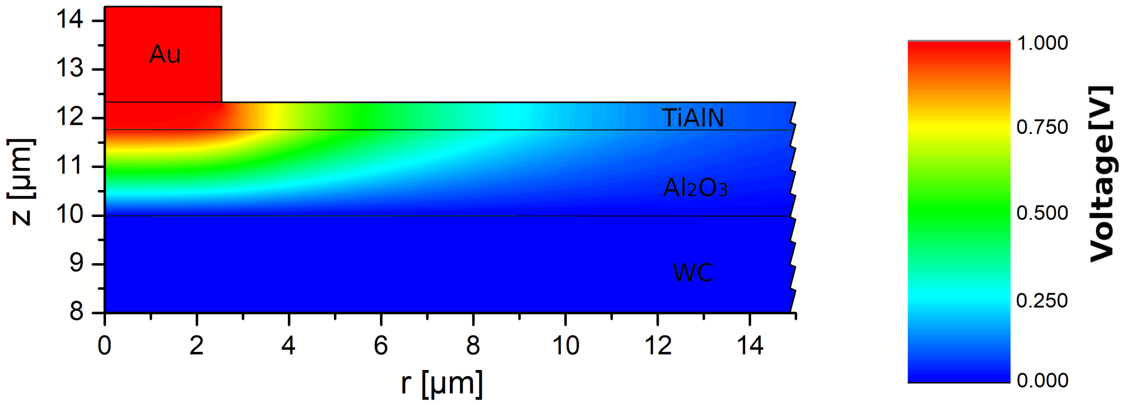

Figure 8.5.: Cut out of simulated voltage drop across the different layers of sample 10:S2S1 using COMSOL Multiphysics. The z-axis is also the symmetry axis for the rotational symmetry. The lateral dimension was cut to highlight the voltage distribution below the Au contact pins.

Figure 8.5 visualizes a cut-out of the simulated voltage distribution across sample 10:S2S1. It shows how the current flow (linked to the voltage drop) is guided laterally through the top TiAlN layer. With decreasing layer thickness, lateral current flow is restricted, resulting in an smaller effective contact area. This leads to a higher resistance for thinner TiAlN contact layers as observed for samples of series 2.

From the simulation, the electrical conductivity for the pseudo-γ aluminum oxide layer was determined as $\rho_{10:S2S1} = 0.36\,\Omega cm$. This simulation can only serve as an estimate, since the resistivity of the TiAlN layer and contact area can only be estimated themselves. Bright et al. give an overview of the improvement of electrical resistivities for various binary transparent conductive oxides [10]. The simulated resistivity of pseudo-γ aluminum oxide is about a factor of ten higher in comparison, but a more detailed investigation of samples with defined contact areas are necessary to precisely determine the electrical resistivity for the pseudo-γ aluminum oxide film.

8.3.3.2. Electrical measurements from 80 K to room temperature

To further analyze the electrical properties of the samples and the pseudo-γ aluminum oxide film, temperature dependent resistance measurements were performed. Small pieces (10 mm x 5 mm) of the samples were cut out and the WC substrate was thinned down to a few mm to reduce the thermal mass of the samples. Using an optical cryostat, the temperature can be controlled within a range of 80 K to 300 K (room temperature). To reduce the impact of the exact contacting position, a small drop of silver paste was put on top of the samples. This leads to an increased contacting area and a more homogeneous current flow in comparison to small pin contacts as in Figure 8.5.

The electrical resistance was determined from the slope of the voltage and current pairs recorded for a voltage sweep from −10 mV to 10 mV. In addition to all four samples of series 2, two reference samples were investigated: i) sample 1:S1S1 served as a reference sample for the pseudo-γ aluminum oxide film and ii) sample 14:TiAlN for the TiAlN top layer.

Sample ID	Electrical resistance at room temperature [Ω]	Relative increase from 300 K to 80 K
1:S1S1	4.4	4.3
10:S2S1	57	1.8
11:S2S2	260	1.9
12:S2S3	230	1.8
13:S2S4	683	3.4
14:TiAlN	6.5	1.8

Table 8.5.: Room temperature resistance and relative resistance increase from room temperature to 80 K for all small cryostat samples under investigation.

The electrical resistance at room temperature of the smaller cryostat samples is given in Table 8.5. In comparison to the full samples, the resistance is smaller due to the increased contacting area, but the trend between the samples remains the same.

All samples are characterized by a negative temperature coefficient, i.e. the resistance increased with decreasing temperature, see Table 8.5. Sample 1:S1S1 shows the highest increase in resistance from 300 K to 80 K by a factor of 4.3. The smallest increase factor of 1.8 is observed for the TiAlN reference sample 14:TiAlN. The resistance ratio obtained for each sample of series 2 ranged in between the values of the reference samples (1.8 for 14:TiAlN and 4.3 for 1:S1S1).

In consecutive cooling cycles, measurements proved to be reproducible on all samples of series 2 and the TiAlN reference sample, indicating a high mechanical stability of the layers. Sample 1:S1S1 differs from the former, since the sputtered Au contacts only lasted for the recording of two cooling cycles, where measurements showed higher variation between each run.

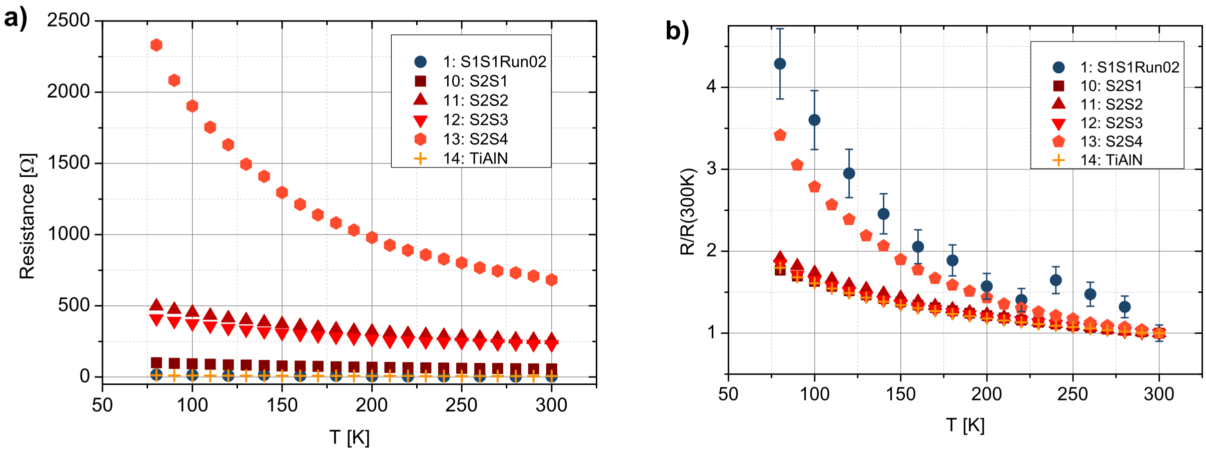

Figure 8.6.: Temperature dependent increase of electrical resistance of all samples. Error bars are obtained from the linear fit to the voltage sweep. **a)** shows the resistance as measured, **b)** shows the change in the resistance (normalized to resistance at 300K).

Since the contact area is not known, the analysis is focusing on the temperature dependency for all samples. For the plot in Figure 8.6, the temperature curves were divided by their resistance value at 300K to show the relative increase of the electrical resistance.

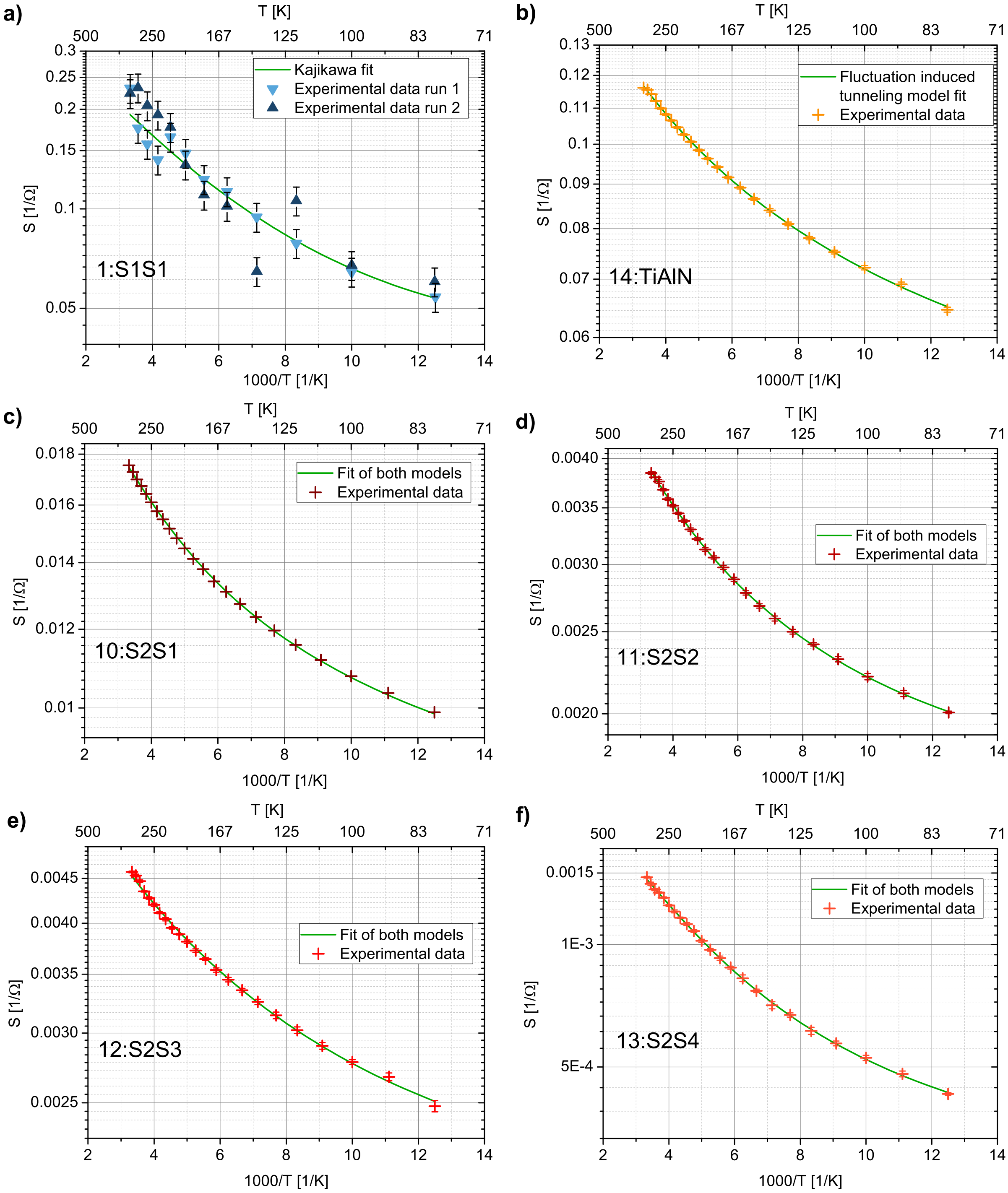

Figure 8.7.: Arrhenius plots of electrical conductance experimental data as well as obtained fit for all samples: **a)** and **b)** shows reference samples 1:S1S1 and 14:TiAlN respectively, **c)** to **f)** show samples 10:S2S1, 11:S2S2, 12:S2S3 and 13:S2S4.

Figure 8.7 shows Arrhenius plots (logarithmic scale for conductance vs inverse temperature) for all samples. In case of a single crystalline semiconductor with thermally activated transport (i.e. thermally activated charge carriers) the temperature dependence of the resistivity can be expressed as

$$\rho(T) = \rho_0 \, exp\left(\frac{E_a}{k_B T}\right) \tag{8.1}$$

where E_a is the activation energy of the charge carriers and k_B Boltzmann constant.
In an Arrhenius plot, equation 8.1 results in a straight line with a slope of $-\frac{Ea}{k_B}$. But for polycrystalline semiconductors, not only the temperature dependence of the carrier density has to be considered, but the temperature dependence of their mobility has to be taken into account as well according to

$$\frac{1}{\rho} = \sigma = n \, e \, \mu \tag{8.2}$$

where *n* is charge carrier density, *e* the carriers charge and μ the carrier mobility. Therefore, the electrical resistance exhibits a curved shape in the Arrhenius plot [141, 142].
An overview of different models to explain this curvature can be found in [143]. Depending on the underlying mechanism, the curvature yields information about the structure of the films, depending on which model describes the curvature the best. The relevant models for this section are presented in short in the following.

Fluctuation induced tunneling model

The fluctuation induced tunneling model is applicable for polycrystalline conductors, where large metallic, internally connected clusters are separated by a thin insulating layer. The temperature dependence of the fluctuation induced tunneling can be expressed as

$$\rho(T) = B \, exp\left(\frac{T_1}{T + T_0}\right) \tag{8.3}$$

where *B* is a constant and T_1 and T_0 are parameters linked to the barrier height, width and area of the insulating layer between the conductive clusters [144].
Using this model, the temperature dependence of the reference sample 14:TiAlN was matched very well, see Figure 8.7b and Table 8.6 for the fit parameters. Since resistance was measured instead of resistivity, the constant *B* also contains the geometry factor (especially the unknown contacting area).
The match of the fluctuating tunneling model for sample 14:TiAlN indicates that the TiAlN layer consists of highly conductive, large grains, separated by insulating grain boundaries. This is in agreement with results of Rachbauer et al. [145] for $Ti_{0.46}Al_{0.54}N$ deposited by sputtering, where they report on the elemental distribution within the grains. They show that in their structure, upon heating to 600 °C, spinodal decomposition takes place, where AlN accumulates at the grain boundaries, leaving a TiN rich grain interior. AlN is known to have a very high electrical resistivity (for cubic as well as for hexagonal configuration) of $\rho_{AlN} > 10^{17}\,\Omega\,\mathrm{cm}$ [140, 146], while TiN is a good electrical conductor with $\rho_{TiN} \approx 20\,\mu\Omega\,\mathrm{cm}$ [140, 147].

In our case, chemical stochiometry of the film, deposited with HIPIMS, is $Ti_{0.33}Al_{0.67}N$. The

Sample ID	a $[10^{-6}\ \frac{1}{\Omega}\frac{1}{\mathrm{K}}]$	b $[10^{3}\ \mathrm{K}^{\frac{3}{2}}]$	$q\overline{\Phi}$ [meV]	$q\sigma_\Phi$ [meV]	H	B [Ω]	T_1 [K]	T_0 [K]
1:S1S1 Run01	60.5	8.6	85	23	3.7	-	-	-
1:S1S1 Run02	75.5	8.3	85	21	4.2	-	-	-
10:S2S1	16.5	5.4	76	47	1.6	0.29	231	125
11:S2S2	3.7	6.9	87	40	2.2	0.32	259	141
12:S2S3	8.4	8.5	87	28	3.1	0.51	213	142
13:S2S4	1.5	4.9	87	29	3.0	0.21	281	130
14:TiAlN	-	-	-	-	-	0.53	281	144

Table 8.6.: Fit parameters for Kajikawa's model (a, b, $\overline{\Phi}$ and σ_Φ, see equation 8.6) and fluctuation induced tunneling (B, T_1 and T_0, see equation 8.3) for all samples of series 2 and the reference samples. The homogeneity factor $H = \frac{\overline{\Phi}}{\sigma_\Phi}$ is given as well.

substrate was kept at 550 °C during deposition. The excess in aluminum (in comparison to the structures of Rachbauer et al.) and the different, highly pulsed deposition technique could lead to an accumulation of the AlN at the grain boundaries even at the slightly lower deposition temperature.

This shows that temperature dependent measurement are capable to reveal structural properties of the thin films. At 300 °C, the temperature coefficient of the electrical resistance of sample 14:TiAlN was determined to be $-1.4 \times 10^{-3}\ \frac{1}{\mathrm{K}}$. This is in good agreement with the results of Park and Kim, who determined coefficients in the range of -1.1 to $-0.7 \times 10^{-3}\ \frac{1}{\mathrm{K}}$ for radio frequency magnetron sputtered $\mathrm{Ti}_{0.33}\mathrm{Al}_{0.67}\mathrm{N}$ films [148].

Inhomogeneous grain boundary models

Curved Arrhenius plot are a common observation for different TCO materials [149, 150, 151]. However, for reference sample 1:S1S1, the above model was not able to describe the curvature in the Arrhenius plots.

In some reports, the temperature range is divided into smaller segments, where the curvature is almost linear and a standard thermally activated transport model is fitted to each region. This results in different activation energies for different temperature regions [152, 153].

Different approaches like variable range hopping were also used to model the curvature, but no good agreement over a wide temperature range was found [143, 154]. Martin et al. tried a different approach to explain the curvature for TiO_2 films based on the Werner model [141, 155].

The Werner model is based on the assumption, that the potential barrier at the grain boundary is not constant, but fluctuates spatially along the boundary, following a Gaussian distribution with mean barrier height $\overline{\Phi}$ and the standard deviation σ_Φ[141].

Under the assumption that the mean barrier height is either independent (temperature coefficient $\alpha_\Phi = 0$) or linearly dependent ($\alpha_\Phi > 0$) on the temperature

$$\overline{\Phi}(T) = \overline{\Phi}(T = 0) + \alpha_\Phi\, T, \tag{8.4}$$

the Werner model describes the electrical resistivity of a polycrystalline semiconductor as

$$\rho(T) = \frac{\rho_0}{T}\, exp \left(\frac{q\,(\overline{\Phi}(T=0) - \alpha_\Phi\, T)}{k_B\, T} - \left(\frac{q\,\sigma_\Phi}{\sqrt{2}\, k_B\, T} \right)^2 \right) \tag{8.5}$$

where q is the carriers charge and ρ_0 and additional fit parameter [141].
Using this model, Martin et al. achieved a good fit of the curvature in the Arrhenius plot for TiO_2 over the full measured temperature range [155]. Werner himself used data from Ueda et al. on $MgIn_2O_4$ to model the temperature dependent behavior [141, 156]. Their derived parameters are given in Table 8.7.

Material	$q\overline{\Phi}$ [meV]	$q\sigma_\Phi$ [meV]	H	Model used	Data from Ref	Fit in Ref
TiO_2	83	29	2.9	Werner	[155]	[155]
TiO_2	113	40	2.8	Werner	[155]	[155]
$MgIn_2O_4$	71	21	3.4	Werner	[156]	[141]
ZnO	275	34	3.4	Kajikawa	[157]	[142]
ZnO	185	65	1.4	Kajikawa	[157]	[142]
ZnO	250	95	1.1	Kajikawa	[157]	[142]
WO_3	160	42	2.9	Kajikawa	[158]	[142]
WO_3	95	39	0.9	Kajikawa	[158]	[142]

Table 8.7.: Fit parameters for Werner's and Kajikawa's models as well as the homogeneity factor $H = \frac{\overline{\Phi}}{\sigma_\Phi}$ for different conductive oxides in literature.

To investigate structural properties of the samples, Werner proposed the ratio of the mean barrier height to the barrier fluctuations as a measure for the homogeneity of the sample (a higher value representing a more homogeneous sample). The homogeneity is given in Table 8.7 as well.

One drawback of the Werner model is that the mean potential barrier height (first part in the exponent in equation 8.5) can become negative as the temperature dependent term is dominant for low temperatures.
To avoid a negative effective barrier in the model, Kajikawa et al. modified Werner's model, leaving out its restricting assumptions. This leads to a integral expression for the conductivity that has to be evaluated numerically

$$\frac{1}{\rho(T)} = a\, \frac{T}{\sigma_\Phi} \int_0^\infty exp\left(-\frac{(\Phi - \overline{\Phi})^2}{2\,\sigma_\Phi^2} \right) \left(\frac{q\,\Phi}{k_B\, T}\, f\,(\Phi,\xi) + \mathscr{F}_0 \left(\xi - \frac{q\Phi}{k_b T} \right) \right) d\Phi \tag{8.6}$$

where a is a fit parameter, $\mathscr{F}_i$ the i-th order Fermi-Dirac integral, $f(\Phi,\xi)$ the Fermi-Dirac distribution

$$f(\Phi,\xi) = \frac{1}{1 + exp\left(\frac{q\,\Phi}{k_B\, T} - \xi \right)} \tag{8.7}$$

and ξ is the reduced Fermi level

$$b = T^{\frac{3}{2}} \mathscr{F}_{\frac{1}{2}}(\xi) \tag{8.8}$$

that has to be adjusted numerically via a second fit parameter b [142].Together with the potential barrier parameters $\overline{\Phi}$ and σ_{Φ}, four fit parameters are needed to adjust Kajikawa's model to experimental data.
Kajikawa used his model to fit the data reported by Roth and Williams [157] on ZnO and Regragui et al. on WO_3 [158]. The obtained fit parameters for the barrier parameters are again given in Table 8.7. In contrast to Regragui's original paper, where a combination of Werner's as well as a tunneling model was necessary to explain the curvature over a wide temperature range, Kajikawa's model was able to fit the whole range [142].

Kajikawa's Model was successfully applied to fit the temperature dependence of the electrical resistance of the reference sample 1:S1S1, see Figure 8.7a and Table 8.6 for the fit parameters.

For all samples of series 2, the sum of equations 8.3 and 8.6 (corresponding to both films connected in series) provided a great fit for all four samples across the whole temperature range, see Figure 8.7. The parameters derived from the combined fit series 2 samples show good agreement with the values obtained for the respective reference samples 1:S1S1 and 14:TiAlN.
In Table 8.6, the derived potential barrier parameters of different conductive oxides are given, derived from Werner's and Kajikawa's model respectively. The values obtained for pseudo-γ aluminum oxide are close to the reported values for different conductive oxides, see Table 8.7. The homogeneity factor is in the range of 1.6 to 3.1 for the series 2 samples and 3.7 (4.2) for run 1 (run 2) of the reference sample.
Within samples of series 2, the fluctuation of the barrier height appears to be smaller for thin layers of pseudo-γ aluminum oxide. This is corresponding to the qualitative chemical analysis in the previous section. All samples showed a high Ar content at the interface to the WC substrate. But only in thicker aluminum oxide films, a second phase with lower Ar content was observed, see also chapter 9. In case of two different layers with different granular structure, the homogeneity factor is expected to be lower as it is seen for sample 10:S2S1, where the layer thickness of the pseudo-γ aluminum oxide film is the highest.
These results illustrate that it is in fact possible to get structural information out of temperature dependent electrical measurements. By determining the right model to explain the curvature of the Arrhenius plot, it is possible to get information about the homogeneity of the sample (in case of the pseudo-γ aluminum oxide films), but also about the chemical distribution within the grains in case of the TiAlN layers. In addition, it is also possible to get this information out of multilayer structure. This is especially helpful in case of single thin films or multilayer structures with individual thickness below 500 nm, where SEM EDX as well as XRD are pushed to their limit.

8.4. Conclusion

Cemented tungsten carbide (WC) is a widely used material for cutting tools. To avoid oxidation, WC tools can be covered with a protective layer. Here, pseudo-γ aluminum oxide, recently discovered to be a transparent conductive oxide, and TiAlN was deposited on top of WC substrate. In case of multilayer structures with layer thickness in the range of hundreds of nanometer, application of standard structural investigation techniques such as x-ray diffraction and SEM EDX is limited by their poor peak intensity and lateral resolution (approx. 1 µm in case of SEM EDX). Still, structural information is elementary for establishing a structure-property correlation and for a deeper understanding of the investigated structures.

In this chapter, it was shown that temperature dependent electrical measurements are a capable tool to probe structural properties of conductive thin films. By carefully choosing the right model to fit the temperature dependence of the electrical resistance, it was possible to investigate the sample homogeneity (in case of pseudo-γ aluminum oxide films) as well as the granular structure and qualitative elemental distribution within TiAlN films.

Especially, it was shown that by applying such structure-property correlation to multilayer structures, it is also possible to get structural information of individual films. This provides an important tool for further investigation on the electrical properties of pseudo-γ aluminum oxide.

9. Pseudo-γ aluminum oxide thin films on SiO_2 substrate

9.1. Introduction

The standard-γ aluminum oxide phase is well known and was investigated in-depth through utilization of various characterization techniques [21, 49, 52, 55, 60, 159, 160]. However, the exact structure is still unknown. The commonly accepted unit cell is the Mn_2O_4 spinel, where the Mg atoms are replaced by Al atoms. To achieve Al_2O_3 stochiometry, only 21 Al ions are available per unit cell to fill 24 cation positions, resulting in cation vacancies [49]. This leads to partially unoccupied sub lattices of the tetrahedral (8a) and octahedral (16d) coordinated aluminum sublattice. Various experimental approaches lead to different interpretations, which Al sublattice is affected the most by the inevitable disorder [21, 49, 55].

Pseudo-γ aluminum oxide was introduced in 2011 by Engelhart et al. and the results of structural investigations are even harder to interpret in comparison to standard-γ aluminum oxide [56]. In terms of electron diffraction in TEM and x-ray diffraction, it is most similar to the γ aluminum oxide phase. But in contrast, pseudo-γ aluminum oxide shows high Ar mole fraction, crystalline and amorphous character in TEM diffraction and even worse x-ray diffractograms in terms of number and intensity of visible peaks [56].

In the previous chapters, the impact of Ar on the structural parameters of the pseudo-γ aluminum oxide phase in terms of hardness and lattice spacings were investigated 6.

The most outstanding property of pseudo-γ aluminum oxide in comparison to other aluminum oxide phases is the fact that it is a transparent conductive oxide, see chapters 7 and 8.

The incorporation of Ar apparently leads to structural changes, creating the possibility for current transport. During the deposition of γ aluminum oxide, Ar is often used as a sputtering gas, but other groups do not report on Ar within their structure [45, 47, 54]. Recently, Zhou reported on HIPIMS deposited aluminum oxide using argon and oxygen as sputtering gases, but again no Ar was found in the aluminum oxide phase[161]. This highlights the importance of the sputtering deposition technique to actually incorporate Ar into the aluminum oxide phases and achieve pseudo-γ aluminum oxide.

Incorporation of noble gas atoms into crystalline structures has been investigated for a long time. But only few publications deal with the effect of noble gas incorporation on the electronic structure of the material. Tkachev showed with photoluminescence and cathodulimenescence experiments that noble gas atoms incorporated in Si and Diamond leads to the creation of deep impurity states and initiates the appearance of a number of bands [162, 163]. They concluded that the compression of the noble gas atoms electron shells by the host material enables the formation of chemical bonds between the noble gas atoms and the host lattice. This experimental work is supported by Gagarin et al., who used an theoretical scattered- wave approach and reported the possibility of chemical bonds between the noble gas atoms with the crystal lattice [164].

Since then, mostly theoretical work and simulations dealt with the effect of noble gas incorporation. But due to the different limitations of the various models the simulations were based on, no universally valid model was derived. For the case of interstitial noble gas atoms, various publications tried to model the effect on the electronic structure of the host material.

Wood et al. reported that incorporation of noble gas atoms can have an effect on the directness of the band gap of zinc blende semiconductors, using a self-consistent local-density approximation (LDA) pseudopotential total-energy method [165]. Estreicher et al. performed ab initio Hartree Fock calculations and found that interstitial noble gas atoms within an Si crystal show no electrical activity themselves, but their effect on the lattice relaxations around the noble gas atoms leads to the narrowing of the gap [166].

Chacham et al. used the Watson sphere terminated cluster model and found that interstitial noble gas atoms induce empty shallow levels close to the bottom of the conduction band of Si.

In comparison to the defect spinel structure of pseudo-γ aluminum oxide, the impact of noble atoms located in vacancies is especially of interest. Mudryi et al. performed extended Hückel theory calculations and showed that noble gas atoms in divacancy centers can lead to local levels in the forbidden band gap of Si due to their effect of the surrounding host crystal [167].

While the stable character of noble gas atoms in divacancy centres was confirmed by different groups using Hartree Fock and density functional theory calculations [166, 168, 169], the role of monovacancies remain unclear (repellent to noble gas atoms [166] or stable positions [168, 169]).

To fully understand the role of Ar in creating a conductive aluminum oxide phase, the structural properties need to be investigated further. In this chapter, the results of detailed TEM imaging, diffraction and analytical investigations on pseudo-γ aluminum oxide samples in cross-section are reported. Samples were deposited on standard WC substrates as in previous chapters, but also on SiO_2 to investigate the possibility to transfer the conductive pseudo-γ aluminum oxide phase on different substrate for possible future applications.

9.2. Experimental procedure

9.2.1. Film deposition and dual magnetron sputtering

For this chapter, both subsets of series 4 (pseudo-γ alumiona on WC and SiO_2 substrate) were used. More details about the deposition process is given in section 2.2.3 and in Table 2.4.

Different deposition bias voltages were used to analyze their effect on the pseudo-γ aluminum oxide structure, −125 V for sample 8:S4S1 and −90 V for 9:S4S2. For future applications as a TCO, the pseudo-γ aluminum oxide films need to deposited onto different substrates.

Sample ID	Batch	HV [Vickers]	Deposition bias [V]	Substrate	Thickness of Al_2O_3 Film [nm]
8:S4S1:WC	6	2435	-125	WC	1060 ± 60
8:S4S1:SiO_2	6	-	-125	SiO_2	1010 ± 88
9:S4S2:WC	7	2930	-90	WC	1040 ± 40
9:S4S2:SiO_2	7	-	-90	SiO_2	1054 ± 111

Table 9.1.: Sample information for series 4 samples. Mechanical properties were only determined for samples with WC substrate, film thickness was determined in the SEM.

Therefore, two different substrates were used. Standard mirror polished cemented tungsten carbide substrates (as were used for samples investigated in chapters 6, 7 and 8) to act as reference samples, as well as insulating SiO_2 substrates to investigate the possibility to adapt the deposition process for new substrates.

An overview of all samples is given in Table 9.1. Film thickness was measured in the SEM. For samples with WC substrate, good contrast between the WC substrate and the aluminum oxide film allows for reproducible determination of the samples thickness. In case of SiO_2 substrates, the contrast between the substrate and the pseudo-γ aluminum oxide film in the SEM images is poor, resulting in a higher uncertainty in the determined film thickness.

9.2.2. X- ray diffraction

Structural characterization of pseudo-γ aluminum oxide films of all samples was performed to analyze possible differences depending on the substrate.
X-ray diffractograms were acquired in grazing incidence mode using Cu-K_α radiation. For more details on the instrumental setup, see 6.3.1. Peak positions were determined using peak deconvolution for the samples with WC substrate (due to overlap of the (400) pseudo-γ peak and the (101) WC substrate peak). In all cases, nonlinear background subtraction in combination with a fit to the peak profile was performed.
Qualitative energy dispersive x-ray spectroscopy was performed in cross-section as well as in plan-view for all samples. In plan-view, acceleration voltage was set to 12 kV so that the excitation volume is probing the aluminum oxide film, but not the substrate. In cross-section, acceleration voltage was set to 10 kV and the electron beam was positioned in the middle of the film to enhance the overlap of the excitation volume with the aluminum oxide film.

9.3. Results and discussion

9.3.1. Structrual investigation by XRD and SEM

In the previous analysis of samples with tungsten carbide substrate, x-ray diffraction in grazing incidence geometry proved to be a valuable tool to reveal distinct features of the pseudo-γ aluminum oxide phase. In comparison to standard-γ aluminum oxide, only few, broad peaks are visible with low intensity (see also section 6.2.2).
It was also possible to analyze the influence of incorporated argon on the crystal structure, i.e. the lattice constant and hardness of the pseudo-γ film. However, one difficulty in the analysis of the x-ray diffractograms stem from high intensity peaks related to the WC substrate, partly overlapping with peaks originating from the pseudo-γ aluminum oxide phase.
For samples on SiO_2 substrates, no peaks are expected due to the amorphous structure of the silicon oxide, highlighting the peaks of the pseudo-γ film.

Figure 9.1 shows the x-ray diffractograms for samples 8:S4S1 and 9:S4S2 on both substrates. Both the (400) and (440) peaks of the pseudo-γ aluminum oxide film are visible in all spectra, independent of the substrate material. Notably, even in diffractograms for SiO_2 substrates, no additional peaks of the aluminum oxide film can be identified. This is again in contrast to the results of Zhou and Synder, who reported three peaks ((220), (311) and (222)) close to $2\theta = 35\,^\circ$ for standard-γ aluminum oxide [49].
Peak positions of the pseudo-γ (400) peak were fitted with nonlinear background subtraction and peak deconvolution for WC substrates, as well as for SiO_2. The results are given in Table

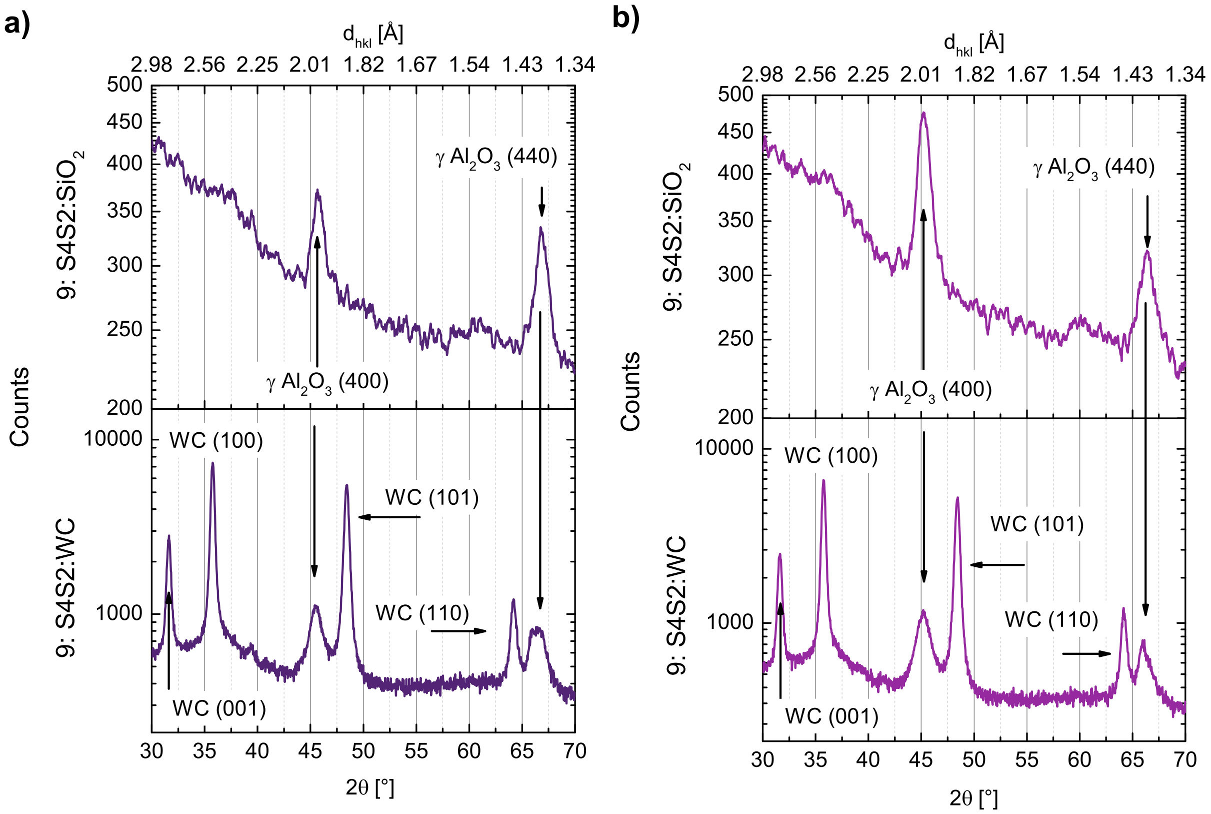

Figure 9.1.: Xrd diffractograms **a)** for samples 8:S4S1 on WC and SiO_2 substrates and **b)** for sample 9:S4S2 on both substrates in grazing incidence mode.

9.2, showing that the peak position is closer within the same batch as between different batches. In terms of x-ray diffractograms, the pseudo-γ aluminum oxide films show the same features, independent of the substrates the films are deposited on. These results highlight once again the differences of pseudo-γ to standard-γ as reported in [49]. Remarkably, Sridharan et al. report similar results on standard-γ aluminum oxide films deposited by refractive magnetron sputtering on Si substrates, using Ar and O as sputtering gases [61]. They did identify a peak close to 35°, but much smaller in intensity compared to (400) and (440) peaks. This indicates that their structure is in fact much closer to pseudo-γ aluminum oxide instead of standard-γ aluminum oxide. Unfortunately, they do not report quantitative chemical analysis of the Ar mole fraction.

Sample ID	$2\theta_{400}$[°]	d_{400} [Å]	Peak-to-background ratio
8:S4S1:WC	45.52 ± 0.03	1.993 ± 0.001	1.7
8:S4S1:SiO_2	45.76 ± 0.13	1.983 ± 0.005	0.4
9:S4S2:WC	45.21 ± 0.03	2.006 ± 0.001	1.9
9:S4S2:SiO_2	45.28 ± 0.06	2.003 ± 0.003	0.8

Table 9.2.: 2θ and the calculated d values (for the Cu-K_α Line) for all samples of series 4 on both substrates.

To further investigate similarities of samples with different substrates, qualitative SEM EDX investigation was performed for cross-section and plan-view samples, as well as qualitative linescans in cross-section. In plan-view, acceleration voltage was adjusted such that the excitation volume penetrates the entire film (i.e. until a substrate peak is visible in the EDX spectrum) and set to 12 kV. In cross-section, acceleration voltage was set to 10 kV and the beam was positioned in the middle of the pseudo-γ aluminum oxide film to enhance the overlap of the excitation volume with the film. For every sample, the measurement was taken at different positions (for cross-section as well as for plan-view) and the results were averaged. The results of the quantitative chemical analysis is given in Table 9.3.

Sample ID	Type	Al [at%]	O [at%]	Ar [at%]	Al to Ar ratio
8:S4S1:WC	PV	32.50 ± 0.46	66.30 ± 0.56	1.19 ± 0.12	27.3
	CS	31.33 ± 0.27	67.24 ± 0.74	1.43 ± 0.27	21.9
8:S4S1:SiO_2	PV	32.79 ± 0.56	65.91 ± 0.63	1.29 ± 0.14	25.4
	CS	30.72 ± 0.34	68.06 ± 0.41	1.23 ± 0.55	25.0
9:S4S2:WC	PV	32.54 ± 1.31	65.38 ± 1.44	2.07 ± 0.19	15.7
	CS	29.24 ± 0.06	68.80 ± 0.12	1.96 ± 0.06	14.9
9:S4S2:SiO_2	PV	32.71 ± 0.29	65.08 ± 0.31	2.21 ± 0.11	14.8
	CS	31.22 ± 0.28	66.89 ± 0.32	1.89 ± 0.11	16.5

Table 9.3.: Quantitative SEM EDX analysis in cross-section (CS) and plan-view (PV) for all samples of series 4 with Al, O and Ar mole fractions included in the analysis.

Samples 9:S4S2 show higher Ar mole fractions as compared to samples 8:S4S1. Again, the differences between batches are higher than within a batch. For SiO_2 samples, the Ar mole fraction are slightly higher than the corresponding WC sample in plan-view, but slightly lower in cross-section, see Figure 9.2.

Qualitative linescans on samples with tungsten carbide substrates revealed characteristic line profiles for the argon content: a sharp increase of Ar content at interface to WC substrate, maximum content close to interface to WC substrate, smaller Ar content in rest of the film. The linescans for all samples of series 4 are given in the Appendix A.

In terms of chemical analysis, samples with SiO_2 reproduce the characteristics of the samples with WC substrate. The same specific line profile is observed after the maximum close to the substrate to pseudo-γ interface for samples 8:S4S1:WC and 9:S4S2:WC. For samples 8:S4S1, independent of the substrate, the Ar line profile is decreasing almost linearly towards the upper end (i.e. interface to air) of the film. In contrast, samples 9:S4S2 on both substrates show a plateau of a higher Ar content before a sharp decrease at the upper end appears.

These differences in the line profile also explain the higher standard deviation in the Ar mole fraction for cross-section analysis of samples 8:S4S1 in Table 9.3. In case of a higher gradient in the Ar profile, the determined Ar mole fraction from a point scan is much more sensitive to the exact beam position within the film. Even small deviations of tens of nanometers in the beam position can result in measurable changes in the determined Ar mole fraction, leading to a higher fluctuation for multiple measurements and therefore a higher standard deviation.

All characterization carried out for samples with different substrates show that the pseudo-γ aluminum oxide phase is forming independently of the substrate. Structural (lattice spacings from

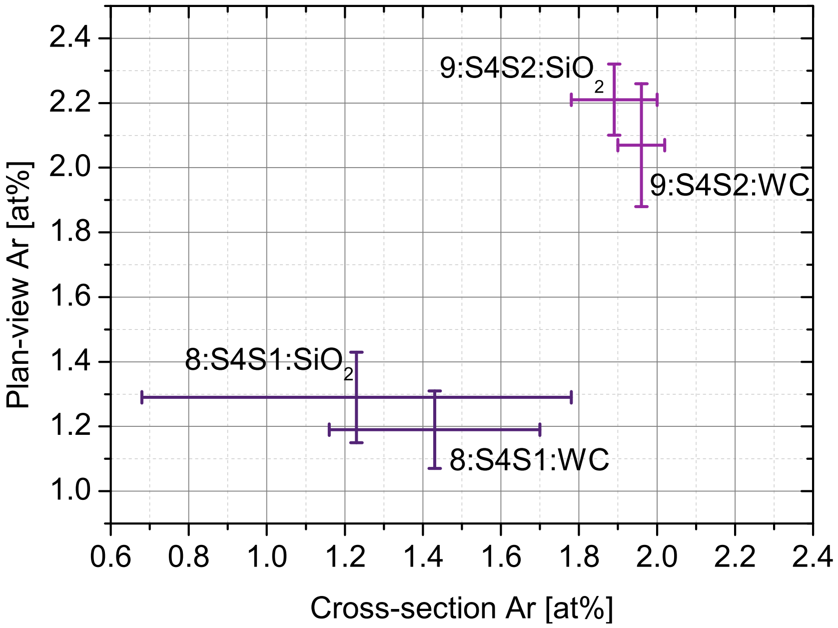

Figure 9.2.: Correlation diagram for Ar mole fraction determined in the SEM by quantitative EDX analysis in plan-view and cross-section.

x-ray diffraction) and chemical (qualitative and quantitative) results are almost identical for samples of the same batch (and different substrate) and differ for samples of different batches. Even specific chemical characteristics such as the Ar lineprofile is reproduced by samples on SiO_2 substrates in comparison to samples with WC substrates.
This illustrates, that the transfer to a non-conductive substrate is possible and that investigations on the pseudo-γ aluminum oxide film are independent on the substrate material.

9.3.2. Structrual investigation by TEM

9.3.2.1. Bright-field imaging

TEM samples were prepared for 8:S4S1:SiO_2 and 9:S4S2:SiO_2 in cross-section by conventional grinding and polishing steps. For more information on the sample preparation and the acquisition conditions, see section 3. Bright- and dark-field images were acquired using energy filtering.
Figure 9.3 shows bright-field images of both samples at 20k magnification. The images are rotated such that the substrate is at the bottom of the image. The pseudo-γ aluminum oxide film appears to have a twofold structure for both samples: i) a multilayer structure at the interface to the SiO_2 substrate (approx. 250 nm-600 nm thick, see Table 9.4) and ii) a granular structure on top.

The multilayer structure is shown in high magnification in Figure 9.3 for both samples. In addition to wider stripes (36 nm for 8:S4S1:SiO_2 and 42 nm for 9:S4S2:SiO_2) already visible for 20k magnifications, the high magnification images reveal additional smaller linear features (approx. 4-5 nm) within the wider stripes, see also Table 9.4.
In case of sample 8:S4S1:SiO_2, the multilayer structure appears to be interrupted by granular

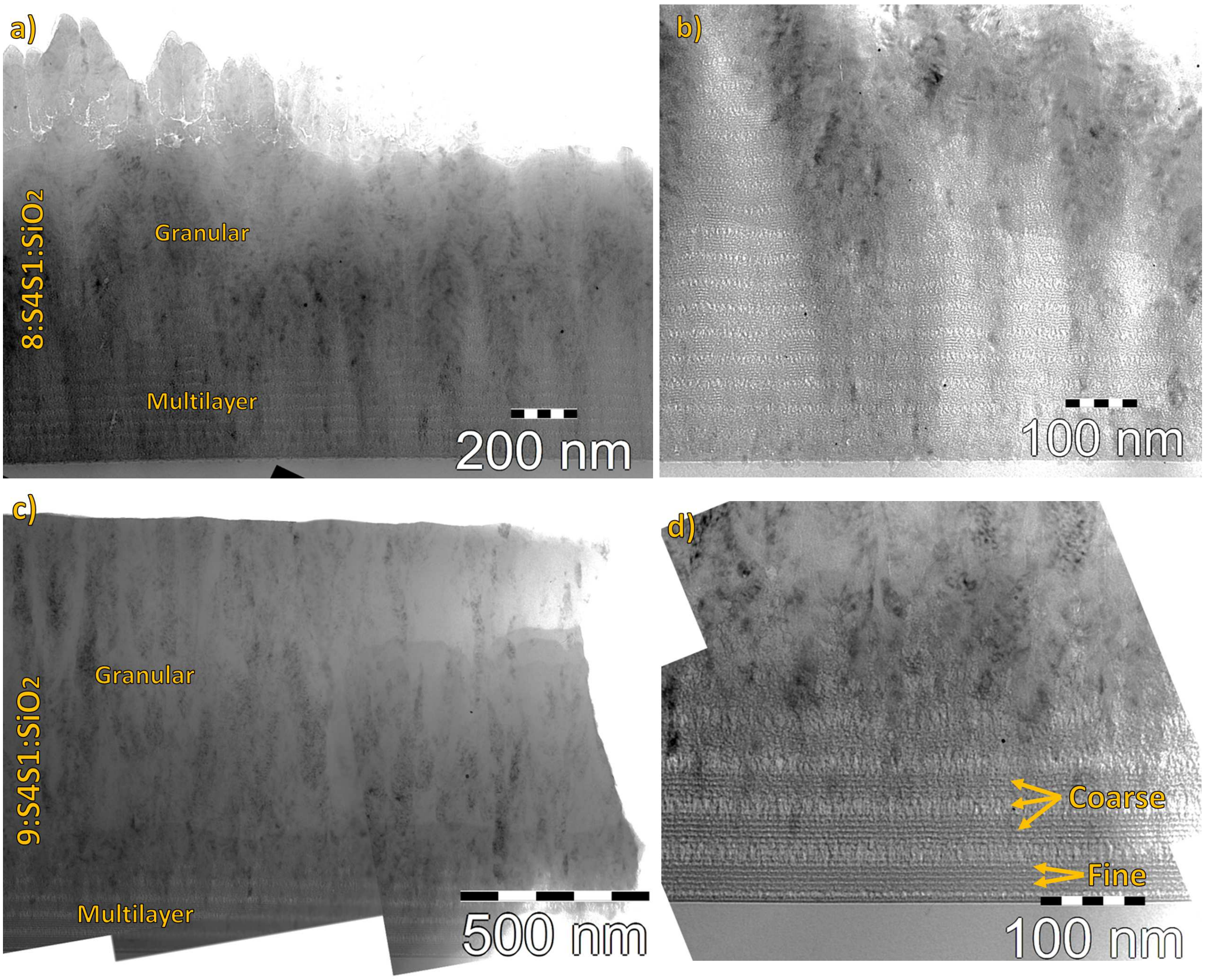

Figure 9.3.: TEM bright-field images for 8:S4S1:SiO_2 (**a,b**) and 9:S4S2:SiO_2 (**c,d**) at 20k (**a,c**) and 50k (**b,d**) magnification in cross-section. The images are orientated such that the substrate is at the bottom of the image.

regions, leading to a zig-zag interface to the upper granular region of the pseudo-γ film. This is different for sample 9:S4S2:SiO_2, where the interface between the multilayer and granular region appears smooth and parallel to the SiO_2-pseudo-γ interface.

9.3.2.2. Electron diffraction and dark-field imaging

To further analyze the crystal structure, diffraction patterns were acquired for both samples using a 700 nm selective area aperture, see Figure 9.4. In agreement with results on pseudo-γ aluminum oxide by Engelhart et al., the diffraction patterns show amorphous and crystalline features simultaneously [56]. For lattice spacings d>2 Å, no crystalline spots are visible and only an amorphous ring remains.

No crystalline spots are seen for reflections of (220), (311) and (222) of γ aluminum oxide. In case of smaller lattice spacings, especially (400) and (440) reflections, crystalline spots with high intensities can be seen.

For sample 9:S4S2:SiO_2, the crystalline spots of (400) and (440) show features of texture, i.e. similar orientation of the pseudo-γ grains. Whereas for sample 8:S4S1:SiO_2, the crystalline spots are distributed randomly along the (400) and (440) circles, indicating random orientation of the pseudo-γ aluminum oxide grains.

Dark-field images were acquired using the (400) ring for both samples. Only for sample 9:S4S2:SiO_2 the intensity in the (440) ring was high enough to acquire dark-field images, see Figure 9.4.

Sample ID	Multilayer thickness [nm]	Grain size horiz. [nm]	Grain size vert. [nm]	Multilayer coarse [nm]	Multilayer fine [nm]
8:S4S1:SiO_2	250 - 600	27 ± 13	80 ± 20	36 ± 1	4.0 ± 0.1
9:S4S2:SiO_2	220	65 ± 17	545 ± 241	42 ± 1	5.2 ± 0.1

Table 9.4.: Measurements of typical features (multilayer dimension and grain sizes) for samples 8:S4S1:SiO_2 and 9:S4S2:SiO_2 in TEM bright-field images.

Sample 8:S4S1:SiO_2 exhibits a micro-granular structure for the upper part of the film with small grain dimensions of 27 nm ± 13 nm horizontally and 80 nm ± 20 nm vertically, see also Table 9.4. In contrast, sample 9:S4S2:SiO_2 shows larger, columnar type grains spanning almost all across the film from the interface to the multilayer part to the top of the film, see Table 9.4.

In both samples, small grains can be seen within the multilayer structure in DF images.

To further analyze the crystal structure, diffraction patterns were acquired for both samples with the selective area aperture centred at the multilayer structure as well as centered in the granular, upper region of the pseudo-γ film. Radial intensity patterns were generated out of these diffraction patterns to reveal additional information within the amorphous ring, see Figure 9.5.

The radial intensity profiles feature high, sharp peaks for (400) and (440) and otherwise small peaks. Even for sample 9:S4S2:SiO_2, where large grains are visible in the dark-field images, the amorphous, broad appearance of (220) is still clearly identified.

This illustrates once more that no amorphous regions lead to the high background for d>2 Å in the electron diffraction patterns, a characteristic feature of the pseudo-γ aluminum oxide

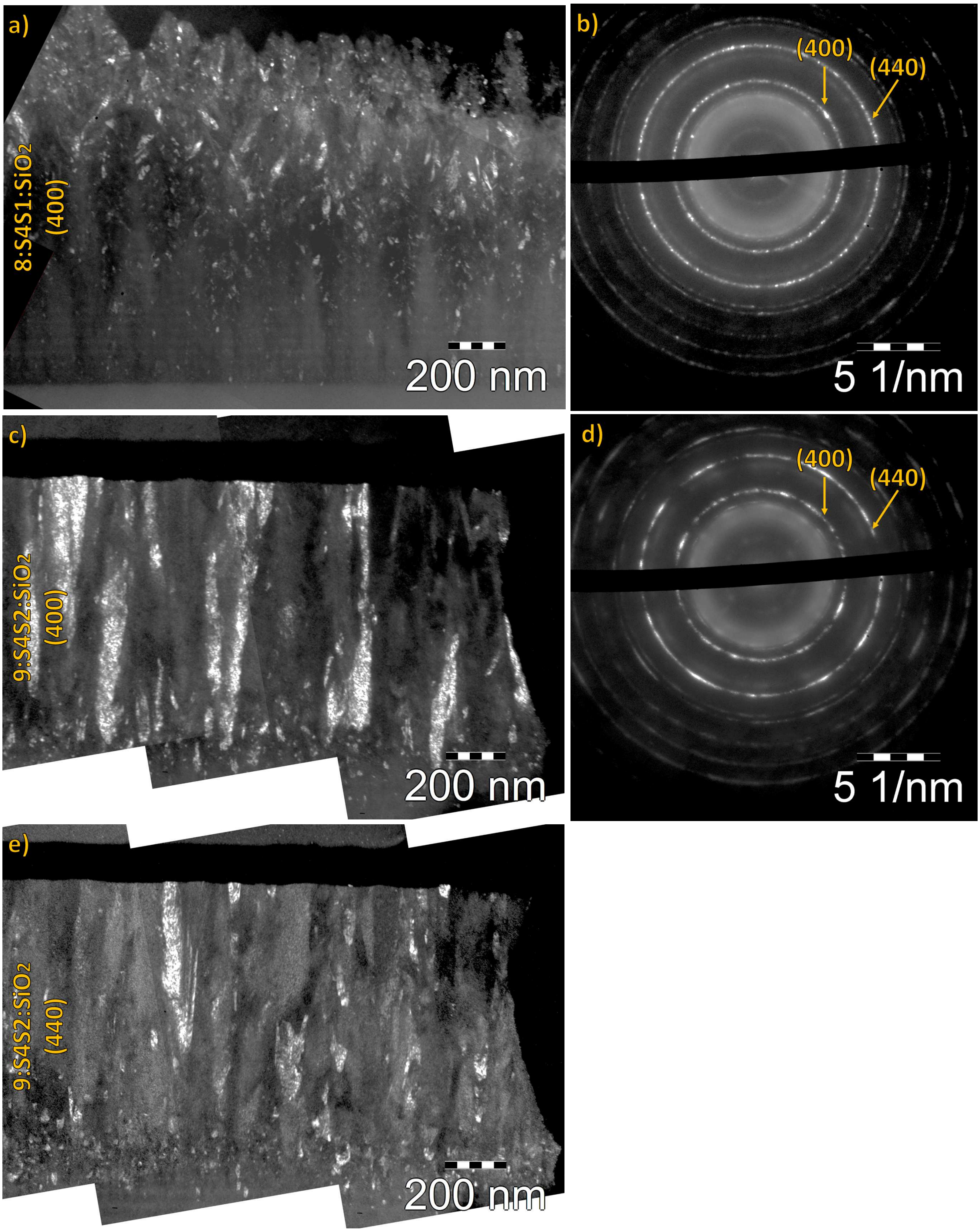

Figure 9.4.: **a)** (400) dark-field image for sample 8:S4S1:SiO_2 in cross-section and **b)** the corresponding diffraction pattern. **c** and **e)** show (400) and (440) dark-field images for sample 9:S4S2:SiO_2 in cross-section and **d)** the corresponding diffraction pattern.

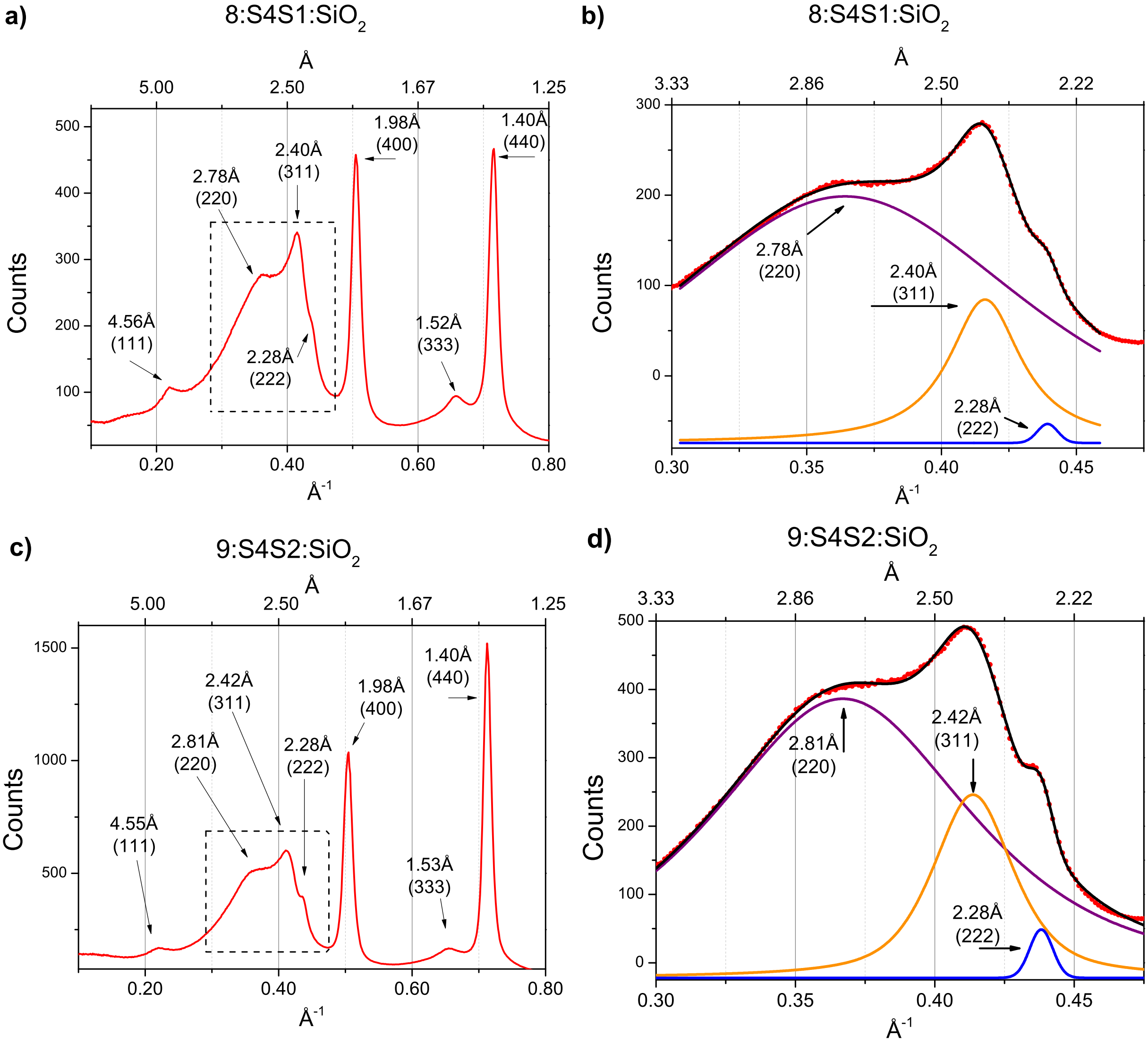

Figure 9.5.: Radial intensity profiles of diffraction patterns for samples **a)** 8:S4S1:SiO_2 and **c)** 9:S4S2:SiO_2. **b)** and **d)** show peak deconvolution fits for peaks (220), (311) and (222) for both samples.

structure. Sridharan et al. also experienced an amorphous background during their TEM investigation, see [61]. They concluded that the amorphous background is not originating from amorphous regions but is linked to the granular structure.

In radial intensity profiles, the amorphous ring can be broken down to contributions from a broad (220) reflection and small, but visible peaks corresponding to (311) and (222) reflections, see Figure 9.5. In previous investigations of Engelhart et al., especially the (222) reflection was not seen. However, the intensity is still much lower as expected for standard-γ aluminum oxide, see [49].

To investigate the disorder, Engelhart et al. calculated the electron diffraction intensities of the Al and O sublattice for the γ Al_2O_3 spinel [56]. Snyder et al. report on the diffraction intensity for XRD, see [49]. Every sublattice shows different contributions to the intensities of various peaks, therefore providing a link between peak intensity and sublattice ordering.

In electron and x-ray diffraction, only the 8a Al sublattice contributes to the (220) reflection. In Figure 9.5, the (220) peak is very broad but clearly visible. For XRD measurements on γ aluminum oxide, Snyder et al. also report a broad, but clearly visible peak [49]. This shows that the 8a Al sublattice is populated, but disordered, leading to broadening of the peak.

The second possible configuration for Al in the Mg_2O_4 spinel is the octahedral 16d position. According to the electron diffraction intensities of Engelhart, the (311) reflection mostly originates from the 16d sublattice. The (222) reflection has contributions from the 16d Al sublattice as well as from the oxygen sublattice. Both peaks are much lower in intensities in comparison to the results of Snyder. This shows that both Al sublattices are disordered for the pseudo-γ aluminum oxide phase.

In the case of oxygen, the 32e sublattice contributes to the (220) peak (but out of phase in comparison to the 16d Al sublattice), and dominates the (440)and (400) peaks in XRD as well as in electron diffraction.

Of all visible peaks in the radial intensity profiles, the (400) and (440) peaks exhibit the sharpest profile. Therefore, the oxygen sublattice appears to have the highest order in comparison to the two Al sublattices. In x-ray diffractograms however, these peaks appear also very broad, leading to the conclusion that the O sublattice also experiences disorder to some degree. These results lead to the conclusion, that pseudo-γ aluminum oxide is in fact similar to γ aluminum oxide in regard of the unit cell, but differs in terms of the lattice disorder: (i) all sublattices are disordered in pseudo-γ aluminum oxide and (ii) no sharp peak is seen for d>2 Å. This is in contrast to standard-γ aluminum oxide, where the (222) peak is still sharp and the O lattice appears to be well ordered [49].

The (400) and (440) peak locations were used to determine the lattice constant of the pseudo-γ film (see Table 9.5). Notably, no differences for the top and the bottom part were observed, but the shift in between samples is in agreement with results of the XRD measurement (see Table 9.5).

Therefore, despite the small intensities and broad peaks in XRD, valid conclusions about the crystal structure of the pseudo-γ aluminum oxide films can be drawn. The investigation of the columnar structure of sample 9:S4S2:SiO_2 in comparison to the micro-granular structure of sample 8:S4S1:SiO_2 is important for understanding the mechanical (i.e. hardness) properties of the samples. In chapter 8, the importance of the grain boundaries for understanding the electrical properties was investigated. Therefore, microstructural analysis is crucial to fully understand the electrical properties of pseudo-γ aluminum oxide thin films.

Sample ID	Lattice constant by TEM [Å]	Lattice constant by XRD [Å]
8:S4S1:WC	-	7.972 ± 0.004
8:S4S1:SiO_2	7.917 ± 0.001	7.932 ± 0.020
9:S4S2:WC	-	8.024 ± 0.004
9:S4S2:SiO_2	7.932 ± 0.001	8.012 ± 0.012

Table 9.5.: Lattice constants of pseudo-γ determined by XRD and TEM diffraction patterns.

9.3.2.3. Quantitative EDX in TEM

Quantitative TEM EDX measurements were performed for both samples to further determine the role of Ar in the formation of the pseudo-γ aluminum oxide phase. The probe size was set to 50 nm for thin and to 80 nm for thicker specimen areas. The quantitative analysis was performed according to the Cliff Lorimer method, see also section 3.3.5.2 and Table 3.5 for the k-factors used in the analysis [82].

Multiple spectra were acquired across the film as marked in Figure 9.6, the results of the quantitative analysis (including O, Ar and Al) are given in Table 9.6.
For both samples, the multilayer structure at the interface to the substrates shows the highest Ar mole fractions up to 7.21 at% for sample 8:S4S2:SiO_2 and 10.62 at% for sample 9:S4S2:SiO_2. This is in agreement with the SEM EDX linescans, where the highest Ar content was always found at the interface to the substrate.
The Ar mole fraction varies within the granular region for both samples. Sample 8:S4S1:SiO_2 with micrograpular structure shows low Ar fractions ranging from 0.44 at% to 3.74 at%, gradually decreasing towards the top of the film. Again, this corresponds to the qualitative SEM EDX linescans, where for sample 8:S4S1 the Ar line profile dropped to lower values after the maximum at the substrate to film interface.

Sample ID	Position	Al [at%]	O [at%]	Ar [at%]	Al to Ar ratio
8:S4S1:SiO_2 Area 1	1	43.99	55.57	0.44	100.0
	2	43.43	55.07	1.50	29.0
	3	44.06	53.91	2.03	21.7
	4	43.50	52.77	3.73	11.7
	5	42.27	50.52	7.21	5.9
8:S4S1:SiO_2 Area 2	1	42.16	57.07	0.77	54.8
	2	42.38	56.81	0.81	52.3
	3	42.98	55.77	1.25	34.4
	4	43.38	53.39	3.23	13.4
	5	41.77	51.38	6.85	6.1
9:S4S2:SiO_2 Area 1	1	44.03	53.31	2.66	16.6
	2	43.59	53.72	2.69	16.2
	3	43.84	53.51	2.65	16.5
	4	43.84	53.59	2.57	17.1
	5	40.45	48.93	10.62	3.8
9:S4S2:SiO_2 Area 2	1	42.66	55.03	2.31	18.5
	2	40.93	56.69	2.38	17.2
	3	41.24	56.22	2.54	16.2
	4	42.30	55.62	2.08	20.3
	5	39.65	50.41	9.94	4.0

Table 9.6.: Results of quantitative chemical analysis in the TEM for samples 8:S4S1:SiO_2 and 9:S4S2:SiO_2. The acquisition positions are marked in Figure 9.6

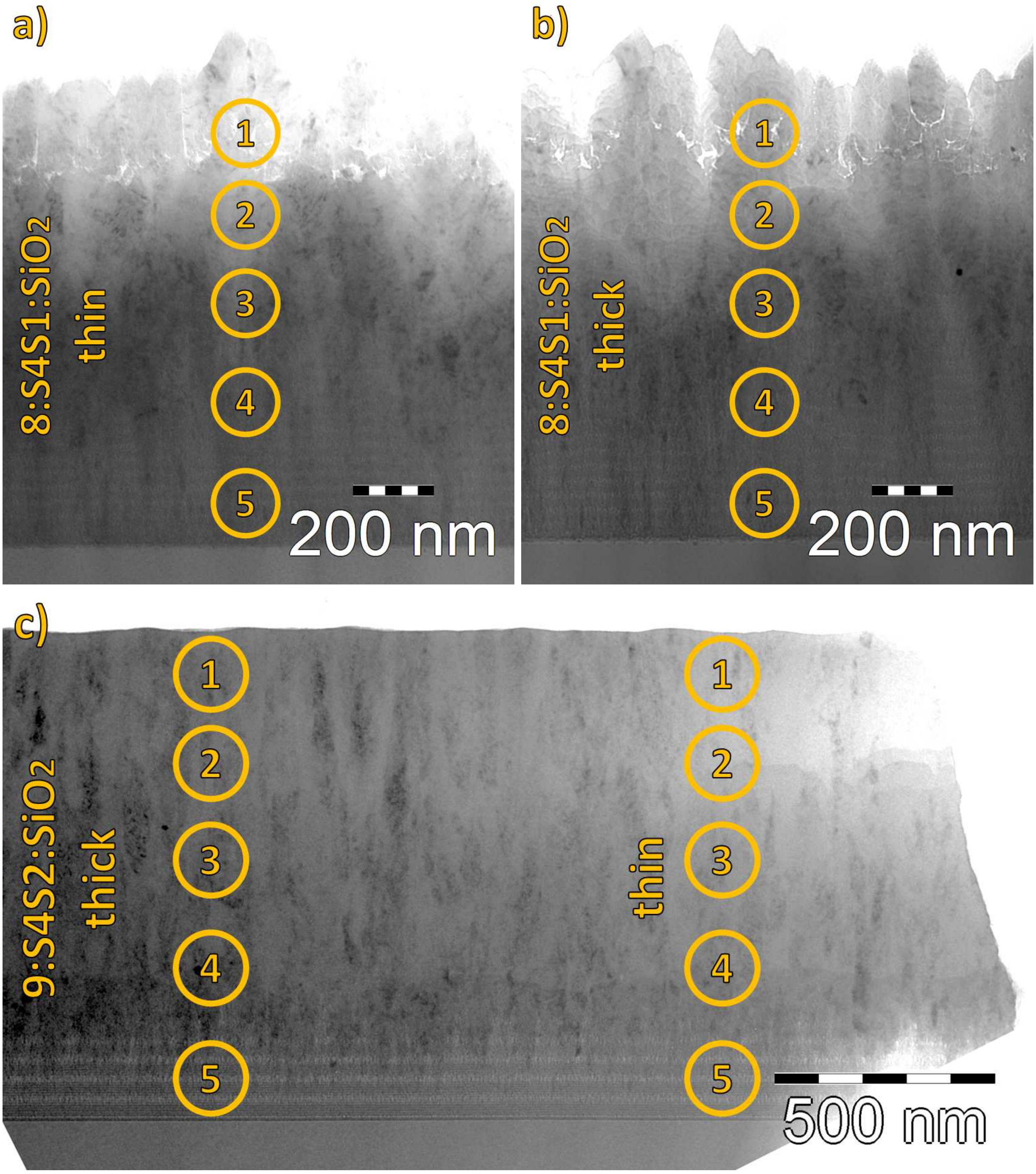

Figure 9.6.: TEM EDX acquisition locations for samples 8:S4S1:SiO_2 (thin **a)** and thick **b)** sample area) and **c)** 9:S4S2:SiO_2 (in cross-section). The results of the quantitative analysis is given in Table 9.6.

In sample 9:S4S2:SiO_2, the Ar mole fraction of the granular region is smaller than in the multilayer region, but higher in comparison to sample 8:S4S1:SiO_2 with Ar mole fractions in the range of 2.08 at% to 2.69 at%. In addition, the Ar mole fraction is homogeneous within the full granular part of the film and no gradient towards the top of the film is detected. Once more, this in good agreement with the qualitative linescans in SEM EDX, where the Ar line profile showed a higher plateau for the region next to the maximum at the interface.

Figure 9.7 shows correlation diagrams of the Ar mole fraction against the Al mole fraction as well as the O mole fraction. In both cases, a negative correlation is seen.

For the micrograngular structure of sample 8:S4S1:SiO_2, the gradual decrease in the Ar content towards the top of the film is accompanied in a gradually increasing O content. For Al, there seems to be two different branches for sample 8:S4S1:SiO_2, where some measurements show only small changes in the Ar content with increasing Al content and others show an decrease in the Ar content when the Al content is increased.

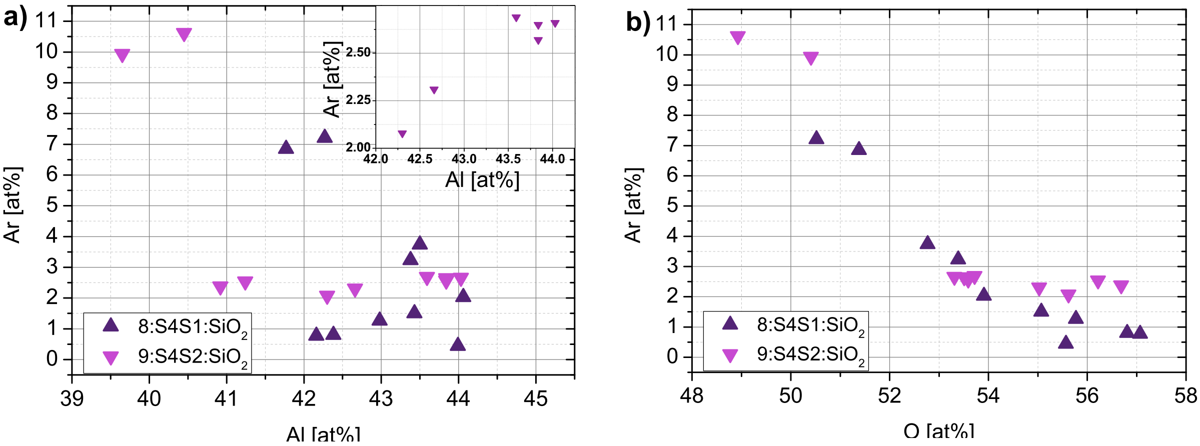

Figure 9.7.: Correlation diagrams for the determined Ar mole fraction to **a)** the Al mole fraction and **b)** the O mole fraction.

The inset in Figure 9.7a highlights the correlation for sample 9:S4S2:SiO_2. The correlation is small, but positive in case of Al and negative in case of O. Strong changes occur as soon as the Ar mole fraction increases beyond 3 at%. To some degree, the Ar atoms can fill the vacancies within the defect spinel structure with only small changes to the overall structure. When more Ar atoms are introduced to the structure, the atoms are replacing O as well as Al atoms from their position within the crystal structure.

In general, TEM EDX point scans confirm the linescans taken in the SEM: i) highest mole fractions at the interface to the substrate and ii) lower (but different for each sample) values for rest of film. Together with TEM bright-field images, the different Ar mole fractions can be linked to structural features of the film.

The higher Ar mole fraction in sample 9:S4S2:SiO_2 with larger grains (and therefore less grain boundaries) shows that the Ar is not accumulated in between grains in an amorphous region, but is incorporated into the grains.

In section 6.3.2, a higher Ar mole fraction of $\approx$2.2 at % (determined by SEM EDX) was successfully linked to the mechanical properties of the samples (i.e. hardness), where higher mole fraction correlated with higher hardness. Bright-field images, in conjunction with TEM EDX measurements, indicate that the granular structure of sample 9:S4S2:SiO_2 is linked to the optimal argon mole fraction and is therefore important for achieving high sample hardness. The role of the multilayer structure has to be investigated further using additional samples to fully understand the role of this structure and its interface to the granular region to the structural and electrical properties.

9.3.2.4. Electron energy loss spectroscopy

Electron energy loss spectra were acquired for all samples at the multilayer and granular part of the pseudo-γ aluminum oxide films of both samples. Figure 9.8 shows the low loss spectra for both samples and both areas.

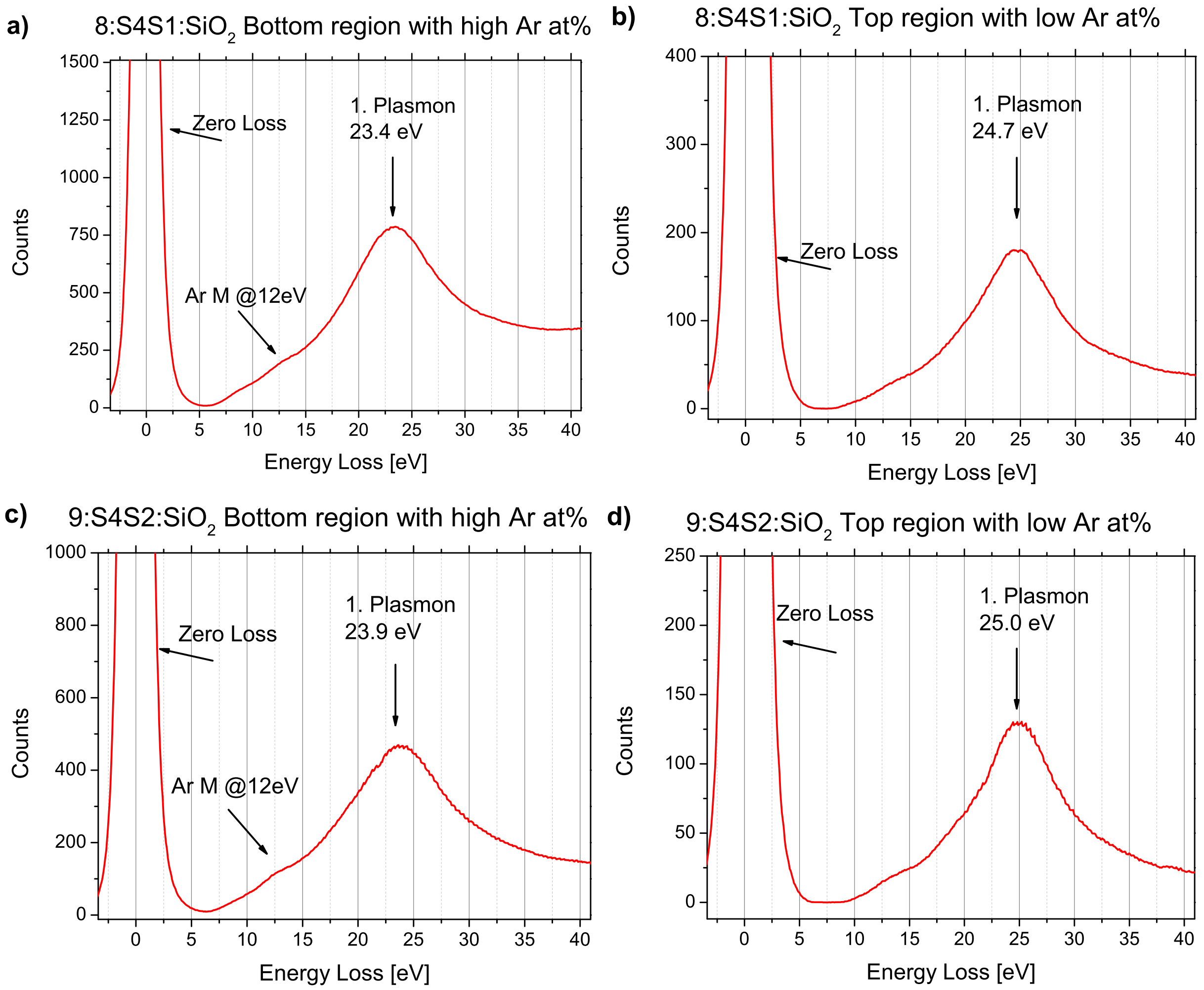

Figure 9.8.: Low loss EELS spectra for samples **(a,b)** 8:S4S1:SiO_2 and **(c,d)** 9:S4S2:SiO_2, acquired at the **(a,c)** bottom and the **(b,d)** top of both samples.

At low energies, energy loss is due to excitation of collective electron oscillations (plasmons). The plasmon frequency depends on the free electron density, their effective mass and is an effective as well as sensitive tool for fingerprinting different phases. The determined plasmon frequency is slightly different for both samples, while for both cases the lower frequency was observed for the multilayer structure (see Figure 9.8). This indicates differences in the electronic structure of the multilayer and the granular part of the pseudo-γ film.

In the literature, different values for the plasmon energy are reported for different aluminum oxide phases, ranging from 22 eV for standard-γ by Strara et al. [170] and 26 eV for standard-γ as well as α aluminum oxide by French et al. [171]. For pseudo-γ aluminum oxide, Engelhart et al. reported 26.1 eV for the plasmon energy. All values determined for samples 8:S4S1:SiO_2 and 9:S4S2:SiO_2 are in between the reported values.

At higher electron loss energies, absorption edges of the present elements can be seen for aluminum (Al $L_{2,3}$) oxygen (O K). The shape of the absorption edge is characteristic for the electronic structure and depends for each element on their coordination and bonds within the crystal structure.

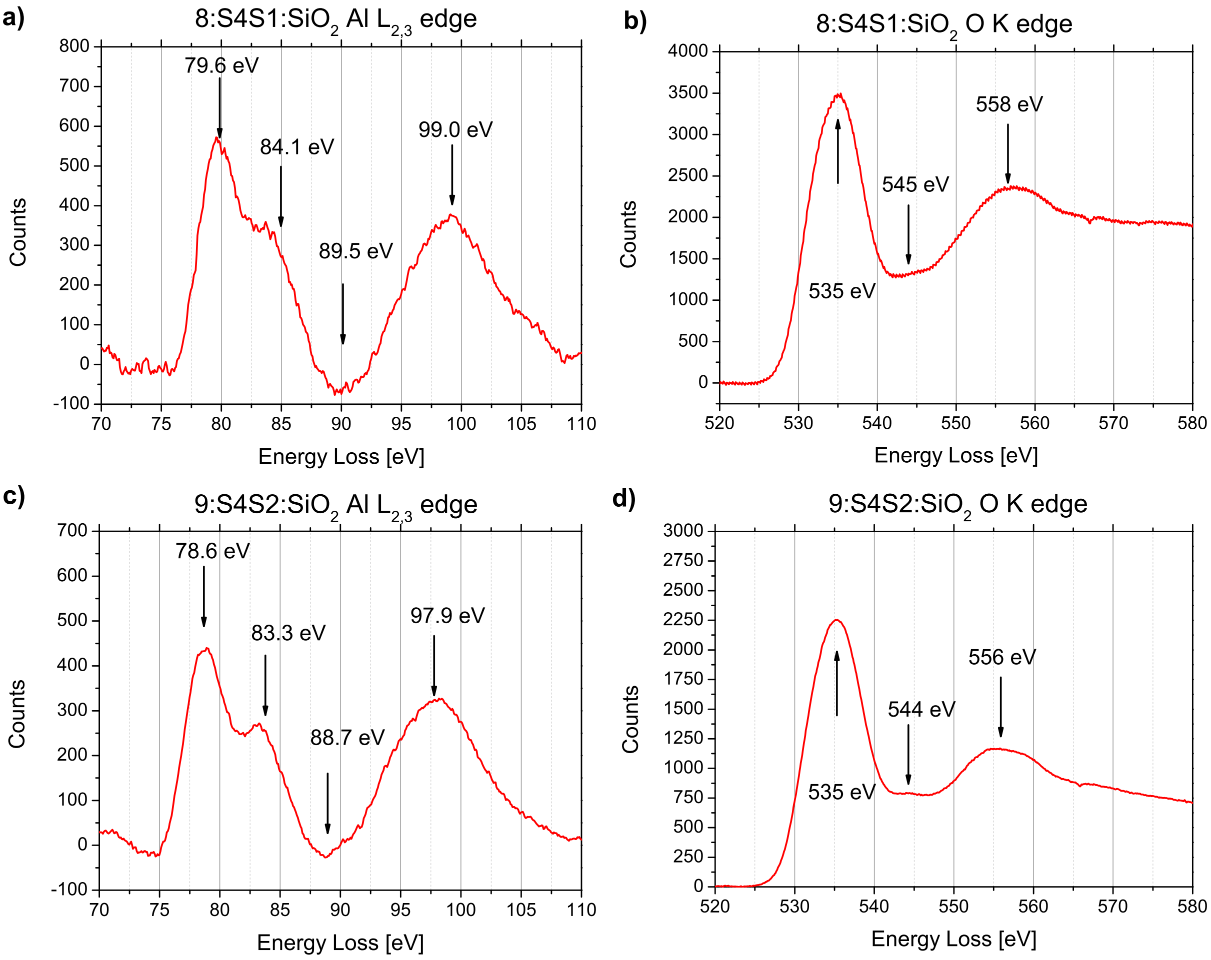

Figure 9.9.: Electron core loss spectra for **(a,c)** Al $L_{2,3}$ and **(b,d)** O K edges for both samples **(a,b)** 8:S4S1:SiO_2 and **c,d** 9:S4S2:SiO_2 acquired in the TEM.

Bouchet et al. give a comparative overview of the shape of the Al $L_{2,3}$ edge for α, γ and amorphous aluminum oxide phases [172]. The recorded core loss spectra for both samples is shown in Figure 9.9. The closest resemblance can be seen for γ aluminum oxide, whereas the spectra of amorphous aluminum oxide shows a significantly higher intensity in the peak close to 97 eV that is not seen for samples 8:S4S1:SiO_2 and 9:S4S2:SiO_2.

Hansen et al. did a comparative study of the shape of the Al $L_{2,3}$ edge depending on the coordination of the Al in silicate structures [87]. The recorded spectra for both samples are more similar for tetrahedral coordination (corresponding to the 8a sublattice) than for octahedral coordination (corresponding to the 16d sublattice). This indicates a higher disorder for the 16d sublattice in comparison to the 8a sublattice.

Figure 9.9 shows the core loss spectra of the O K line for both samples. Again, the shape is characteristic for the type of bonds the O atoms form to the surrounding atoms in the crystal structure. Grunes et al. give an overview of the shape in different metal oxides [86], Nyquist et al. report on the edge shape for oxygen in different types of spinel structures [173].

For aluminum oxide oxides, the shape of the O K line does not differ strongly for α (as reported by Kaneko et al. [174]), γ (see Borisevich et al. [175]) as well as pseudo-γ aluminum oxide (see Engelhart et al. [56]).

In comparison to the core loss spectra reported by Engelhart, the intensity of the first peak at 535 eV in Figure 9.9 is significantly lower compared to the second peak at 553 eV-558 eV.

9.4. Conclusion

In conclusion, the transfer of the pseudo-γ aluminum oxide phase to non conductive substrates such as SiO_2 is possible and can be used for further development of applications of pseudo-γ aluminum oxide as a transparent conductive oxide. All structural investigations of x-ray diffraction and qualitative as well as quantitative EDX in the SEM show that the characteristic structural features of pseudo-γ aluminum oxide are reproduced by the thin films deposited on SiO_2 substrates.

TEM investigation in cross-section revealed a multilayer structure at the interface, incorporating very high Ar mole fractions up to 10 at%. This observation gives a structural explanation for the SEM EDX linescans in sections 6.3.3 and 8.3.2, where the highest Ar content was always found at the interface to the substrate. The shape of the SEM EDX linescans for the rest of the pseudo-γ film was linked to the granular structure of the film. Low Ar content is measured for small grains, whereas high, constant Ar content corresponds to larger, columnar grains. This proves that Ar is in fact incorporated into the spinel crystal structure and is not leading to regions of amorphous aluminum oxide, as is also shown by dark-field images and EELS core loss analysis of the Al $L_{2,3}$ edge.

This correlation of different characterization techniques is necessary as their combination can help to develop a full picture of the structural features of the pseudo-γ aluminum oxide phase. The high Ar mole fraction was linked to distinct features in the electron diffraction patterns (and therefore the crystal structure) and shows once again the differences to the standard-γ phase. To fully understand the role of Ar in forming a transparent conductive oxide, additional measurements of the electric properties of samples deposited on SiO_2 are necessary.

Appendices

A. SEM EDX linescans in cross-section

SEM EDX linescans acquired for all samples in cross-section.

Series 1

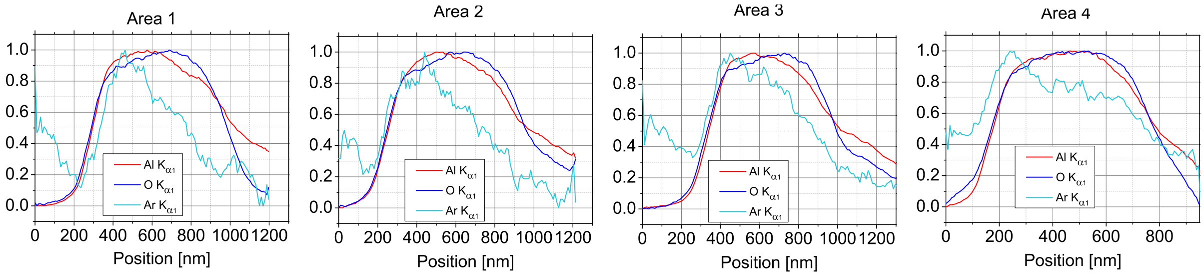

Figure A.1.: SEM EDX linescans in cross-section for sample 1:S1S1.

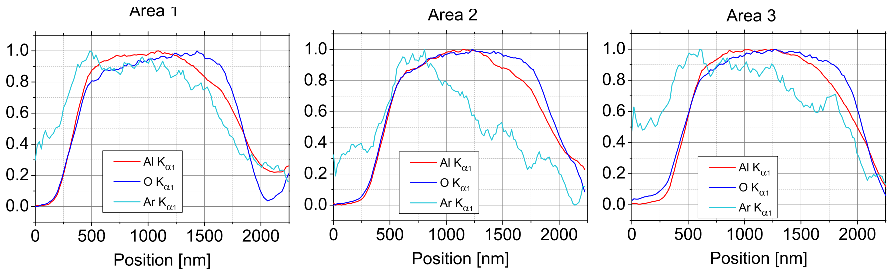

Figure A.2.: SEM EDX linescans in cross-section for sample 2:S1S2.

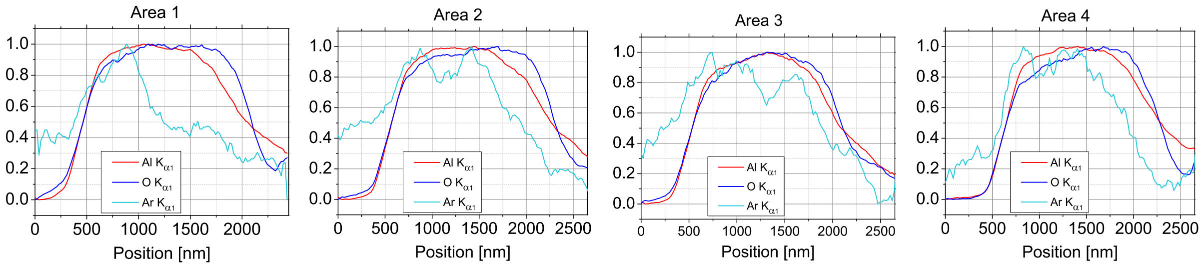

Figure A.3.: SEM EDX linescans in cross-section for sample 3:S1S3.

Series 2

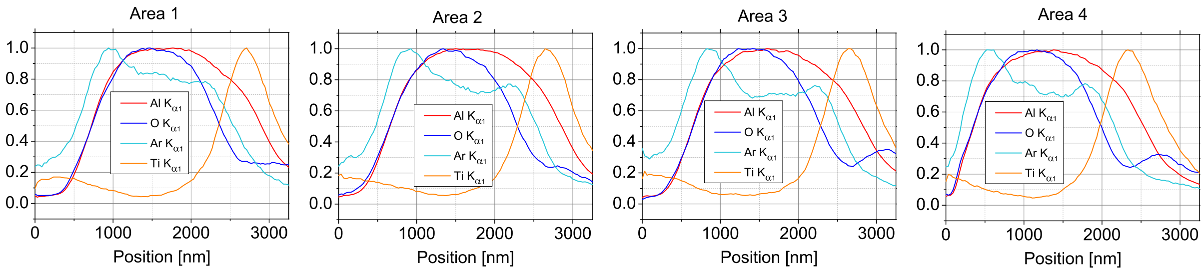

Figure A.4.: SEM EDX linescans in cross-section for sample 10:S2S1.

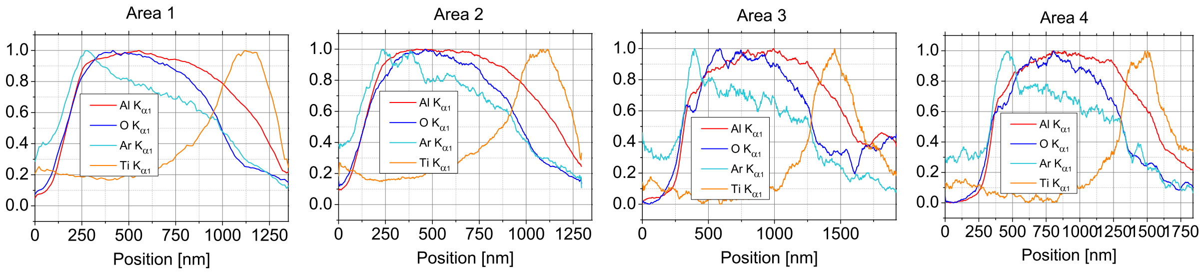

Figure A.5.: SEM EDX linescans in cross-section for sample 11:S2S2.

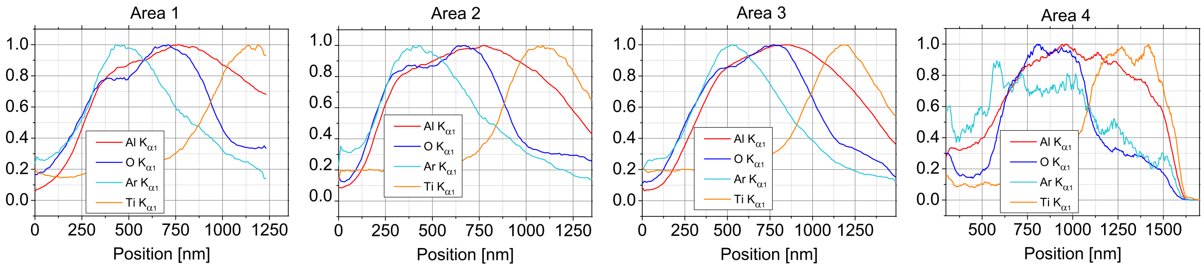

Figure A.6.: SEM EDX linescans in cross-section for sample 12:S2S3.

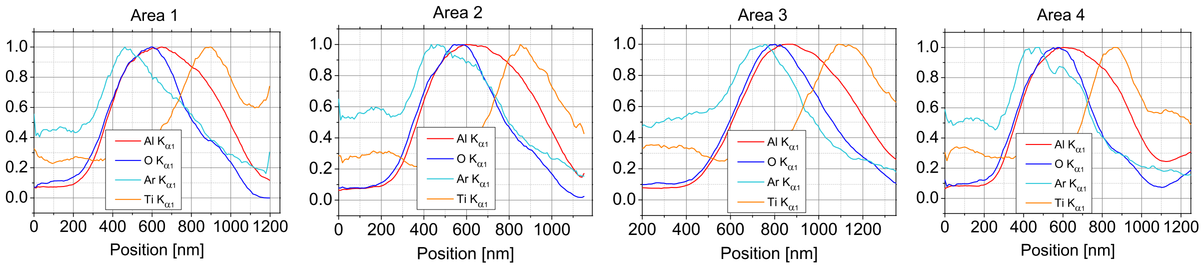

Figure A.7.: SEM EDX linescans in cross-section for sample 13:S2S4.

Series 3

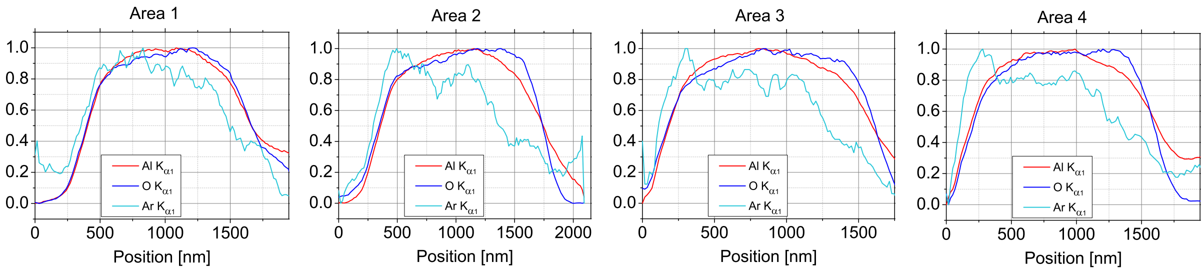

Figure A.8.: SEM EDX linescans in cross-section for sample 4:S3S1.

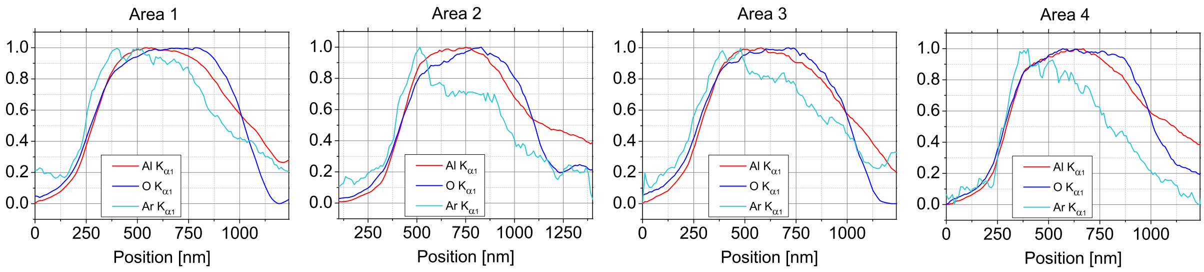

Figure A.9.: SEM EDX linescans in cross-section for sample 5:S3S2.

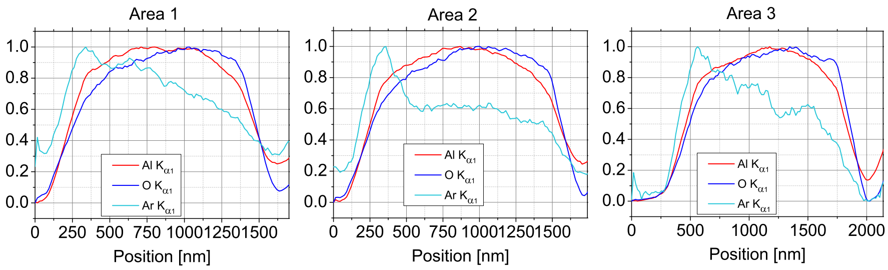

Figure A.10.: SEM EDX linescans in cross-section for sample 6:S3S3.

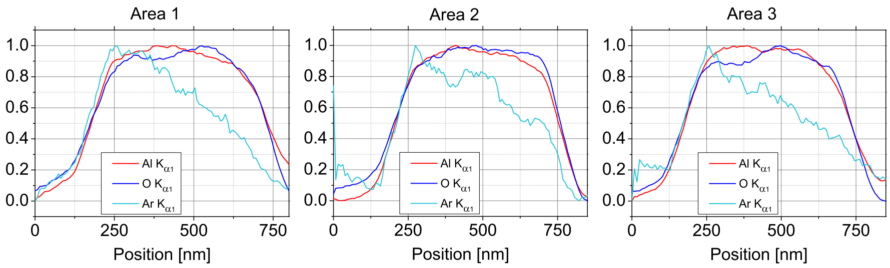

Figure A.11.: SEM EDX linescans in cross-section for sample 7:S3S4.

Series 4

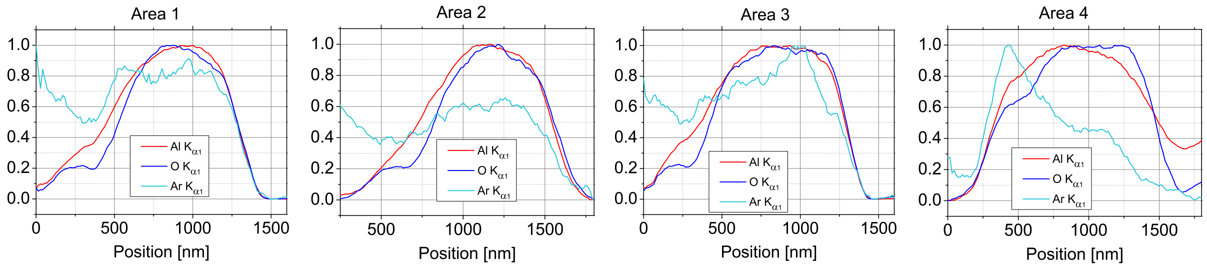

Figure A.12.: SEM EDX linescans in cross-section for sample 8:S4S1 on WC substrate.

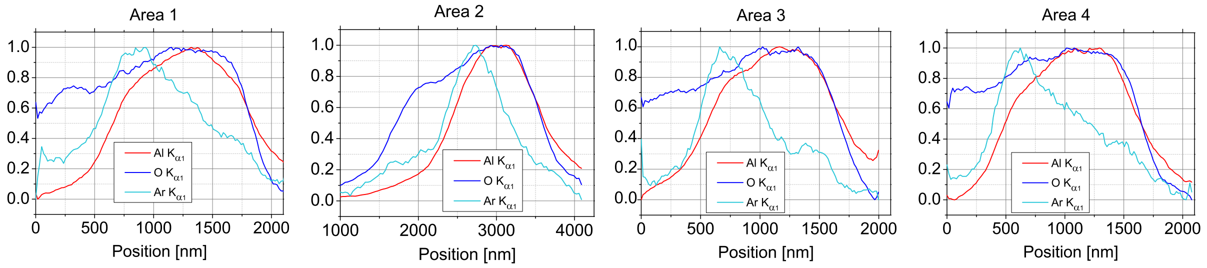

Figure A.13.: SEM EDX linescans in cross-section for sample 8:S4S1 on SiO_2 substrate.

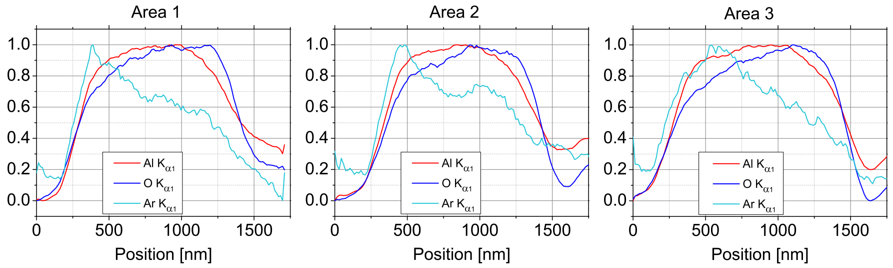

Figure A.14.: SEM EDX linescans in cross-section for sample 9:S4S2 on WC substrate.

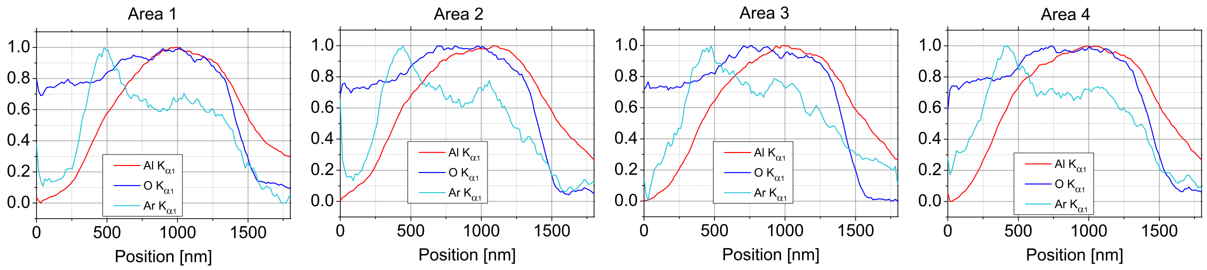

Figure A.15.: SEM EDX linescans in cross-section for sample 9:S4S2 on SiO_2 substrate.

B. Peak deconvolution of x-ray diffractograms

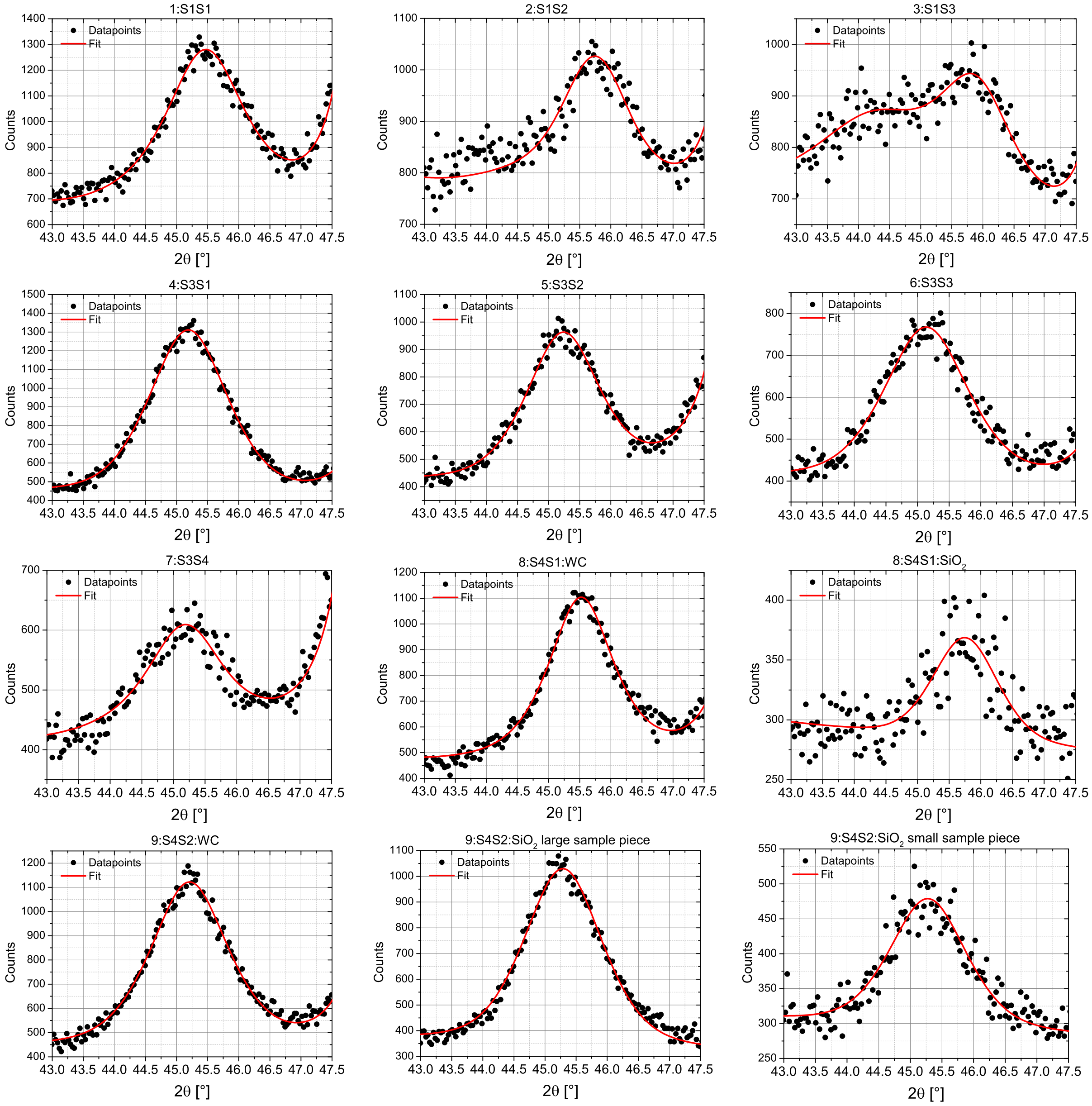

Figure B.1.: X-Ray diffractograms for all samples of series 1, 3 and 4 are shown together with the fit.

C. Structured DC sputtered Au contacts on pseudo-γ aluminum oxide films.

Shadowing masks were used to deposit 60 nm thick Au contacts about 3.12 mm × 1.80 mm in area, see Figure C.1a. They were used in combination with the spring contacting system, and both cross-plane and in-plane resistivity was measured at room temperature.

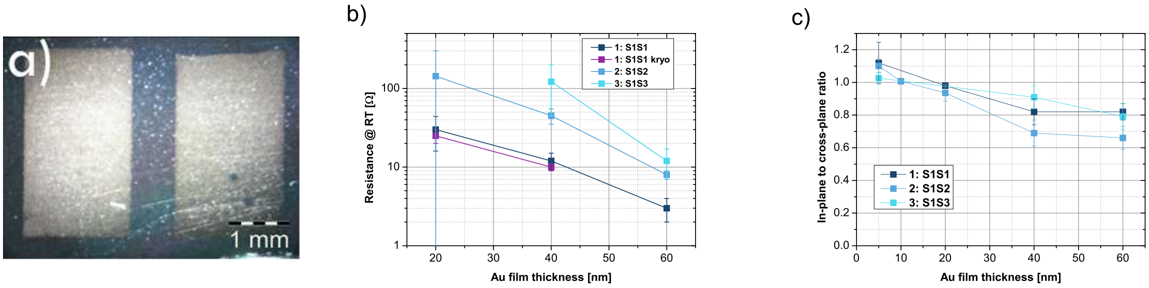

Figure C.1.: **a)** Light-microscopic image of DC sputtered Au contacts using a shadowing mask. **b)** Decrease of measured electrical resistance with increasing Au film thickness for samples of series 1. **c)** Decrease of in-plane to cross-plane resistance ratio with increasing Au film thickness for samples of series 1.

Figure C.1c shows dependence of resistance with increasing metalization layer. An increasing Au metalization reduces the in-plane resistance of the metalization, increasing the effective electrode area and thus decreasing the resistance. This is also seen in Figure C.1b (in-plane cross-plane ratio) for increasing thickness layer, a thicker metalization layer will carry a part of the current for in-plane measurements, thus reducing the resistance in comparison to addition of cross-plane resistances.

D. Formula derivation for thermopower measurement

The voltage measured for the whole sample is made up by contributions from the pseudo-γ aluminum oxide layer and the WC substrate

$$V_{Total} = V_{\mathrm{Al_2O_3}} + V_{WC} \tag{D.1}$$

where d is the layer thickness. The voltage is linked to the electric field E

$$V_{Total} = -E_{\mathrm{Al_2O_3}} \cdot d_{\mathrm{Al_2O_3}} - E_{WC} \cdot d_{WC}. \tag{D.2}$$

The electric field in equation D.2 is generated by the thermoelectric effect and can be expressed by the Seebeck coefficient and the temperature gradient across the film

$$V_{Total} = -S_{\mathrm{Al_2O_3}} \cdot \nabla T_{\mathrm{Al_2O_3}} \cdot d_{\mathrm{Al_2O_3}} - S_{WC} \cdot \nabla T_{WC} \cdot d_{WC} \tag{D.3}$$

In the steady state case, the termperature gradient ∇T is linear and can be expressed using the temperature difference ΔT

$$\nabla T_i = \frac{\Delta T_i}{d_i} \tag{D.4}$$

The temperature difference ΔT is applied across the whole sample, yielding a temperature difference across each material

$$\Delta T = \Delta T_{\mathrm{Al_2O_3}} + \Delta T_{WC} \tag{D.5}$$

The heat flux across the interface of the pseudo-γ aluminum oxide to the WC substrate has to be conserved

$$\lambda_{\mathrm{Al_2O_3}} \cdot \Delta T_{\mathrm{Al_2O_3}} = \lambda_{WC} \cdot \Delta T_{WC} \tag{D.6}$$

where λ is the thermal conductivity.
Using equations D.4, D.5 and D.6 it is possible to express the temperature difference across each film as a function of the total temperature difference, the thickness and thermal conductivity values of the films

$$\Delta T = \Delta T_{WC} \cdot \left(1 + \frac{d_{\mathrm{Al_2O_3}}}{d_{WC}} \frac{\lambda_{WC}}{\lambda_{\mathrm{Al_2O_3}}}\right) \tag{D.7}$$

$$\Delta T = \Delta T_{\mathrm{Al_2O_3}} \cdot \left(1 + \frac{d_{WC}}{d_{\mathrm{Al_2O_3}}} \frac{\lambda_{\mathrm{Al_2O_3}}}{\lambda_{WC}}\right) \tag{D.8}$$

Plugging equation D.7 into equation D.3

$$-V_{Total} = S_{\mathrm{Al_2O_3}} \cdot \frac{\Delta T}{1 + \frac{d_{WC}}{d_{\mathrm{Al_2O_3}}} \frac{\lambda_{\mathrm{Al_2O_3}}}{\lambda_{WC}}} + S_{WC} \cdot \frac{\Delta T}{1 + \frac{d_{\mathrm{Al_2O_3}}}{d_{WC}} \frac{\lambda_{WC}}{\lambda_{\mathrm{Al_2O_3}}}} \tag{D.9}$$

and solving for $S_{\mathrm{Al_2O_3}}$ yields

$$S_{\mathrm{Al_2O_3}} = -\frac{V_{Total}}{\Delta T} + \frac{\lambda_{\mathrm{Al_2O_3}}}{\lambda_{WC}} \frac{d_{WC}}{d_{\mathrm{Al_2O_3}}} (-\frac{V_{Total}}{\Delta T} - S_{WC}) \tag{D.10}$$

From the experimental results for the voltage and temperature difference, as well as the known values for the thicknesses and the Seebeck coefficient of WC, it is possible to estimate the order of magnitude for the two parts of the sum in equation D.10.
For the thermal conductivity of WC, Wang et al. report a value of 110 $\frac{\mathrm{W}}{\mathrm{m\,K}}$ [108]. The value of the thermal conductivity of pseudo-γ aluminum oxide is unknown, however, Su et al. report for γ aluminum oxide a value of 6 $\frac{\mathrm{W}}{\mathrm{m\,K}}$ [45]. Using these values, the order of magnitude can be estimated for both parts of the sum as

$$-\frac{V_{Total}}{\Delta T} \approx 10^{-6} \frac{V}{K} \tag{D.11}$$

$$\frac{\lambda_{\mathrm{Al_2O_3}}}{\lambda_{WC}} \frac{d_{WC}}{d_{\mathrm{Al_2O_3}}} (-\frac{V_{Total}}{\Delta T} - S_{WC}) \approx 10^{-3} \frac{V}{K} \tag{D.12}$$

This shows that the first part of the sum can be omitted and equation D.10 can be simplified to

$$S_{\mathrm{Al_2O_3}} \approx \frac{\lambda_{\mathrm{Al_2O_3}}}{\lambda_{WC}} \frac{d_{WC}}{d_{\mathrm{Al_2O_3}}} (-\frac{V_{Total}}{\Delta T} - S_{WC}) \tag{D.13}$$

Bibliography

[1] K. Bädeker. Über die elektrische Leitfähigkeit und die thermoelektrische Kraft einiger Schwermetallverbindungen. *Annalen der Physik*, 327(4):749–766, 1907. `doi:10.1002/andp.19073270409`.

[2] S. C. Dixon, D. O. Scanlon, C. J. Carmalt, and I. P. Parkin. N-Type doped transparent conducting binary oxides: An overview. *Journal of Materials Chemistry C*, 4(29):6946–6961, 2016. `doi:10.1039/c6tc01881e`.

[3] M. A. Aegerter and M. Menning. *Sol-Gel Technologies for Glass Producers and Users*. Springer, Boston, MA, 2004. `doi:10.1007/978-0-387-88953-5`.

[4] D. S. Ginley and C. Bright. Transparent Conducting Oxides. *MRS Bulletin*, 25(08):15–18, 2000. `doi:10.1557/mrs2000.256`.

[5] J. H. Yun, J. Kim, Y. C. Park, S. J. Moon, and W. A. Anderson. Double transparent conducting layers for Si photovoltaics. *Thin Solid Films*, 547:17–21, 2013. `doi:10.1016/j.tsf.2013.05.072`.

[6] T. Koida, H. Fujiwara, and M. Kondo. High-mobility hydrogen-doped In_2O_3 transparent conductive oxide for a-Si:H/c-Si heterojunction solar cells. *Solar Energy Materials and Solar Cells*, 93(6-7):851–854, 2009. `doi:10.1016/j.solmat.2008.09.047`.

[7] E. Fortunato, D. Ginley, H. Hosono, and D. C. Paine. Transparent Conducting Oxides for Photovoltaics. *MRS Bulletin*, 32(3):242–247, 2007. `doi:10.1557/mrs2007.29`.

[8] M. Grundmann. *The Physics of Semiconductors*. Springer Verlag, 2010. `doi:10.1007/978-3-319-23880-7`.

[9] P. F. Gerhardinger and R. J. McCurdy. Float Line Deposited Transparent Conductors - Implications for the PV Industry. In *Mat. Res. Soc. Symp. Proc.*, volume 426, pages 399–410, 1996. `doi:10.1557/PROC-426-399`.

[10] C. I. Bright. Review of Transparent Conductive Oxides (TCO). In D. M. Mattox and V. H. Mattox, editors, *50 Years of Vacuum Coating Technology and the Growth of the Society of Vacuum Coaters*, page 38. Society of Vacuum Coaters, 2007.

[11] B. Szyszka, W. Dewald, S. K. Gurram, A. Pflug, C. Schulz, M. Siemers, V. Sittinger, and S. Ulrich. Recent developments in the field of transparent conductive oxide films for spectral selective coatings, electronics and photovoltaics. In *Current Applied Physics*, volume 12, pages S2–S11, 2012. `doi:10.1016/j.cap.2012.07.022`.

[12] R. B. Laughlin. Optical absorption edge of SiO_2. *Physical Review B*, 22(6):3021–3029, 1980. `doi:10.1103/PhysRevB.22.3021`.

[13] Z. A. Weinberg, G. W. Rubloff, and E. Bassous. Transmission, photoconductivity, and the experimental band gap of thermally grown SiO_2 films. *Physical Review B*, 19(6):3107–3117, 1979. `doi:10.1103/PhysRevB.19.3107`.

[14] G. L. Tan, M. F. Lemon, D. J. Jones, and R. H. French. Optical properties and London dispersion interaction of amorphous and crystalline SiO_2 determined by vacuum ultraviolet spectroscopy and spectroscopic ellipsometry. *Physical Review B*, 72(20), 2005. `doi:10.1103/PhysRevB.72.205117`.

[15] L. Gupta, A. Mansingh, and P. K. Srivastava. Band gap narrowing and the band structure of tin-doped indium oxide films. *Thin Solid Films*, 176(1):33–44, 1989. `doi:10.1016/0040-6090(89)90361-1`.

[16] Y. Ohhata, F. Shinoki, and S. Yoshida. Optical properties of R.F. reactive sputtered tin-doped In_2O_3 films, 1979. `doi:10.1016/0040-6090(79)90298-0`.

[17] S. Ray, R. Banerjee, N. Basu, A. K. Batabyal, and A. K. Barua. Properties of tin doped indium oxide thin films prepared by magnetron sputtering. *Journal of Applied Physics*, 54(6):3497–3501, 1983. `doi:10.1063/1.332415`.

[18] R. H. French. Electronic Band Structure of Al_2O_3, with Comparison to AlON and AIN. *Journal of the American Ceramic Society*, 73(3):477–489, 1990. `doi:10.1111/j.1151-2916.1990.tb06541.x`.

[19] S. Miyazaki. Photoemission study of energy-band alignments and gap-state density distributions for high-k gate dielectrics. *Journal of Vacuum Science & Technology B: Microelectronics and Nanometer Structures*, 19(6):2212, 2001. `doi:10.1116/1.1418405`.

[20] E. O. Filatova and A. S. Konashuk. Interpretation of the Changing the Band Gap of Al_2O_3 Depending on Its Crystalline Form: Connection with Different Local Symmetries. *Journal of Physical Chemistry C*, 119(35):20755–20761, 2015. `doi:10.1021/acs.jpcc.5b06843`.

[21] B. Ealet, M. H. Elyakhloufi, E. Gillet, and M. Ricci. Electronic and crystallographic structure of γ-alumina thin films, 1994. `doi:10.1016/0040-6090(94)90171-6`.

[22] T. S. Moss. The Interpretation of the Properties of Indium Antimonide. *Proceedings of the Physical Society. Section B*, 67(10):775, 1954. `doi:10.1088/0370-1301/67/10/306`.

[23] E. Burstein. Anomalous optical absorption limit in InSb. *Physical Review*, 93(3):632–633, 1954. `doi:10.1103/PhysRev.93.632`.

[24] P. P. Edwards, A. Porch, M. O. Jones, D. V. Morgan, and R. M. Perks. Basic materials physics of transparent conducting oxides. *Dalton Transactions*, 19:2995, 2004. `doi:10.1039/b408864f`.

[25] C. Persson, U. Lindefelt, and B. E. Sernelius. Band gap narrowing in n-type and p-type 3C-, 2H-, 4H-, 6H-SiC, and Si. *Journal of Applied Physics*, 86(8):4419–4427, 1999. `doi:10.1063/1.371380`.

[26] U. Lindefelt. A model for doping-induced band gap narrowing in 3C-, 4H-, and 6H-SiC. *Materials Science and Engineering B*, 61-62(1998):225–228, 1999. `doi:10.1016/S0921-5107(98)00507-8`.

[27] H. A. McMaster. Conductive coating for glass and method of application, 1947. URL: `https://patentimages.storage.googleapis.com/4d/b3/67/af7fbfa321f08e/US2429420.pdf`.

[28] G. Rupprecht. Untersuchungen der elektrischen und lichtelektrischen Leitfähigkeit dünner Indiumoxydschichten. *Zeitschrift für Physik*, 139:504–517, 1954. `doi:10.1007/BF01374559`.

[29] H. Kawazoe, H. Yanagi, K. Ueda, and H. Hosono. Transparent p-type conducting oxides: design and fabrication of p-n heterojunctions. *MRS Bulletin*, 25(8):28–36, 2000. `doi:10.1557/mrs2000.148`.

[30] P. Gupta, T. Dutta, S. Mal, and J. Narayan. Controlled p-type to n-type conductivity transformation in NiO thin films by ultraviolet-laser irradiation. *Journal of Applied Physics*, 111(1), 2012. `doi:10.1063/1.3671412`.

[31] R. G. Gordon. Criteria for choosing transparent conductors. *MRS Bulletin*, 25(8):52–57, 2000. `doi:10.1557/mrs2000.151`.

[32] C. G. Granqvist and A. Hultåker. Transparent and conducting ITO films: new developments and applications. *Thin Solid Films*, 411(1):1–5, 2002. `doi:10.1016/S0040-6090(02)00163-3`.

[33] M. Lokanc, R. Eggert, and M. Redlinger. The Availability of Indium: The Present, Medium Term, and Long Term. *National Renewable Energy Laboratory*, October:1–90, 2015. URL: `https://www.nrel.gov/docs/fy16osti/62409.pdf`.

[34] A. C. Tolcin. Indium. *2011 Minerals Yearbook*, May:1–8, 2013. URL: `https://minerals.usgs.gov/minerals/pubs/commodity/indium/myb1-2011-indiu.pdf`.

[35] T. Minami. Present status of transparent conducting oxide thin-film development for Indium- Tin-Oxide (ITO) substitutes. *Thin Solid Films*, 516(17):5822–5828, 2008. `doi:10.1016/j.tsf.2007.10.063`.

[36] Z. Wu, Z. Chen, X. Du, J. M. Logan, J. Sippel, M. Nikolou, K. Kamaras, J. R. Reynolds, D. B. Tanner, A. F. Hebard, and A. G. Rinzler. Transparent, conductive carbon nanotube films. *Science*, 305(5688):1273–1276, 2004. `doi:10.1126/science.1101243`.

[37] Börse Frankfurt. Price development of aluminum in 2018. Accessed on 10th Aug 2018. URL: `http://www.boerse-frankfurt.de/rohstoffe/aluminiumpreis`.

[38] E. P. Gusev, M. Copel, E. Cartier, I. J. R. Baumvol, C. Krug, and M. A. Gribelyuk. High-resolution depth profiling in ultrathin Al_2O_3 films on Si. *Applied Physics Letters*, 76:176, 2000. `doi:10.1063/1.3587227`.

[39] S. Guha, E. Cartier, N. A. Bojarczuk, J. Bruley, L. Gignac, and J. Karasinski. High-quality aluminum oxide gate dielectrics by ultra-high-vacuum reactive atomic-beam deposition. *Journal of Applied Physics*, 90:512, 2001. `doi:10.1063/1.1361065`.

[40] I. Usov, P. Arendt, L. Stan, R. DePaula, H. Wang, S. Foltyn, and P. Dowden. Characteristics of alumina diffusion barrier films on Hastelloy. *Journal of Materials Research*, 19(4):1175–1180, 2004. `doi:10.1557/JMR.2004.0152`.

[41] J. Müller and D. Neuschütz. Efficiency of α-alumina as diffusion barrier between bond coat and bulk material of gas turbine blades. In *Vacuum*, volume 71, pages 247–251, 2003. `doi:10.1016/S0042-207X(02)00746-7`.

[42] M. Leskelä and M. Ritala. Atomic layer deposition (ALD): From precursors to thin film structures. In *Thin Solid Films*, volume 409, pages 138–146, 2002. `doi:10.1016/S0040-6090(02)00117-7`.

[43] A. Paranjpe, S. Gopinath, T. Omstead, and R. Bubber. Atomic Layer Deposition of AlO_x Thin Film Head Gap Applications. *Journal of The Electrochemical Society*, 148(9):G465, 2001. `doi:10.1149/1.1385822`.

[44] D. Ha, D. Shin, G. H. Koh, J. Lee, S. Lee, Y. S. Ahn, H. Jeong, T. Chung, and K. Kim. A cost effective embedded DRAM integration for high density memory and high performance logic using 0.15 μm technology node and beyond. *IEEE Transactions on Electron Devices*, 47(7):1499–1506, 2000. `doi:10.1109/16.848299`.

[45] Y. J. Su, H. Wang, W. D. Porter, A. R.De A. Lopez, and K. T. Faber. Thermal conductivity and phase evolution of plasma-sprayed multilayer coatings. *Journal of Materials Science*, 36(14):3511–3518, 2001. `doi:10.1023/A:1017932617123`.

[46] M. Kawate, A. K. Hashimoto, and T. Suzuki. Oxidation resistance of $Cr_{1-x}Al_xN$ and $Ti_{1-x}Al_xN$ films. *Surface and Coatings Technology*, 165(2):163–167, 2003. `doi:10.1016/S0257-8972(02)00473-5`.

[47] Y. Gao, X. Xu, Z. Yan, and G. Xin. High hardness alumina coatings prepared by low power plasma spraying. *Surface and Coatings Technology*, 154(2-3):189–193, 2002. `doi:10.1016/S0257-8972(01)01711-X`.

[48] O. Zywitzki and G Hoetzsch. Influence of coating parameters on the structure and properties of Al_2O_3 layers reactively deposited by means of pulsed magnetron sputtering. *Surface and Coatings Technology*, 86-87(PART 2):640–647, 1996. `doi:10.1016/S0257-8972(96)02992-1`.

[49] R. S Zhou and R. L. Snyder. Structures and transformation mechanisms of the η, γ and θ transition aluminas. *Acta Crystallographica Section B*, 47(5):617–630, 1991. `doi:10.1107/S0108768191002719`.

[50] K. Wefers and C. Misra. Oxides and Hydroxides of Aluminum. *Alcoa Technical Paper*, 19:1–100, 1987. URL: `http://epsc511.wustl.edu/Aluminum_Oxides_Alcoa1987.pdf`.

[51] R. E. Newnham and Y. M. de Haan. Refinement of the α Al_2O_3, Ti_2O_3, V_2O_3 and Cr_2O_3 structures. *Zeitschrift für Kristallographie*, 117(2-3):235–237, 1962. `doi:10.1524/zkri.1962.117.2-3.235`.

[52] F. Haber. Über die Hydroxyde des Aluminiums und des dreiwertigen Eisens. *Die Naturwissenschaften*, 13(49-50):1007–1012, 1925. `doi:10.1007/BF01559270`.

[53] N. Ishizawa, T. Miyata, I. Minato, F. Marumo, and S. Iwai. A structural investigation of α-Al_2O_3 at 2170 K. *Acta Crystallographica Section B Structural Crystallography and Crystal Chemistry*, 36(2):228–230, feb 1980. `doi:10.1107/S0567740880002981`.

[54] A. Khanna and D. G. Bhat. Nanocrystalline gamma alumina coatings by inverted cylindrical magnetron sputtering. *Surface and Coatings Technology*, 201(1-2):168–173, 2006. `doi:10.1016/j.surfcoat.2005.11.109`.

[55] M.-H. Lee, C.-F. Cheng, V. Heine, and J. Klinowski. Distribution of tetrahedral and octahedral Al sites in gamma alumina. *Chemical Physics Letters*, 265(6):673–676, 1997. `doi:10.1016/S0009-2614(96)01492-3`.

[56] W. Engelhart, W. Dreher, O. Eibl, and V. Schier. Deposition of alumina thin film by dual magnetron sputtering: Is it γ-Al_2O_3? *Acta Materialia*, 59(20):7757–7767, 2011. `doi:10.1016/j.actamat.2011.08.048`.

[57] H. P. Pinto, R. M. Nieminen, and S. D. Elliott. Ab initio study of γ-Al_2O_3 surfaces. *Physical Review B*, 70(12):125402, 2004. `doi:10.1103/PhysRevB.70.125402`.

[58] R. Dupree, M. H. Lewis, and M. E. Smith. A study of the vacancy distribution in non-stoichiometric spinels by magic-angle spinning NMR. *Philosophical Magazine A: Physics of Condensed Matter, Structure, Defects and Mechanical Properties*, 53(2):195–L20, 1986. `doi:10.1080/01418618608242816`.

[59] N. Peranio, M. Winkler, M. Dürrschnabel, J. König, and O. Eibl. Assessing antisite defect and impurity concentrations in Bi_2Te_3 based thin films by high-accuracy chemical analysis. *Advanced Functional Materials*, 23(39):4969–4976, 2013. `doi:10.1002/adfm.201300606`.

[60] A. K. N. Kumar, S. Prasanna, B. Subramanian, S. Jayakumar, and G. M. Rao. A transmission electron microscopy and X-ray photoelectron spectroscopy study of annealing induced γ-phase nucleation, clustering, and interfacial dynamics in reactively sputtered amorphous alumina thin films. *Journal of Applied Physics*, 117(12):125307–25302, 2015. `doi:10.1063/1.4916331`.

[61] M. Sridharan, M. Sillassen, J. Bøttiger, J. Chevallier, and H. Birkedal. Pulsed DC magnetron sputtered Al_2O_3 films and their hardness. *Surface and Coatings Technology*, 202(4):920–924, 2007. `doi:10.1016/j.surfcoat.2007.05.061`.

[62] R. Cremer, M. Witthaut, D. Neuschütz, G. Erkens, T. Leyendecker, and M. Feldhege. Comparative characterization of alumina coatings deposited by RF, DC and pulsed reactive magnetron sputtering. In *Surface and Coatings Technology*, volume 120-121, pages 213–218, 1999. `doi:10.1016/S0257-8972(99)00458-2`.

[63] P. J. J. Kelly and R. D. D. Arnell. Magnetron sputtering: a review of recent developments and applications. *Vacuum*, 56:159–172, 2000. `doi:10.1016/S0042-207X(99)00189-X`.

[64] W. Engelhart. *Metalloxid-Dünnfilme als Verschleißschutzschichten: Abscheidung , Nanohärte und Mikro- / Nanostruktur*. PhD thesis, Universität Tübingen, 2011.

[65] H. Holleck, M. Lahres, and P. Woll. Multilayer coatings-influence of fabrication parameters on constitution and properties. *Surface and Coatings Technology*, 41(2):179–190, 1990. `doi:10.1016/0257-8972(90)90166-A`.

[66] J. Luo, Y. Meng, T. Shao, and Q. Zhao. *Advanced Tribology*. Springer, Berlin, Heidelberg, 2010. `doi:10.1007/978-3-642-03653-8`.

[67] V. Kouznetsov, K. Macák, J. M. Schneider, U. Helmersson, and I. Petrov. A novel pulsed magnetron sputter technique utilizing very high target power densities. *Surface and Coatings Technology*, 122(2-3):290–293, 1999. `doi:10.1016/S0257-8972(99)00292-3`.

[68] A. P. Ehiasarian, W. D. Münz, L. Hultman, U. Helmersson, and I. Petrov. High power pulsed magnetron sputtered CrN_x films. *Surface & Coatings Technology*, 163-164:267–272, 2003. `doi:10.1016/S0257-8972(02)00479-6`.

[69] J. Goldstein, D. Newbury, D. Joy, C. Lyman, P. Echlin, E. Lifshin, L. Sawyer, and J. Michael. *Scanning Electron Microscopy and X-Ray Microanalysis*. Springer Science+Business Media, third edit edition, 2013. `doi:10.1017/CBO9781107415324.004`.

[70] L. Reimer. *Scanning Electron Microscopy*, volume 45. Springer Verlag, Berlin Heidelberg, second edition, 1998. `doi:10.1002/sca.4950170309`.

[71] W. C. Röntgen. Über eine neue Art von Strahlen. *Annalen der Physik*, 300(1):12–17, 1895. `doi:10.1002/andp.18983000103`.

[72] G. Benner and W. Probst. Köhler illumination in the TEM: fundamentals and advantages. *Journal of Microscopy*, 174(3):133–142, 1994. `doi:10.1111/j.1365-2818.1994.tb03461.x`.

[73] N. Peranio and O. Eibl. Quantitative EDX microanalysis of Bi_2Te_3 in the TEM. *Physica Status Solidi (A) Applications and Materials Science*, 204(10):3243–3255, 2007. `doi:10.1002/pssa.200622579`.

[74] Oxford Instruments. INCA Operator Manual, 2006. URL: `https://investigacion.us.es/docs/web/files/manual_instrucciones_eds_inca.pdf`.

[75] W. Probst, G. Benner, J. Bihr, and E. Weimer. An "Omega" Energy Filtering TEM - Principles and Applications. *Advanced Materials*, 5(4):297–300, 1993. `doi:10.1002/adma.19930050417`.

[76] J. Hillier and R. F. Baker. Microanalysis by Means of Electrons. *Journal of Applied Physics 1*, 15:5861, 1944. `doi:10.1063/1.1656079`.

[77] R. F. Egerton. Electron energy-loss spectroscopy in the TEM. *Reports on Progress in Physics*, 72(1), 2009. `doi:10.1088/0034-4885/72/1/016502`.

[78] W. Grogger, M. Varela, R. Ristau, B. Schaffer, F. Hofer, and K. M. Krishnan. Energy-filtering transmission electron microscopy on the nanometer length scale. *Journal of Electron Spectroscopy and Related Phenomena*, 143(2-3 SPEC. ISS.):139–147, 2005. `doi:10.1016/j.elspec.2004.09.028`.

[79] J. M. Zuo, J. Pacaud, R. Hoier, and J. C. H. Spence. Experimental measurement of electron diffuse scattering in magnetite using energy-filter and imaging plates. *Micron*, 31:527–532, 2000. URL: `www.elsevier.com/locate/micron`, `doi:10.1016/S0968-4328(99)00133-X`.

[80] D. B. Williams and C. B. Carter. *Transmission Electron Microscopy: A Textbook for Materials Science*, volume V1-V4. Humana Press, Totowa, NJ, 2009. `doi:10.1007/978-1-61779-415-5_23`.

[81] W. H. Bragg and W. L. Bragg. The Reflection of X-rays by Crystals. *Proceedings of the Royal Society A: Mathematical, Physical and Engineering Sciences*, 88(605):428–438, jul 1913. `doi:10.1098/rspa.1913.0040`.

[82] G. Cliff and G. W. Lorimer. The quantitative analysis of thin specimens. *Journal of Microscopy*, 103(2):203–207, 1975. `doi:10.3109/10520295809111862`.

[83] J. E. Wood, D. B. Williams, and J. I. Goldstein. Experimental and theoretical determination of k_{AFe} factors for quantitative X-ray microanalysis in the analytical electron microscope. *Journal of Microscopy*, 133(3):255–274, 1984. `doi:10.1111/j.1365-2818.1984.tb00490.x`.

[84] G. Zschornack. *Hadbook of X-ray Data*. Springer-Verlag Berlin Heidelberg, 2007. `doi:10.1007/978-3-540-28619-6`.

[85] P. Kumar, M. Pfeffer, E. Schweda, O. Eibl, and J. Qiu. PbSe mid-IR photoconductive thin films (part I): Phase analysis of the functional layer. *Journal of Alloys and Compounds*, 724:316–326, nov 2017. `doi:10.1016/j.jallcom.2017.06.330`.

[86] L. A. Grunes, R. D. Leapman, C. N. Wilker, R. Hoffmann, and A. B. Kunz. Oxygen K near-edge fine structure: An electron-energy-loss investigation with comparisons to new theory for selected 3d transition-metal oxides. *Physical Review B*, 25(12):7157–7173, 1982. `doi:10.1103/PhysRevB.25.7157`.

[87] P. L. Hansen, R. Brydson, D. W. McComb, and I. Richardson. EELS fingerprint of Al-coordination in silicates. *Microscopy Microanalysis Microstructures*, 5(3):173–182, 1994. `doi:10.1051/mmm:0199400503017300`.

[88] T. M. Chou and M. Libera. Mean free paths for inelastic electron scattering in silicon and poly(styrene) nanospheres. *Ultramicroscopy*, 94(1):31–35, 2003. `doi:10.1016/S0304-3991(02)00192-4`.

[89] W. C. Oliver and G. M. Pharr. An improved technique for determining hardness and elastic modulus using load and displacement sensing indentation experiments. *Journal of Materials Research*, 7(6):1564–1583, jun 1992. `doi:10.1557/JMR.1992.1564`.

[90] W. C. Oliver and G. M. Pharr. Measurement of hardness and elastic modulus by instrumented indentation: Advances in understanding and refinements to methodology. *Journal of Materials Research*, 19(01):3–20, jan 2004. `doi:10.1557/jmr.2004.19.1.3`.

[91] S. N. Rashkeev, K. Sohlberg, M. V. Glazoff, J. Novak, S. J. Pennycook, and S. T. Pantelides. Transition metal atoms on different alumina phases: The role of subsurface sites on catalytic activity. *Physical Review B*, 67(11):115414, 2003. `doi:10.1103/PhysRevB.67.115414`.

[92] Z. Aabdin, N. Peranio, and O. Eibl. Switching of the natural nanostructure in Bi_2Te_3 materials by ion irradiation. *Advanced Materials*, 24(34):4605–4608, 2012. `doi:10.1002/adma.201201079`.

[93] M. Tyagi, M. Tomar, and V. Gupta. Postdeposition annealing of NiO_x thin films: A transition from n-type to p-type conductivity for short wave length optoelectronic devices. *Journal of Materials Research*, 28(5):723–732, 2013. `doi:10.1557/jmr.2012.443`.

[94] X. Pang, L. Shi, P. Wang, G. Zhang, and W. Liu. Influences of bias voltage on mechanical and tribological properties of Ti-Al-C films synthesized by magnetron sputtering. *Surface and Coatings Technology*, 203(10-11):1537–1543, 2009. `doi:10.1016/j.surfcoat.2008.12.003`.

[95] Z. T. Yang, B. Yang, L. P. Guo, and D. J. Fu. Effect of bias voltage on the structure and hardness of Ti-Si-N composite coatings synthesized by cathodic arc assisted middle-frequency magnetron sputtering. *Journal of Alloys and Compounds*, 473(1-2):437–441, 2009. `doi:10.1016/j.jallcom.2008.06.003`.

[96] A. Stadler. Transparent Conducting Oxides – An Up-To-Date Overview. *Materials*, 5(12):661–683, 2012. `doi:10.3390/ma5040661`.

[97] H. Liu, V. Avrutin, N. Izyumskaya, Ü. Özgr, and H. Morkoç. Transparent conducting oxides for electrode applications in light emitting and absorbing devices. *Superlattices and Microstructures*, 48:458–484, 2010. `doi:10.1016/j.spmi.2010.08.011`.

[98] M. Grundmann, A. Rahm, and H. von Wenckstern. Transparent Conductive Oxides. *Physica Status Solidi (A) Applications and Materials Science*, 212(7):1408, 2015. `doi:10.1002/pssa.201570449`.

[99] B. G. Lewis and D. C. Paine. Applications and Processing of Transparent Conducting Oxides. *MRS Bulletin*, 25(08):22–27, 2000. `doi:10.1557/mrs2000.147`.

[100] V Edlmayr, M Moser, C Walter, and C Mitterer. Thermal stability of sputtered Al_2O_3 coatings. *Surface and Coatings Technology*, 204(9-10):1576–1581, 2010. `doi:10.1016/j.surfcoat.2009.10.002`.

[101] D. A. G. Bruggeman. Berechnung verschiedener physikalischer Konstanten von heterogenen Substanzen. I. Dielektrizitätskonstanten und Leitfähigkeiten der Mischkörper aus isotropen Substanzen. *Annalen der Physik*, 421(2):160–178, 1937. `doi:10.1002/andp.19374210205`.

[102] Y. C. Liu, J. H. Hsieh, and S. K. Tung. Extraction of optical constants of zinc oxide thin films by ellipsometry with various models. *Thin Solid Films*, 510(1-2):32–38, 2006. `doi:10.1016/j.tsf.2005.10.089`.

[103] J. Houska, J. Blazek, J. Rezek, and S. Proksova. Overview of optical properties of Al_2O_3 films prepared by various techniques. *Thin Solid Films*, 520(16):5405–5408, 2012. `doi:10.1016/j.tsf.2012.03.113`.

[104] R. A. A. Synowicki. Spectroscopic ellipsometry characterization of indium tin oxide film microstructure and optical constants. *Thin Solid Films*, 313âĂŞ314:394–397, 1998. `doi:http://dx.doi.org/10.1016/S0040-6090(97)00853-5`.

[105] H. El Rhaleb, E. Benamar, M. Rami, J. P. Roger, A. Hakam, and A. Ennaoui. Spectroscopic ellipsometry studies of index profile of indium tin oxide films prepared by spray pyrolysis. *Applied Surface Science*, 201(1-4):138–145, 2002. `doi:10.1016/S0169-4332(02)00656-6`.

[106] T. Gerfin and M. Grätzel. Optical properties of tin-doped indium oxide determined by spectroscopic ellipsometry. *Journal Of Applied Physics*, 79(3):1722, 1996. `doi:10.1063/1.360960`.

[107] N. W. M. Ritchie. Spectrum Simulation in DTSA-II. *Microscopy and Microanalysis*, 15(5):454–468, 2009. `doi:10.1017/S1431927609990407`.

[108] H. Wang, T. Webb, and J. W. Bitler. Study of thermal expansion and thermal conductivity of cemented WC-Co composite. *International Journal of Refractory Metals and Hard Materials*, 49(1):170–177, 2015. `doi:10.1016/j.ijrmhm.2014.06.009`.

[109] D. M. Mattox. Influence of Oxygen on the Adherence of Gold Films to Oxide Substrates. *Journal of Applied Physics*, 37(9):3613–3615, 1966. `doi:10.1116/1.1492648`.

[110] D. M. Mattox. Thin Film Metallization of Oxides in Microeletronics. *Thin Solid Films*, 18:173–186, 1973. `doi:10.1016/0040-6090(73)90096-5`.

[111] L. Zhang, R. Persaud, and T. E. Madey. Ultrathin metal lms on a metal oxide surface: Growth of Au on TiO_2 (110). *Physical Review B*, 56(16):549–557, 1997. `doi:10.1103/PhysRevB.56.10549`.

[112] M. Voigt and M. Sokolowski. Electrical properties of thin rf sputtered aluminum oxide films. *Materials Science and Engineering: B*, 109(1-3):99–103, 2004. `doi:10.1016/j.mseb.2003.10.056`.

[113] J. Kolodzey, E. A. Chowdhury, T. N. Adam, G. Qui, I. Rau, J. O. Olowolafe, J. S. Suehle, and Y. Chen. Electrical conduction and dielectric breakdown in aluminum oxide insulators on silicon. *IEEE Transactions on Electron Devices*, 47(1):121–128, 2000. `doi:10.1109/16.817577`.

[114] D. Liu and J. Robertson. Oxygen vacancy levels and interfaces of Al_2O_3. *Microelectronic Engineering*, 86(7-9):1668–1671, 2009. `doi:10.1016/j.mee.2009.03.011`.

[115] V. V. Afanas'Ev and A. Stesmans. Internal photoemission at interfaces of high- κ insulators with semiconductors and metals. *Journal of Applied Physics*, 102(8):81301–1785, 2007. `doi:10.1063/1.2799091`.

[116] M. Orita, H. Ohta, M. Hirano, S. Narushima, and H. Hosono. Amorphous transparent conductive oxide $InGaO_3(ZnO)_m$ ($m \leq 4$): a Zn 4s conductor. *Philosophical Magazine Part B*, 81(5):501–515, 2001. `doi:10.1080/13642810110045923`.

[117] D. D. Edwards, T. O. Mason, F. Goutenoire, and K. R. Poeppelmeier. A new transparent conducting oxide in the Ga_2O_3 - In_2O_3-SnO_2 system. *Applied Physics Letters*, 70(13):1706–13504, 1997. `doi:10.1063/1.3499306`.

[118] K. Nomura, H. Ohta, A. Takagi, T. Kamiya, M. Hirano, and H. Hosono. Room-temperature fabrication of transparent flexible thin-film transistors using amorphous oxide semiconductors. *Nature*, 432(7016):488–492, 2004. `doi:10.1038/nature03090`.

[119] Z. Q. Li and J. J. Lin. Electrical resistivities and thermopowers of transparent Sn-doped indium oxide films. *Journal of Applied Physics*, 96(10):5918–5920, 2004. `doi:10.1063/1.1801153`.

[120] H. Kawazoe, M. Yasukawa, H. Hyodo, M. Kurita, H. Yanagi, and H. Hosono. P-type electrical conduction in transparent thin films of $CuAlO_2$. *Nature*, 389(6654):939–942, 1997. `doi:10.1038/40087`.

[121] K. Bobzin. High-performance coatings for cutting tools. *CIRP Journal of Manufacturing Science and Technology*, 18(2017):1–9, aug 2017. `doi:10.1016/j.cirpj.2016.11.004`.

[122] A. Michalski and D. Siemiaszko. Nanocrystalline cemented carbides sintered by the pulse plasma method. *International Journal of Refractory Metals and Hard Materials*, 25(2):153–158, 2007. `doi:10.1016/j.ijrmhm.2006.03.007`.

[123] Z. Fang and J. W. Eason. Study of nanostructured WC-Co composites. *International Journal of Refractory Metals and Hard Materials*, 13(5):297–303, 1995. `doi:10.1016/0263-4368(95)92675-A`.

[124] H. C. Kim, I. K. Jeong, I. Ji. Shon, I. Y. Ko, and J. M. Doh. Fabrication of WC-8 wt.%Co hard materials by two rapid sintering processes. *International Journal of Refractory Metals and Hard Materials*, 25(4):336–340, 2007. `doi:10.1016/j.ijrmhm.2006.09.001`.

[125] Z. Z. Fang, X. Wang, T. Ryu, K. S. Hwang, and H. Y. Sohn. Synthesis, sintering, and mechanical properties of nanocrystalline cemented tungsten carbide - A review. *International Journal of Refractory Metals and Hard Materials*, 27(2):288–299, 2009. `doi:10.1016/j.ijrmhm.2008.07.011`.

[126] S. A. Humphry-Baker and W. E. Lee. Tungsten carbide is more oxidation resistant than tungsten when processed to full density. *Scripta Materialia*, 116:67–70, 2016. `doi:10.1016/j.scriptamat.2016.01.007`.

[127] S. A. Humphry-Baker, K. Peng, and W. E. Lee. Oxidation resistant tungsten carbide hardmetals. *International Journal of Refractory Metals and Hard Materials*, 66:135–143, aug 2017. `doi:10.1016/j.ijrmhm.2017.03.009`.

[128] B. Casas, X. Ramis, M. Anglada, J. M. Salla, and L. Llanes. Oxidation-induced strength degradation of WC-Co hardmetals. In *International Journal of Refractory Metals and Hard Materials*, volume 19, pages 303–309, 2001. `doi:10.1016/S0263-4368(01)00033-6`.

[129] W. Acchar, U. U. Gomes, W. A. Kaysser, and J. Goring. Strength degradation of a tungsten carbide-cobalt composite at elevated temperatures. *Materials Characterization*, 43(1):27–32, 1999. `doi:10.1016/S1044-5803(98)00056-4`.

[130] P. Kindermann, P. Schlund, H. G. Sockel, M. Herr, W. Heinrich, K. Görting, and U. Schleinkofer. High-temperature fatigue of cemented carbides under cyclic loads. *International Journal of Refractory Metals and Hard Materials*, 17(1):55–68, 1999. `doi:10.1016/S0263-4368(99)00014-1`.

[131] S. PalDey and S. C. Deevi. Single layer and multilayer wear resistant coatings of (Ti,Al)N: a review. *Materials Science and Engineering A*, 342:58–79, 2003. `doi:10.1016/S0921-5093(02)00259-9`.

[132] J. G. Han, J. S. Yoon, H. J. Kim, and K. Song. High temperature wear resistance of (TiAl)N films synthesized by cathodic arc plasma deposition. *Surface and Coatings Technology*, 8687:82–87, 1996. `doi:10.1016/S0257-8972(96)02964-7`.

[133] U. Helmersson, S. Todorova, S. A. Barnett, J.-E. Sundgren, L. C. Markert, and J. E. Greene. Growth of single-crystal TiN/VN strained-layer superlattices with extremely high mechanical hardness. *Journal of Applied Physics*, 62:481, 1987. `doi:10.1116/1.578030`.

[134] H. Holleck. Material selection for hard coatings. *Journal of Vacuum Science & Technology A*, 4:2661, 1986. `doi:10.1116/1.581977`.

[135] J.-E. Sundgren. Structure and properties of TiN coatings. *Thin Solid Films*, 128(1):21–44, 1985. `doi:10.1016/0040-6090(85)90333-5`.

[136] D. G. Cahill, S.-M. Lee, and T. I. Selinder. Thermal conductivity of κ Al_2O_3 and α Al_2O_3 wear-resistant coatings. *Journal of Applied Physics*, 83:5783, 1998. `doi:10.1063/1.367500`.

[137] X. Liu, C. Johnson, C. Li, J. Xu, and C. Cross. Developing TiAlN coatings for intermediate temperature solid oxide fuel cell interconnect applications. *International Journal of Hydrogen Energy*, 33(1):189–196, 2008. `doi:10.1016/j.ijhydene.2007.09.007`.

[138] C. Subramanian and K. N. Strafford. Review of multicomponent and multilayer coatings for tribological applications. *Wear*, 165:85–95, 1993. `doi:10.1016/0043-1648(93)90376-W`.

[139] COMSOL Multiphysics 4.3a. URL: `https://www.comsol.com/`.

[140] H. O. Pierson. Fundamentals of Chemical Vapor Deposition. In *Handbook of chemical vapor deposition (CVD): Principles, Technology and Applications*, chapter 2, pages 36–67. William Andrew Publishing, second edition, 1999. `doi:10.1016/B978-081551432-9.50006-1`.

[141] J. H. Werner. Origin of Curved Arrhenius Plots for the Conductivity of Polycrystalline Semiconductors. *Solid State Phenomena*, 37-38:213–218, 1994. `doi:10.4028/www.scientific.net/SSP.37-38.213`.

[142] Y. Kajikawa. Conduction model covering non-degenerate through degenerate polycrystalline semiconductors with non-uniform grain-boundary potential heights based on an energy filtering model. *Journal of Applied Physics*, 112(12), 2012. `doi:10.1063/1.4770452`.

[143] J. Ederth, P. Johnsson, G. A. Niklasson, A. Hoel, A. Hultåker, P. Heszler, C. G. Granqvist, A. R. van Doorn, M. J. Jongerius, and D. Burgard. Electrical and optical properties of thin films consisting of tin-doped indium oxide nanoparticles. *Physical Review B*, 68(15):155410, 2003. `doi:10.1103/PhysRevB.68.155410`.

[144] Ping Sheng. Fluctuation-induced tunneling conduction in disordered materials. *Physical Review B*, 21(6):2180–2195, 1980. `arXiv:arXiv:1011.1669v3`, `doi:10.1103/PhysRevB.21.2180`.

[145] R. Rachbauer, J. J. Gengler, A. A. Voevodin, K. Resch, and P. H. Mayrhofer. Temperature driven evolution of thermal, electrical, and optical properties of Ti-Al-N coatings. *Acta Materialia*, 60(5):2091–2096, 2012. `doi:10.1016/j.actamat.2012.01.005`.

[146] J. Wang, W. L. Wang, P. D. Ding, Y. X. Yang, L. Fang, J. Esteve, M. C. Polo, and G. Sanchez. Synthesis of cubic aluminum nitride by carbothermal nitridation reaction. *Diamond and Related Materials*, 8(7):1342–1344, 1999. `doi:10.1016/S0925-9635(99)00134-X`.

[147] Y. Igasaki, H. Mitsuhashi, K. Azuma, and T. Moto. Structure and Electrical Properties of Titanium Nitride Films. *Japanese Journal of Applied Physics*, 17(1):85, 1978. `doi:10.1143/JJAP.17.85`.

[148] M.-H. Park and S.-H. Kim. Temperature coefficient of resistivity of TiAlN films deposited by radio frequency magnetron sputtering. *Transactions of Nonferrous Metals Society of China*, 23(2):433–438, 2013. `doi:10.1016/S1003-6326(13)62481-4`.

[149] J.-J. Lin and Z.-Q. Li. Electronic conduction properties of indium tin oxide: single-particle and many-body transport. *Journal of Physics: Condensed Matter*, 26, 2014. `doi:10.1088/0953-8984/26/34/343201`.

[150] J. A. Marley and R. C. Dockerty. Electrical properties of stannic oxide single crystals. *Physical Review*, 140(1A), 1965. `doi:10.1103/PhysRev.140.A304`.

[151] R. K. Gupta, K. Ghosh, R. Patel, and P. K. Kahol. Effect of thickness on optoelectrical properties of Mo-doped indium oxide films. *Applied Surface Science*, 255(5 PART 2):3046–3048, 2008. `doi:10.1016/j.apsusc.2008.08.077`.

[152] P. S. Raghupati, J. Gerorge, and C. S. Menon. The effect of deposition rate on electrical , optical and structural properties of tin-doped indium oxide (ITO) films. *E -Journal of Chemistry*, 2(3):171–177, 2005. `doi:10.1016/j.physb.2005.11.159`.

[153] H. Hosono, H. Ohta, M. Orita, K. Ueda, and M. Hirano. Frontier of transparent conductive oxide thin films. *Vacuum*, 66(3-4):419–425, 2002. `doi:10.1016/S0042-207X(02)00165-3`.

[154] R. Kumar and N. Khare. Temperature dependence of conduction mechanism of ZnO and Co-doped ZnO thin films. *Thin Solid Films*, 516(6):1302–1307, 2008. `doi:10.1016/j.tsf.2007.06.121`.

[155] N. Martin, A. Besnard, F. Sthal, F. Vaz, and C. Nouveau. The contribution of grain boundary barriers to the electrical conductivity of titanium oxide thin films. *Appl.Phys. Lett.*, 93, 2008. `doi:10.1063/1.356306`.

[156] Naoyuki Ueda, Takahisa Omata, Naoko Hikuma, Kazushige Ueda, Hiroshi Mizoguchi, Takuya Hashimoto, and Hiroshi Kawazoe. New oxide phase with wide band gap and high electroconductivity, $MgIn_2O_4$. *Applied Physics Letters*, 61(16):1954–1955, 1992. `doi:10.1063/1.108374`.

[157] A. P. Roth and D. F. Williams. Properties of zinc oxide films prepared by the oxidation of diethyl zinc. *Journal of Applied Physics*, 52(11):6685–6692, 1981. `doi:10.1063/1.328618`.

[158] M. Regragui, V. Jousseaume, M. Addou, A. Outzourhit, J. C. Bernède, and B. El Idrissi. Electrical and optical properties of WO_3 thin films. *Thin Solid Films*, 397(1-2):238–243, 2001. `doi:10.1016/S0040-6090(01)01405-5`.

[159] B. C. Lippens and J. H. de Boer. Study of phase transformations during calcination of aluminum hydroxides by selected area electron diffraction. *Acta Crystallographica*, 17(10):1312–1321, 1964. `doi:10.1107/S0365110X64003267`.

[160] C. S. John, N. C. M. Alma, and G. R. Hays. Characterization of transitional alumina by solid-state magic angle spinning aluminium NMR. *Applied Catalysis*, 6(3):341–346, 1983. `doi:10.1016/0166-9834(83)80106-7`.

[161] G. Zhou, L. Wang, X. Wang, and Y. Yu. Deposition of nanostructured crystalline alumina thin film by twin targets reactive high power impulse magnetron sputtering. *Applied Surface Science*, 455:310–317, oct 2018. `doi:10.1016/j.apsusc.2018.05.153`.

[162] V. D. Tkachev, A. V. Mudryi, and N. S. Minaev. Noble Gas Atoms as Chemical Impurities in Silicon. *Phys stat sol (a)*, 81:313, 1984. `doi:10.1002/pssa.2210810135`.

[163] V. D. Tkachev, A. M. Zaitsev, and V. V. Tkachev. Chemical Activity of Noble Gases in Diamond. *Phys stat sol (b)*, 129:129–133, 1985. `doi:10.1002/pssb.2221290112`.

[164] S. G. Gagarin, A. V. Mudryi, A. L. Pushkarchuk, A. G. Ulyashin, and Y. A. Teterin. Theoretical Analysis of the Chemical Activivity of Noble Gas Atoms in Silicon. *Phys stat sol (b)*, 499:499–503, 1986. `doi:10.1002/pssb.2221330208`.

[165] D. M. Wood, A. Zunger, and R. De Groot. Electronic structure of filled tetrahedral semiconductors. *Physical Review B*, 31(4):2570–2573, 1985. `doi:10.1103/PhysRevB.31.2570`.

[166] S. K. Estreicher, J. Weber, A. Derecskei-Kovacs, and D. S. Marynick. Noble-gas-related defects in Si and the origin of the 1018 meV photoluminescence line. *Physical Review B*, 55(8):5037–5044, 1997. `doi:10.1103/PhysRevB.55.5037`.

[167] A. V. Mudryi, A. L. Pushkarchuk, and A. G. Ulyashin. Noble Gas Atoms in Si: Energy Spectrum Distortion of Vacancy Complexes. *Phys stat sol (b)*, 129:K83, 1985. `doi:10.1002/pssb.2221290166`.

[168] L. Pizzagalli, A. Charaf-Eddin, and S. Brochard. Numerical simulations and modeling of the stability of noble gas atoms in interaction with vacancies in silicon. *Computational Materials Science*, 95:149–158, 2014. `doi:10.1016/j.commatsci.2014.07.011`.

[169] A. Charaf Eddin and L Pizzagalli. First principles calculation of noble gas atoms properties in 3C-SiC. *Journal of Nuclear Materials*, 429(1-3):329–334, 2012. `doi:10.1016/j.jnucmat.2012.06.022`.

[170] I. Stará, D. Zeze, V. Matolín, J. Pavluch, and B. Gruzza. AES and EELS study of alumina model catalyst supports. *Applied Surface Science*, 115(1):46–52, 1997. `doi:10.1016/S0169-4332(96)00582-X`.

[171] R. H. French, H. Müllejans, and D. J. Jones. Optical Properties of Aluminum Oxide: Determined from Vacuum Ultraviolet and Electron Energy-Loss Spectroscopies. *Journal of the American Ceramic Society*, 57(10):2549–2557, 1998. `doi:10.1111/j.1151-2916.1998.tb02660.x`.

[172] D. Bouchet and C. Colliex. Experimental study of ELNES at grain boundaries in alumina: Intergranular radiation damage effects on Al-L_{23} and O-K edges. *Ultramicroscopy*, 96(2):139–152, 2003. `doi:10.1016/S0304-3991(02)00437-0`.

[173] S. Nyquist and U. Hålenius. An EELS study of near edge structures of the oxygen K-edge in spinels. *Physics and Chemistry of Minerals*, 41(4):255–265, 2014. `doi:10.1007/s00269-013-0643-z`.

[174] K. Kaneko, T. Gemming, I. Tanaka, and H. Müllejans. Analytical investigation of random grain boundaries of Zr-doped sintered α-Al_2O_3 by transmission electron microscopy and scanning transmission electron microscopy. *Philosophical Magazine*, 77(5):1255–1272, 1998. `doi:10.1080/01418619808214251`.

[175] A. Y. Borisevich, S. Wang, S. N. Rashkeev, M. Glazoff, S. J. Pennycook, and S. T. Pantelides. Dual nanoparticle/substrate control of catalytic dehydrogenation. *Advanced Materials*, 19(16):2129–2133, 2007. `doi:10.1002/adma.200601618`.

Acknowledgments

For all the support I received during my time at the University of Tübingen to work towards my PhD, I would like to thank the following people:

- First of all, I want to thank my supervisor **Prof. Dr. Oliver Eibl** for giving me the opportunity to work on interesting topics in the material science in his group, as well as for all the helpful discussions during the last years.

- **Prof. Dr. Frank Schreiber** for accepting to be the second supervisor and **Prof. Dr. Jannik Meyer** for accepting to be the second reviewer of my thesis.

- **Prof. Dr. Monika Fleischer** and **Prof. Dr. Roland Roth** for joining the defense committee.

- **Eva Lohmann** for her support and help with all kinds of problems and the introduction to the XL30.

- **Ralf Zenke** for his help, especially whenever maintenance work was due.

- **Praveen Kumar** for countless talks and discussions and even more coffees in our office.

- **Nicola Peranio** for his help at the beginning of my stay and the introduction into TEM sample preparation and microscopy work.

- **Benjamin Willsch** for his introduction to temperature dependent electrical measurements in the cryostat lab.

- All other colleagues, Bachelor-, Master- and Diploma students and Hiwis that made my stay here more pleasant.

List of Publications

Peer-reviewed journal papers

1. **M. Pfeffer**, P. Kumar and O. Eibl. High-Efficiency Crystalline-Si Solar Cells with Screen-Printed Front-Side Metallization: A Percolation Model to Explain the Current Path. *Journal of Electronic Materials*, 45(11):5764-5772, 2016. doi: 10.1007/s11664-016-4818-5
2. P. Kumar, **M. Pfeffer**, B. Willsch and O. Eibl. Contact formation of front side metallization in p-type, single crystalline Si solar cells: Microstructure, temperature dependent series resistance and percolation model. *Sol. Energy Mater. Sol. Cells*, 145:358-367, 2016. doi: 10.1016/j.solmat.2015.10.042
3. P. Kumar, **M. Pfeffer**, B. Willsch, O. Eibl, L. J. Koduvelikulathu, V. D. Mihailetchi and R. Kopecek. N-type single-crystalline Si solar cells: Front side metallization for solar cells reaching 20% efficiency. *Sol. Energy Mater. Sol. Cells*, 157:200-208, 2016. doi: 10.1016/j.solmat.2016.05.027
4. P. Kumar, **M. Pfeffer**, N. Peranio, O. Eibl, S. BäSSler, H. Reith and K. Nielsch. Ternary, single-crystalline $\mathrm{Bi_2(Te,Se)_3}$ nanowires grown by electrodeposition. *Acta Materialia*, 125:238-245, 2017. doi: 10.1016/j.actamat.2016.11.057.
5. P. Kumar, **M. Pfeffer**, B. Willsch, O. Eibl, L. Yedra, S. Eswara, J.-N. Audinot and T. Wirtz. Direct imaging of dopant distributions across the Si-metallization interfaces in solar cells: Correlative nano-analytics by electron microscopy and NanoSIMS. *Sol. Energy Mater. Sol. Cells*, 160:398-409, 2017. doi: 10.1016/j.solmat.2016.11.004
6. P. Kumar, **M. Pfeffer**, E. Schweda, O. Eibl, J. Qui and Z. Shi. PbSe mid-IR photoconductive thin films (part I): Phase analysis of the functional layer. *Journal of Alloys and Compounds*, 724:316-326, 2017. doi: 10.1016/j.jallcom.2017.06.330
7. P. Kumar, Z. Aabdin, **M. Pfeffer** and O. Eibl. High-efficiency, single-crystalline, p- and n-type Si solar cells: Microstructure and chemical analysis of the glass layer. *Solar Energy Materials and Solar Cells*, 178:52-64, 2018. doi: 10.1016/j.solmat.2018.01.001
8. P. Kumar, **M. Pfeffer**, C. Berthold and O. Eibl. *PbSe mid-IR photoconductive thin films (part-II): Structural analysis of the functional layer*, 735:1654-1661. doi: 10.1016/j.jallcom.2017.11.252

Peer-reviewed conference papers

1. **M. Pfeffer**, P. Kumar, M. Zehender, B. Willsch and O. Eibl. Front Side Metallization of p and n-Type Si Solar Cells: A Percolation Model for Explaining the Current Path. *EUPVSEC Proceedings*, 247-250, September 2017. doi: 10.4229/EUPVSEC20172017-2AO.4.4
2. P. Kumar, **M. Pfeffer** and O. Eibl. Screen Printed Mono-Crystalline Si Solar Cells: Assessing the Microstructure and Dopant Concentration at the Front Side Metallization Interface by Electron Microscopy and NanoSIMS. *EUPVSEC Proceedings*, 907-910, September 2017. doi: 10.4229/EUPVSEC20172017-2CV.2.55
3. P. Kumar, **M. Pfeffer** and O. Eibl. Front Side Metallization of p- and n-Type Si Solar Cells: Microstructure of the Glass Layer. *EUPVSEC Proceedings*, 923-927, September 2017. doi: 10.4229/EUPVSEC20172017-2CV.2.64

Curriculum Vitae

School

Sep 1992 - Jul 1996	Johann-Gemmer-Grundschule in Ahorn, Germany
Sep 1996 - Jul 2005	Gymnasium Casimirianum in Coburg, Germany

University

Oct 2006 - May 2013	Julius-Maximilians-Universität in Würzburg, Germany Diplom Physiker Univ.
Sep 2009 - May 2010	Heriot-Watt Univeristy in Edinburgh, Scotland Master of Physics in Physical Science with Honours of the First Class
Oct 2010 - Nov 2018	FernUniversität in Hagen, Germany B. Sc. Wirtschaftswissenschaft

PhD Thesis

Dec 2014 - Nov 2018	Eberhard Karls Universität in Tübingen, Germany Thesis Supervisor: Prof. Dr. Oliver Eibl

Eidesstattliche Versicherung

Ich erkläre hiermit, dass ich die zur Promotion eingereichte Arbeit mit dem Titel "Pseudo-γ Al_2O_3: A new transparent conductive oxide with outstanding structural properties" selbständig verfasst, nur die angegebenen Quellen und Hilfsmittel benutzt und wörtlich oder inhaltlich übernommene Stellen als solche gekennzeichnet habe. Ich versichere an Eides statt, dass diese Angaben wahr sind und dass ich nichts verschwiegen habe. Mir ist bekannt, dass die falsche Abgabe einer Versicherung an Eides statt mit Freiheitsstrafen bis zu drei Jahren oder mit Geldstrafe bestraft wird.
Weiterhin erkläre ich, dass bisher kein Promotionsversuch unternommen wurde.

Tübingen, den 07.01.2019